UNIVERSITÀ DEGLI STUDI DI CATANIA
facoltà di scienze matematiche, fisiche e naturali
Ph.D. in Physics

Salvatore Viola

Design and operation of novel underwater acoustic detectors: applications to particle physics and multidisciplinary science for the NEMO-SMO and KM3NeT projects

Ph.D. thesis

Supervisors:
Prof. Marcello Lattuada
Dott. Giorgio Riccobene

PhD Coordinator:
Prof. Francesco Riggi

XXV cycle (2009-2012)

Ai miei genitori.

Contents

Introduction

Neutrino-astronomy is one of the most interesting frontiers of the astro-particle physics. Observations of cosmic rays with energy up to $3 \cdot 10^{20}$ eV have demonstrated the existence of astrophysical objects able to accelerate hadrons up to extreme energies. Theoretical studies foresee emission of high energy charged particles from several astrophysical sources, whose study is nowadays accessible only through their electromagnetic emission. In these sources, acceleration of protons, little affected by synchrotron energy losses, can be efficient up to $10^{19\div20}$ eV. Protons acceleration, followed by electromagnetic or nuclear interactions, can lead to fluxes of very high energy neutrinos and photons. Photons up to ~ 10 TeV have been recently observed from Galactic Supernova Remnants and closest Active Galactic Nuclei. Nevertheless, the gamma astronomy potential at these energies is limited. In fact, gamma rays with energy above 10 TeV can be observed within a distance of a few millions of light-year from the Earth, because of the gamma interaction with the cosmic microwave background radiation (CMBR) and with interstellar medium. The use of hadrons as probes to explore remote Universe is also limited: neutrons have a mean life too short ($\tau_0 \approx 900$ s), heavy nuclei suffer fragmentation processes in their interaction with interstellar medium and protons are deflected by the Galactic magnetic field (~ 3 μG), avoiding the identification of their sources. Eventually, very high energy protons (10^{21} eV) are absorbed by the interaction with CMBR within about 10^7 light-year. Neutrinos are an optimal probe to observe high energy astrophysical phenomena. Neutrinos interact only via weak interaction, so they allow the exploration of the Universe and regions close to black-holes, where the radiation and matter densities hinder the photon emission. The detection of high energy neutrinos, not yet claimed by present experiments, will provide powerful informations to update astrophysical models describing Supernova Remnants, Active Galactic Nuclei and Gamma-Ray Burst or to find unattended neutrino sources.

The faintness of expected neutrino flux at Earth and the extrapolated HE neutrinos cross sections indicate that a detection volume of a few km^3 is required to detect a statically significant number of events per year. For neutrino energies between 10^{11} eV and 10^{16} eV the underwater Čerenkov technique is validated and used. ICECUBE, installed in the polar ices of Antarctica, is today the first operating km^3-scale neutrino telescope. In parallel, the European KM3NeT Consortium aims at the construction of a 5 km^3 neutrino telescope to be installed in Mediterranean Sea. Thanks to transparency of seawater, to larger volume and thanks to geographical location, in the Northern Hemisphere, KM3NeT is expected to have better performances with respect to ICECUBE. Within the KM3NeT Consortium, the NEMO Collaboration has built a detection unit prototype, NEMO Phase-II, described in details in Chapter 4 of this thesis. NEMO Phase-II will be installed in the first months of 2013 at a depth of 3500 m offshore Capo Passero (Sicily). NEMO Phase-II hosts SMO (Submarine Multidisciplinary Observatory) acoustic array, that is the main topic of this work. SMO will provide acoustic positioning (APS) of the NEMO tower mechanical structure, detecting acoustic signals produced by a long baseline (LBL) of five geo-referenced acoustic beacons anchored on the sea-floor. The APS is a mandatory subsystem of NEMO Phase-II since it will provide position of OMs, an information used to the Čerenkov tracks reconstruction. Unlike traditional underwater acoustic positioning system, the SMO data acquisition system is based on "all data to shore" concept: all acoustic data are continuously sampled underwater and transmitted to shore through an electro-optical cable for real-time analysis. This new feature was implemented to perform preliminary studies on acoustic detection of high-energy astrophysical neutrinos. In this work tests and results on the performances of the SMO acoustic array are presented.

Chapter 1

High-energy astronomy

High-energy astronomy investigates fundamental questions for the understanding of the cosmic environment, among these the origin of cosmic rays, i.e. the mechanisms and places where high- and ultra-high-energy particles are produced and/or accelerated. Moreover, high-energy astronomy investigates particle physics questions like the nature of the Dark Matter, neutrino interaction and ultra-high-energy cross sections of cosmic rays or neutrinos with nuclei. The answers to these questions can be obtained by combining data collected in different energy regimes using different cosmic messengers: the so-called multi-messenger approach. High-energy messengers include gamma rays, neutrinos, and charged cosmic rays. In this chapter on overview on cosmic rays will be given, in particular we will focus on the cosmic neutrino case.

1.1 Cosmic rays

The cosmic rays have been studied for nearly a century. In the thirties and the forties of the 20th century, the cosmic rays study set also the bases of progress in elementary particle physics. In the first decades since their discovery, cosmic rays have represented, indeed, a unique tool to observe unknown particles. Thanks to the study of the cosmic rays positron, pion, muon have been detected for the first time and the first decays of strange particles have been observed [1]. Nowadays, the study of cosmic rays, carrying energies much larger than the energies that can be reach in the terrestrial accelerators, is opening a window to the Universe at high energies.

1.1.1 Cosmic rays composition

The cosmic rays flux, measured at the top of the Earth's atmosphere is composed of 98% of nuclei. The remaining 2% is composed of electrons and positrons. The nuclear component consists of 87% of protons, 12%

of helium and only 1% of heavier nuclei. In Fig. 1.1 the cosmic ray nuclear elements abundances normalized to the Carbon's one (black line), and the Solar System abundances (green line) are shown. Both relative abundances feature peaks for Carbon, Nitrogen, Oxygen and Iron. This feature suggests that the observed cosmic rays originate from galactic supernova explosion. In the cosmic rays flux, over-abundances of nuclei with atomic numbers smaller than those of C,N,O (Li, Be, B) and Fe (SC, Mn, Cr,Ti, V) with respect to the abundances observed in Solar System suggest spallation processes and in particular the interaction between primary nuclei and the interstellar medium with consequent production of lighter elements.

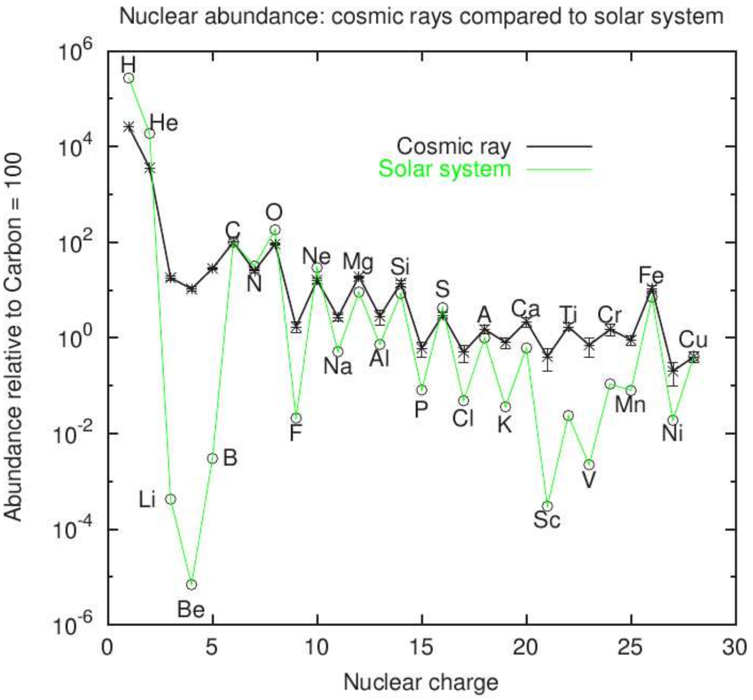

Figure 1.1: Relative abundances with respect to the Carbon abundance in the cosmic rays (black line) and in the Solar system (green line) [2].

1.1.2 Cosmic rays spectrum

The cosmic rays spectrum extends over a large energy range: it covers more than 10 orders of magnitude of energy, up to some 10^{20} eV, while the flux extends over more than 28 orders of magnitude (see Fig. 1.2). At energy ≤ 1 GeV, the modulation of the observed cosmic rays flux is in anticorrelation with the the solar cycle [3]. At higher energies, the inclusive spectrum can be described by a power law

$$\frac{dN}{dE} \propto E^{-\gamma} \tag{1.1}$$

with a spectral index γ between 2.7 and 3, as shown in Fig. 1.2.

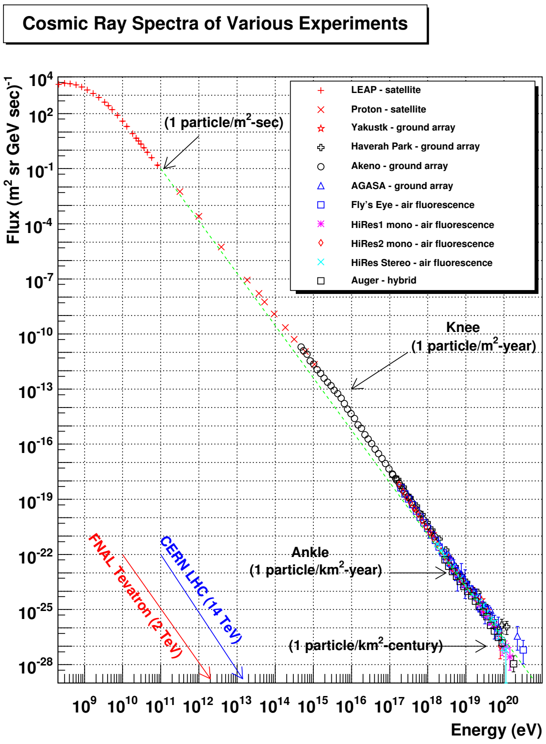

Figure 1.2: The inclusive energy spectra of cosmic rays as measured at the Earth.

Up to $\sim 10^{15}$ eV, the flux is mainly composed of protons and the spectrum is well-described by Eq. 1.1 with spectral index $\gamma = 2.7$. At

$\sim 10^{15}$ eV, the slope of the differential flux becomes steeper ($\gamma = 3.0$). In this region of the spectrum, called the "knee", experimental data show a change in the mass composition, that becomes heavier, due to reduction of the protonic component. This feature was explained by Ginzburg and Syrovatskii in 1965 [4]. They noticed that at energies of about 10^{15} eV, the radius of curvature of the protons in the Galactic magnetic field is about $\sim$ 0.1 pc, that is the typical scale of the regions of irregularity of the galactic magnetic field. So, the confinement of the protons in the Galaxy becomes very unlikely and this results in a leakage of protons from the Galactic disk that is consistent with the decrease of these observed in the flux. At energies higher than 10^{18} eV, the spectral index changes again. In this region, called the "ankle", the spectral index becomes again ~ 2.7. At the "ankle" energies the radius of curvature of the protons is ~ 1 kpc, one order of magnitude bigger than the thickness of the galactic disk. This consideration suggests an extragalactic origin for the cosmic rays with energies higher than 10^{18} eV. This hypothesis is supported by the measurements performed by the AUGER Collaboration, that don't exhibit correlation between the arrival direction of charged particles with energy of 10^{19} eV and the direction of the galactic disk [5].

1.1.3 Particle acceleration models

One of the fundamental issues for the understanding of our cosmic environment deals with the mechanisms of acceleration of the cosmic rays up to ultra-relativistic energies. A first model of particle acceleration was proposed by Fermi in 1949 [6]. In his model Fermi described an acceleration mechanism, where charged particles acquire energy by stochastic magnetic collisions with clouds of interstellar gas. In the Fermi model, the particles acquire in each collision a fractional energy gain $\xi = \Delta E/E$, after n collisions the total energy of a particle with an initial energy E_0 is

$$E_n = E_0(1+\xi)^n. \tag{1.2}$$

If P_{esc} is the escape probability of the particle from the acceleration region after a collision, the probability to remain confined in the acceleration region after n collisions is $(1-P_{esc})^n$. The number of collisions required to reach the energy E is

$$n = \ln\left(\frac{E}{E_0}\right) / \ln(1+\xi)\ . \tag{1.3}$$

With this mechanism the proportion of particles accelerated at energies higher than E is

$$N(\geq E) \propto \frac{1}{P_{esc}}\left(\frac{E}{E_0}\right)^{-\gamma}\ . \tag{1.4}$$

The integral spectral index of the power law obtained by Fermi is

$$\gamma = \log\left(\frac{1}{1-P_{esc}}\right) / \log(1+\xi) \sim \frac{P_{esc}}{\xi} = \frac{1}{\xi}\frac{T_{cycle}}{T_{esc}}, \tag{1.5}$$

where T_{cycle} is the typical time of an acceleration cycle and T_{esc} the escape time from the acceleration region.

Although the expression obtained by Fermi can describe the power law of the observed cosmic rays spectrum, it is inefficient to reproduce the observed spectral index by taking under consideration the typical velocity of the galactic clouds ($V/c \leq 10^{-4}$) and the mean free path of the particles in the galactic interstellar medium, that is ~ 1 pc. In 1978, Bell re-elaborated the Fermi's model, considering the interaction of particles with strong shock waves propagating in the interstellar medium [7]. A shock is generated when the velocity of a gas or a plasma expanding in the interstellar medium is greater than the sound velocity in the gas. The acceleration model proposed by Bell is sketched in Fig. 1.3.

For shock front velocity much larger than the speed of sound in the plasma the velocity of the matter behind the shock, u, is related to the velocity of the shock front V_s, by means of the relation

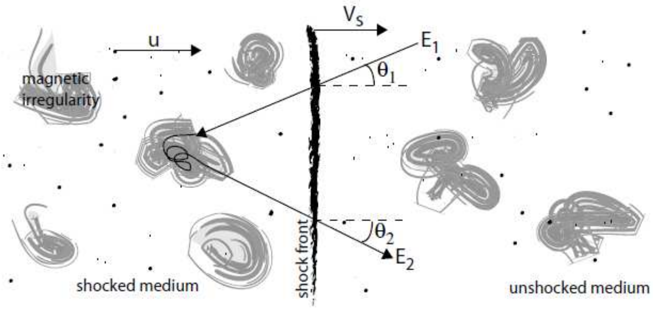

Figure 1.3: Schematic view of the acceleration mechanism of a particle in a plane shock wave propagating in the interstellar medium at velocity V_s.

$$u = \frac{3}{4} V_s. \tag{1.6}$$

The particles move from the unshocked medium into the shocked medium, where they elastically scatter on the irregular magnetic fields. The gain of energy of the particles passing through the shock in both directions can obtained by considering the Lorentz transformation between the shocked and the unshocked frames:

$$E' = \gamma_V (E + p_x V), \tag{1.7}$$

with the direction x orthogonal to the propagation direction of the shock wave. For relativistic shocks ($\gamma_V = 1$) and particles velocity very close to light's one ($E = pc$, $p_x = (E/c)\cos\theta$), the particles gain a fraction of its original energy:

$$\Delta E = pV\cos\theta \;\; ; \;\; \frac{\Delta E}{E} = \frac{V}{c}\cos\theta. \tag{1.8}$$

After the collision, the probability for a particle to escape from the acceleration region is

$$P_{esc} = \frac{V_s}{c}, \tag{1.9}$$

the integral spectral index in Eq. 1.5 becomes

$$\gamma = \frac{P_{esc}}{\xi} \simeq 1 + \frac{4}{M^2} \tag{1.10}$$

where $M = V_s/c$ is the Mach number of the shock wave. For very strong shocks ($M >> 1$) the integral spectral index is $\gamma \approx 1$, corresponding to a differential spectral index of ≈ 2. This value, in agreement with the experimental measurements does not depend on the sources of the shock. According to the Fermi-Bell acceleration model, the maximum energy that a particle can reach is a function of its confinement time within the shock. This, in its turn, is a function of the object dimensions and strength of the magnetic field. Hillas provided a rule for the maximum energy E_{max} that a charged particle can reach in a shock:

$$E_{max} = \beta c \cdot Ze \cdot B_{\mu G} \cdot L_{kpc} \cdot 10^{18}\mathrm{eV} \tag{1.11}$$

where βc is the shock wave velocity, Z is the particle charge in units of e, B is the magnetic field and L is the linear extension of the acceleration source. The maximum energies that a charged particle can reach in the main candidate acceleration sources are reported in Fig. 1.4, in the so called “Hillas plot” [8].

1.2 Gamma rays astronomy

Since protons and nuclei are electrically charged, their paths bend as they travel trough cosmic magnetic fields. They don’t point back to their sources, except at the very highest energies, where deflection becomes small. Fortunately, the suspected charged particles cosmic sources are also predicted to emit neutral elementary particles: gamma rays and, in case of hadronic acceleration mechanisms, neutrinos. Imaging Air Čerenkov Telescopes such as MAGIC [9], HESS [10] and VERITAS [11] have observed gamma rays with energies up to 10^{14} eV from a large vari-

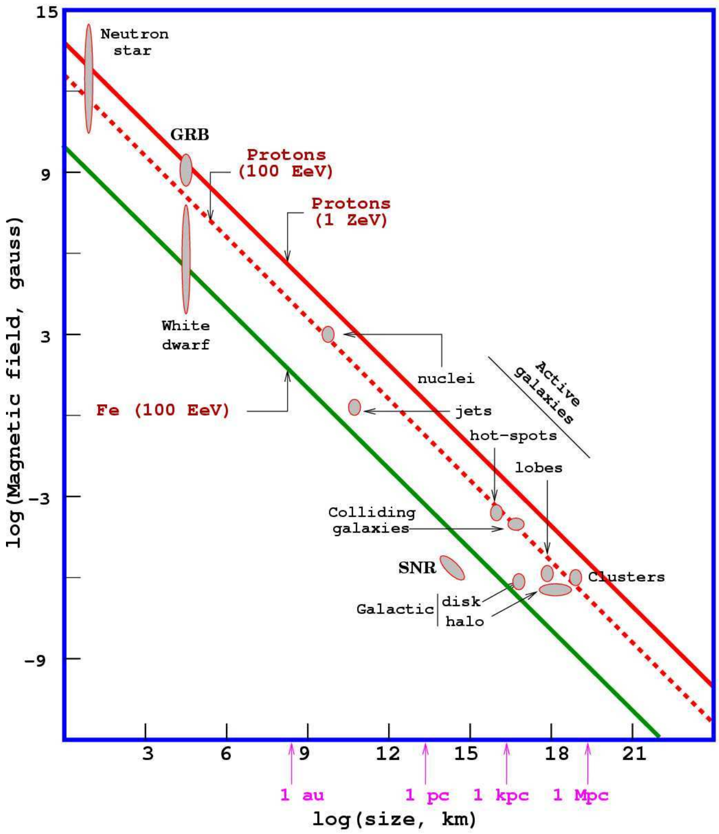

Figure 1.4: The Hillas plot. Astrophysical sources accelerate high-energy protons and nuclei through diffuse shock acceleration. The particle maximum energy is a function of the source dimensions and magnetic field. Astrophysical sources under the green line can't accelerate iron nuclei above 100 EeV, astrophysical sources under the dotted red line can't accelerate protons above 100 EeV, astrophysical sources under the continuous red line can't accelerate protons above 1 ZeV.

ety of sources. It is still not clear if the observed gamma rays are radiated by sources accelerating electrons and positrons (leptonic source scenario) or they are produced in the interactions of high-energy protons with the ambient matter (hadronic source scenario). The two astrophysical gamma rays production scenarios are described in the following sections.

1.2.1 Leptonic scenario

In the leptonic scenario high energy gamma-ray emission from astrophysical sources is interpreted through pure electromagnetic processes, namely the inverse Compton scattering of electrons and positrons accelerated via Fermi-Bell mechanism off low-energy radiation fields, such as the field produced by synchrotron emission of charged particles, the cosmic microwave background (CMB) or the interstellar infra-red and optical radiation. In this scenario we expect to observe, in the energy spectrum of the photons produced by the source, two bumps as shown in Fig. 1.5.

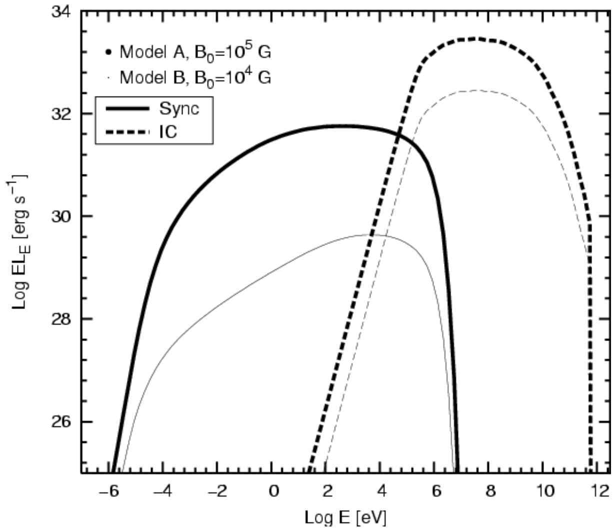

Figure 1.5: The energy spectrum of high energy photons foreseen in the leptonic scenario by considering two different magnetic fields B. The energy spectrum of these photons is characterized by two bumps: the low energy bump is due to the synchrotron radiation of the electrons accelerating in the magnetic fields, the high energy bump is due to the scattering of low energy photons by electrons moving with ultra relativistic velocity.

The lower energy bump is associated to the emission of synchrotron radiation of electrons accelerated in the magnetic field of the source. For a particle of energy E and velocity v, the energy loss rate by synchrotron radiation is:

$$-\frac{dE}{dt} = \frac{4}{3}\sigma_T c \gamma^2 \left(\frac{v}{c}\right)^2 U_{mag} \tag{1.12}$$

where σ_T, c, γ are respectively the Thomson cross-section, the speed of light and the Lorentz factor. $U_{mag} = B^2/2\mu_0$, where μ_0 is the magnetic constant, represents the energy density of the magnetic field B. Consequently, the process is more efficient for intensive magnetic fields. The high energy bump is attributed to the inverse-Compton scattering (ICS) of photons off relativistic electrons accelerated by the Fermi mechanism. Conservation of momentum in the electron's rest frame results in the transfer of energy from the electron to the photon. In the ultra-relativistic limit ($\gamma \gg 1$), if ν_0 is the frequency of a mono-energetic radiation in the electron's frame, the average frequency of the up-scattered radiations in the observer frame is:

$$\langle \nu \rangle = \frac{4}{3}\gamma^2 \nu_0. \tag{1.13}$$

The resulting ICS spectrum is sharply peaked just below the maximum frequency ν_{max}, that is:

$$\nu_{max} \approx 4\gamma^2 \nu_0. \tag{1.14}$$

If the electron-energy distribution in the source follows a power law $N(E) \propto E^{-\delta}$, the scattered photons spectrum will also follow a power law with spectral index $\alpha = (1-\delta)/2$.

1.2.2 Hadronic scenario

In the hadronic scenario, protons in the astrophysical sources, are accelerated (together with electrons) via Fermi mechanism. The accelerated protons interact with ambient radiation and/or matter, within the source or with nearby gas clouds producing pions. Neutral pions then decay into a pair of γs, while charged pions decay producing neutrinos:

$$\pi^0 \longrightarrow \gamma + \gamma \tag{1.15}$$

$$\pi^+ \longrightarrow \mu^+ + \nu_\mu \longrightarrow e^+ + \nu_e + \nu_\mu + \bar{\nu_\mu} \tag{1.15}$$

$$\pi^- \longrightarrow \mu^- + \bar{\nu}_\mu \longrightarrow e^- + \bar{\nu_e} + \nu_\mu + \bar{\nu_\mu}$$

(1.15)

The interactions of the protons with matter occur via *pp* and *pn* interactions. The dominant interaction of protons with the ambient radiation occurs via the Δ^+ resonance:

$$\begin{aligned} p + \gamma &\longrightarrow \Delta^+ \longrightarrow N + \pi^0 \\ p + \gamma &\longrightarrow \Delta^+ \longrightarrow N + \pi^\pm \end{aligned} \tag{1.16}$$

where the pion carries about 20% of the proton energy.

The energy threshold of the $p\gamma$ reaction by means of the Δ^+ resonant channel is $E_p \approx 300$ MeV in the center of mass reference frame. In the hadronic scenario a peak at $E_\gamma \approx 1$ GeV and a clear decrease at photon energies lower than 400 MeV, in the emissivity spectrum, are thus foreseen [12]. Recently, the AGILE gamma-ray observations in the energy range 50 MeV $\div$ 10 GeV of the supernova remnant (SNR)W44 demonstrated that multi-wavelength observation constraints derived from radio, optical, X-ray, and gamma-ray detectors data are consistent with hadron-dominated model, establishing for the first time an evidence for pion-generated gamma emission in a SNR [13]. In this scenario, considering a primary Fermi proton flux with a E^{-2} power law, a muon neutrino flux with a spectrum ${E_{\nu_\mu}}^{-2}$ is also expected. Taking into account the neutrino flavour oscillation, we expected at Earth, equipartition between the three leptonic flavours.

1.2.3 Limits of the gamma ray astronomy

Although gamma-rays are electrically neutral and their trajectory is not bent by magnetic fields, they interact with the interstellar medium and, at energies $\geq$ TeV, also interact with the cosmic radiation through the pair-production reaction, which has an energy threshold E given by:

$$4E\varepsilon \sim (2m_e)^2, \tag{1.17}$$

where E and ε are the high energy gamma and the background photon energies respectively. According to (1.17), TeV photons interact with the infra-red radiation, PeV photons interact with the CMBR (Cosmic Microwave Background Radiation) and EeV photon interact the radio waves. The mean free path of the photons as a function of the energy is shown in Fig. 1.6.

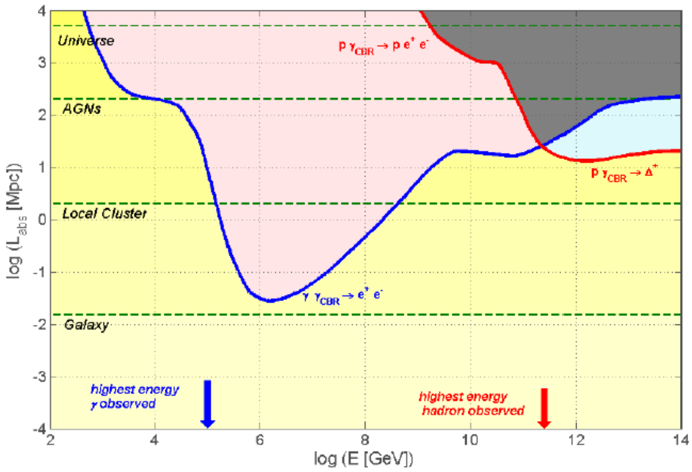

Figure 1.6: Mean free path of the photons in the interstellar medium as a function of the energy (blue line). For comparison, the plot includes the mean free path of the proton in CMBR (red line)

Therefore, trace back extragalactic sources by means of gamma-rays with energy $E \geq 100$ TeV is strongly hindered by their interaction with the interstellar photons background.

1.3 Neutrino astronomy

The neutrino is an optimal probe to study the high energy Universe. Thanks to its very low cross section ($\sigma_{\nu_\mu} \sim 10^{-36}$cm^2 for E_ν=1 TeV), the neutrino is the only particle of the Standard Model that can be propagate unabsorbed in the intergalactic space, travelling in a straight-line. Therefore, neutrino-astronomy represents an optimal tool to explore the candidate sources of cosmic rays and to understand their energy dissipation mechanisms. Neutrino detection can provide, indeed, an incontrovertible evidence of the presence of hadronic processes in high-energy gamma-ray sources.

1.3.1 High energy neutrino sources

According to the Fermi-Bell acceleration mechanisms, neutrinos are produced in the decays of the mesons coming from the collisions of accelerated primary hadrons with the gas clouds that enclose the source or with the photons of the background radiation. In analogy with the beam-target collisions in the terrestrial accelerators, this process is called “Astrophysical Beam Dump”. If the neutrino source flux is intense enough to allow detection of large number of events at Earth compared to the expected background, the position in the sky of the neutrino source can be identified and correlated to sources detected in gamma wavelengths. A “diffuse” neutrino flux is also expected to be observed as sum of faint fluxes from all neutrino cosmic sources. Theoretical models foresee both Galactic and Extragalactic neutrino sources. A brief description of the main candidate neutrino sources is given in the next sections.

Galactic sources

Supernova Remnants

At the end of their evolution, stars with mass greater than $8M_\odot$ burn all internal nuclear fuel up to produce an iron core. The subsequent gravitational collapse results in a big explosion, called Supernova: almost all stellar mass is expelled in the surrounding space. The object resulting from this explosion is called Supernova Remnant (SNR). The shock wave, produced in the explosion, propagates through the ejected gas cloud and can accelerate charged particles by means of the Fermi-Bell mechanism. Considering that the typical energy released by a SN explosions is 10^{51} erg/s and the frequency of the Supernova events in the Milky Way is $dN_{SN}/dt \sim 3/(100\text{yr})$, the estimated total luminosity of the SNRs in the Galaxy is ${L_{SN}}^{tot} \approx 3 \cdot 10^{42}$ erg/s. Since the estimated cosmic ray luminosity in the Galaxy is $L_{CR} \approx 10^{41}$ erg/s, SNRs can justify the observed proton flux up to $\sim 10^{15}$ eV with an production efficiency of a few percent. In a hadronic scenario, the acceleration process in SNRs produces a neutrino flux up to energies of $\sim 10^{13}$ eV.

X-ray binaries

X-ray binaries are a class of binary stars composed of a massive object (a neutron star or a stellar black hole) and a companion star (see Fig. 1.7). Mass transfer from the companion star towards the compact object generates an accretion disk emitting thermic radiation in the X range. The two relativistic jets along the rotation axis of the accretion disk are supposed to be acceleration sites for charged particles up to energies of 10^{16} eV with high energy neutrino production. The expected neutrino flux from the best candidate X-ray binaries SS433 and GX339-4 is $\sim 10^{-11}$ erg cm^{-2}s^{-1} [14].

The Fermi bubbles

A recent analysis of Fermi-LAT satellite data [15] has revealed an intense gamma-ray emission from two large regions extending 50 degrees above and below the Galactic Center with a width of about 40 degrees in longitude as shown in Fig. 1.8.

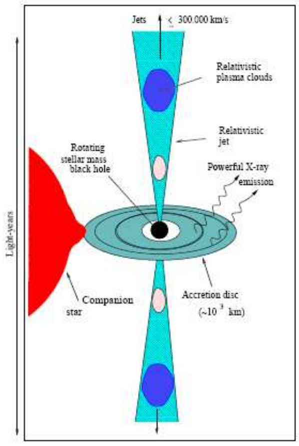

Figure 1.7: Schematic view of a X-ray binary. X-ray binaries are powered by compact objects (neutron stars or stellar mass black holes) via mass accretion from a companion star. This produces collimated jets that boost the energy of stellar photons to the range of very energetic gamma-rays.

The emission of the gamma rays is homogeneous within the bubbles. The energy spectrum in the range 1 GeV $\div$ 100 GeV is compatible with a power-law spectrum described by

$$E^2 \frac{d\Phi_\gamma}{dE} \approx 3 \div 6 \cdot 10^{-7} \text{GeV cm}^{-2} s^{-1} sr^{-1} (1.18)$$

The edges of the bubbles seem to be correlated with ROSAT X-ray maps at 1.5 $\div$ 2 keV, while the inner parts are correlated with the hard-spectrum microwave excess, known as WMAP haze [17] [18]. The observed features suggest an hybrid emission scenario with an underlying hadronic process producing high-energy gamma rays through π_0 decay. Under the hypothesis that the source is transparent to gamma rays and that the mechanism responsible for the gamma-ray emission is hadronic, the estimated muon neutrino plus anti-neutrino flux is $\Phi_\nu \approx 10^{-7}$ GeV cm^{-2} s^{-1} [19].

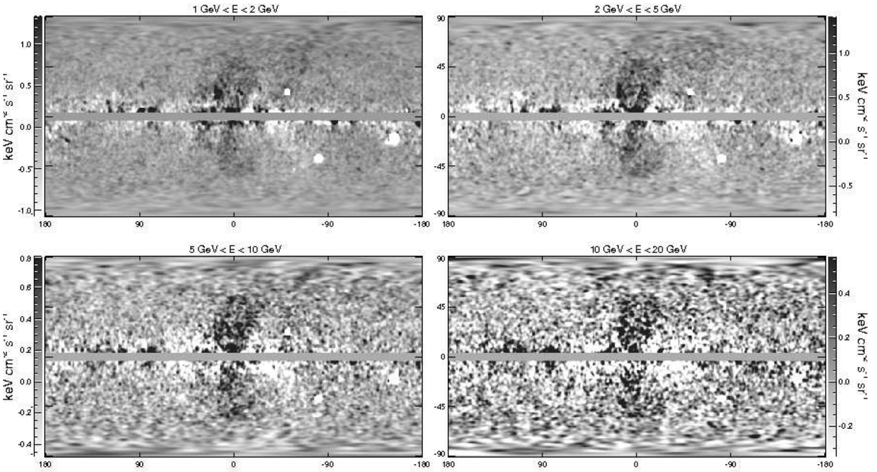

Figure 1.8: All-sky residual map after subtracting the Fermi diffuse galactic model from the LAT 1.6 years maps in 4 energy bins. Two gamma-ray bubbles emerge from the Galactic Center and extend 50 degrees North and South the plane of the Milky Way [15] [16] .

Extragalactic sources

Gamma Ray Bursts

The gamma ray bursts (GRBs) are violent electromagnetic emissions at high energies (X and gamma-ray), followed by an intense emission in the whole electromagnetic bandwidth, called *afterglow*. Since the end of the 1990s the study of the *afterglow* in the optical band has allowed to locate GRBs events at cosmological distance from Earth. These events feature a red-shift z between 0.0085 and 3.4; the total energy emitted by GRBs ranges from 10^{51} to 10^{54} erg. GRBs are classified by the time-scale of their high-energy emission: GRBs are defined as *short* when the observed time of emission is shorter than 1 second; when the emission persists for more than 1 second, GRBs are called *long*. Theoretical study attribute the *short* GRBs to the coalescence of two rotating compact objects. Instead, *long* GRBs are associated to the gravitational collapse of the evolved core of a massive star, like type Ib/c Supernovae. The spectrum of high energy photons emitted by GRBs can be parametrized as a broken power-law $dN/dE = E^{-\alpha}$, where $\alpha \approx 1$ at energy up to E_b = 100 keV ÷ 800 keV and $\alpha \approx 2$ at energy above E_b [20].The emission of gamma radiation can be explained by the *fireball model*, illustrated in Fig. 1.9.

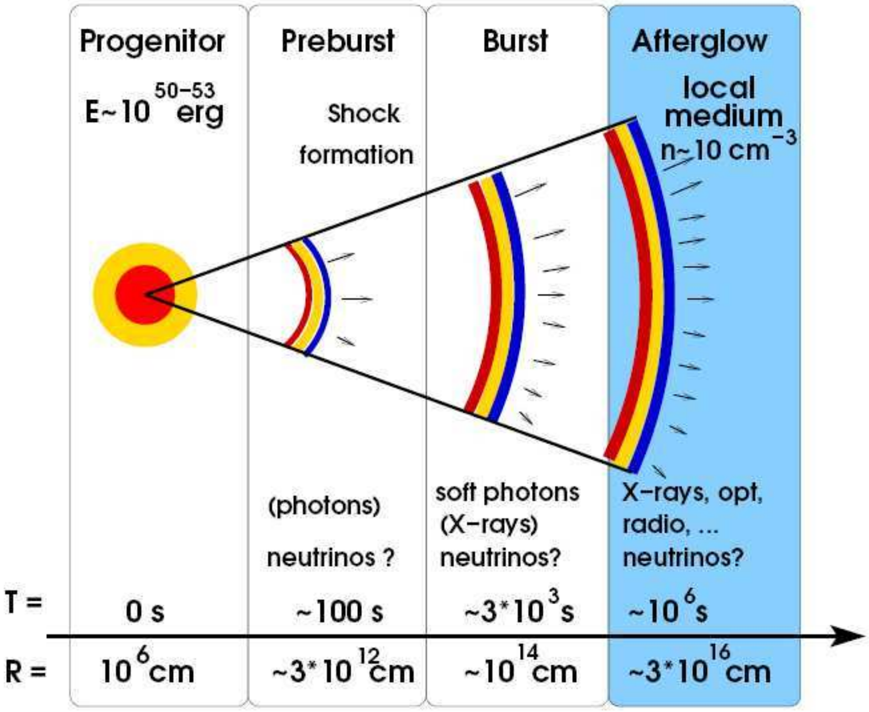

Figure 1.9: Schematic view of the *fireball model* to explain the gamma rays and neutrinos emission from the Gamma Ray Bursts

In this model a large quantity of matter is released by a central engine in a short time producing an opaque photon-lepton “fireball” through the production of electron-positron pairs. The external layers of the fireball move with a velocity lower than the velocity of the internal ones. When the internal layers reach the external layers, shock waves, called *internal shocks* are produced. These shock waves represent and ideal acceleration site for charged particles. Unlike the protons that can be accelerated up to $\sim 10^{21}$ eV , high energy electrons lose their energy via synchrotron emission and inverse compton; gamma emission produce the observed GRB [21]. Subsequently, the interaction of the fireball with the interstellar medium generates the so-called *external shocks*, where the observed *afterglow* radiation emission is produced. The interaction of charged particles, accelerated in the shock waves, with environmental radiation produces mesons, that decay in high energy γs and neutrinos. The expected diffuse neutrino flux from GRBs is $\approx 10^{-8}$ GeV cm^{-2}s^{-1}sr^{-1} [22]. According to the model proposed by Waxman and Bahcall, the delay between the time of arrival of the gamma-ray and the time of arrival of the neutrinos at Earth is less than 10 seconds [23]. However, a dedicated search for neutrinos from p-γ interactions in the prompt phase of the gamma-ray burst fireball using the 40 String IceCube Detector, produced no evidence for neutrino emission, excluding prevailing models at 90% confidence [24].

Active Galactic Nuclei

The term Active Galactic Nuclei (AGN) indicates a class of astrophysical compact sources at the centre of its host galaxy emitting an enormous amount of energy, up to 10^{46} erg/s. According to the standard paradigm, AGNs are composed of a super-massive black-hole with mass $M_{BH} = 10^6 \div 10^9\ M_\odot$ surrounded by an accretion disk and an obscuring torus of dust. The fall of the matter towards the black hole produces a violent energy release that results in an ejection of two relativistic jets from the vicinity of the black hole. A schematic view of an AGN is shown in Fig. 1.10.

The exceptional luminosity of these sources can be attributed to particle acceleration and interaction through either leptonic or hadronic processes. In the leptonic scenario, the emission can be associated to the Synchrotron self-Compton interactions, i.e. the inverse Compton scattering of the electrons with synchrotron emission radiated by the same

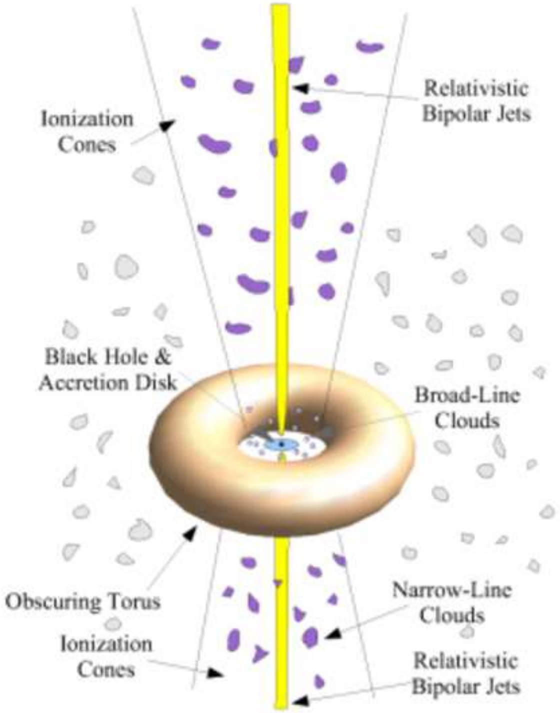

Figure 1.10: Sketch of the AGN structure. A very massive central black-hole ($10^6 \div 10^9$ $M_\odot$) surrounded by an accretion disk emits two relativistic bipolar jets where particles are accelerated up to the highest energy.

population of electrons. This model reproduces the observed spectrum up to 10^{15} eV but it becomes inefficient for higher energies. Models based on a hadronic origin of the observed gamma-rays can explain the more energetic region of the spectrum through the decay of the neutral pions in two high-energy photons. High energy neutrinos are expected to be produced by the charged pions. The expected neutrino flux from single bright AGN, in the range $10^3 \div 10^{11}$ GeV, is about 10^{-8} GeV cm^{-2} s^{-1} sr^{-1}, detectable with a km^3-scale neutrino telescope [25].

Cosmogenic neutrinos

A flux of ultra high-energy neutrinos is expected as a consequence of the interaction of UHE ($E_p \geq 10^{19}$) protons with the cosmic microwave background radiation (CMBR). The interaction of the UHE protons with the CMBR occurs mainly via the photo-production of the Δ^+-resonance $(p + \gamma) \longrightarrow \Delta^+$ (1232 MeV). The energy threshold for the Δ photo-production is $E_p \approx$

$$E_p > \frac{(m_\Delta^2 - m_p^2)}{2\epsilon} \approx 50\text{GeV} \tag{1.19}$$

where ϵ is the mean energy of the CMBR photons ($6.3 \cdot 10^{-4}$ eV) [26]. Considering a cross section $\sigma_{p+\gamma_{CMB}} \approx 10^{-28}$ cm^2, the proton absorption length in CMBR is

$$\lambda_{\gamma p} = (n_\gamma \sigma_{p+\gamma_{CMB}})^{-1} \approx 10 \text{ Mpc} \tag{1.20}$$

As consequence, a cut-off in the cosmic rays spectrum is foreseen for energy greater than energy threshold of the Δ^+ photo-production. This limit, calculated in 1966 by Greisen, Zatsepin and Kuzmin, is called GZK limit [27]. Apart from attenuating the flux of the primary particles, these processes give rise to secondary particles. Cosmogenic neutrinos resulting from $\Delta^+ \longrightarrow \text{N}\pi$ decay allow probing the GZK mechanism as well as spectra beyond the GZK cut-off. The energy spectrum of cosmogenic neutrinos is expected to span the range between approximately 10^{18} eV and 10^{21} eV. The expected neutrino spectrum depends on several factors such as the primary UHECR flux spectral index and composition as shown in Fig. 1.11 [28].

Although, recent results by AUGER confirmed the observations of HIRES, measuring a break in cosmic ray energy spectrum at 10^{20} eV, as expected in the GZK-model, further information is needed. In a scenario where the UHECR flux is dominated by heavier nuclei, as proposed by recent AUGER results [29], the flux suppression at extreme energy can be attributed to the limited acceleration power of the astrophysical source; and thus a low flux of cosmogenic neutrinos is expected.

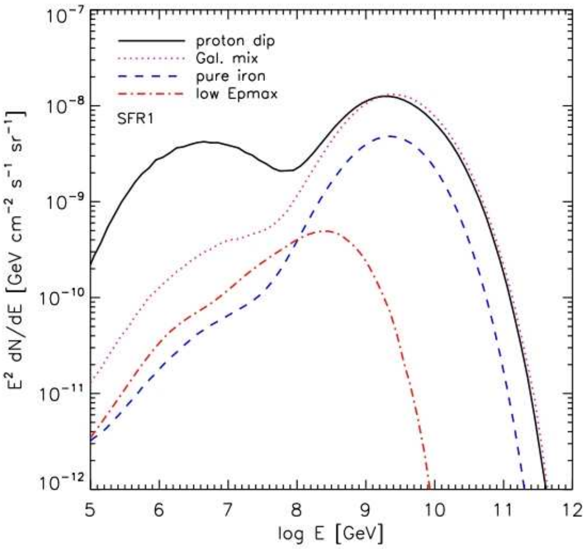

Figure 1.11: Neutrino GZK flux for different UHECR scenarios: pure proton injection scenario, assuming a dip transition mode (black line) proton dominated Galactic type mixed composition (pink dotted line); pure iron composition (blue dashed line) and iron rich low $E_{p_{Max}}$ model (red dash-dotted line) [28].

Chapter 2

High energy neutrino telescopes

Several experimental techniques are used and suggested to detect high-energy cosmic neutrinos, related to different neutrino energy ranges of interest. The detection volume of a neutrino detector is set by the estimated neutrino fluxes coming from astrophysical models and high energy extrapolation on neutrino-nucleon cross section. Some of the proposed detection technique for high-energy neutrino are described in the following sections.

2.1 Neutrino detection principles

High energy neutrino detection is based on the identification of the secondary charged particles produced in weak interactions of neutrino with the detection medium. Neutrinos can interact with a nucleon N of the medium via charged current (CC) or neutral current (NC) processes [30]:

$$\begin{array}{ll} \nu_l + N \rightarrow l^{\pm} + X & (CC) \\ \nu_l + N \rightarrow \nu_l + X & (NC) \end{array} \tag{2.1}$$

where neutrinos and anti-neutrinos are indicated with ν, l refers to the leptonic flavour and X represents nuclear debris. In the CC process, the output channel consists of a hadronic shower and a charged lepton, in the NC process only the hadronic shower is detectable. Neutrino interactions have been studied directly in laboratory experiments at CERN and BNL with neutrino beams produced in the interactions of high-energies protons with targets of Be or C up to energy $E_\nu = 300$ GeV [31]. For energy higher than 300 GeV, the neutrino interaction cross section is obtained by extrapolation, taking into account resonance effects, such as the resonant $W^{\pm}$ and Z^0 production ($E_{\bar{\nu}} = 47.4$ TeV) and the Glashow resonance, that refers to the formation of an intermediate W^- in $\bar{\nu_e} e^-$ collision at anti-neutrino energy $E_{\bar{\nu}} = 6.3$ PeV [32]. The Glashow resonance results in a notably high cross-sections for the allowed decay channels of the

W^-. Given a cross section $\sigma_{\bar{\nu}_e e^-} \approx 10^{-31}$ cm^2, the Glashow resonance, in spite of its narrow peak, may be an important discovery tool for the yet to be observed extra-galactic diffuse neutrino spectrum [33]. The neutrino-nucleon cross-section can be expressed as:

$$\frac{d^2\sigma_\nu}{dxdy} = \frac{2G_F^2 m_N E_\nu}{\pi}\left(\frac{M_W^2}{Q^2+M_W^2}\right)\left[x_q(Q^2,x)+x_{\bar{q}}(Q^2,x)(1-y^2)\right] \quad (2.2)$$

where G_F is the Fermi's constant (G_F=10^{-5} GeV^{-2}), q are the distribution functions of the quarks in the nucleon, M is the mass of the target, $M_{W(Z)}$ is the mass of the exchange boson ($W^\pm$ for CC interactions, Z^0 for NC interaction) and Q^2 is the invariant quadri-momentum transferred from the incoming neutrino to the outcoming lepton. The $x = Q^2/2M\varepsilon$ and $y = \varepsilon/E_\nu$ variables (with $\varepsilon = E_\nu - E_l$), are called Bjorken variables. They take into account the ratios of momenta and energies, that neutrino exchanges with the nucleons of the target. The cross section for *CC* and *NC* neutrino interactions are shown in Fig. 2.1 [34].

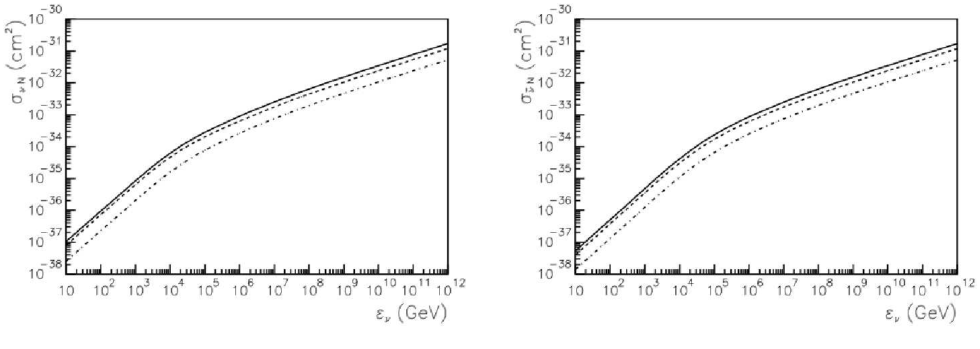

Figure 2.1: Neutrino-nucleon (left) and antineutrino-nucleon (right) cross section as a function of the neutrino energy for *CC* (dash-dotted line) and *NC* interactions (dotted line). The total cross-section is indicated with a solid black line [34].

The ratio of *CC* cross section on the total cross section is

$$\frac{\sigma_{CC}}{\sigma_{CC} + \sigma_{NC}} \simeq 0.7, \tag{2.3}$$

i.e. a charged lepton is produced in about 70% of the neutrino interactions. The mean value of the Bjorken variable y as a function of the energy is shown in Fig. 2.2. For interactions energies greater than 10^{15} eV, about the 80% of the neutrino energy is carried on by outcoming leptons, the remaining 20% is released to the hadronic shower produced in the interaction vertex.

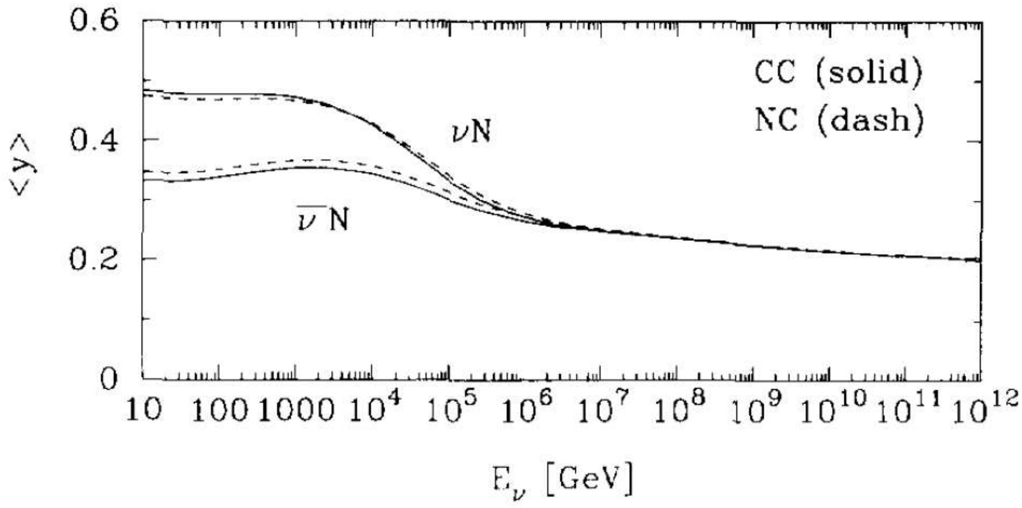

Figure 2.2: Mean value of the Bjorken variable y as a function of the neutrino energy. For energies greater than 10^{15} eV the fraction of the primary energy released to the hadronic shower is between 20% and 25%.

Cosmic neutrinos can be detected from their reaction products through different techniques (see Fig. 2.3). Each technique is related to a specific neutrino energy range. In the next sections the more exploited detection neutrino methods will be presented. In the UHE regime ($> 10^{17}$ eV), radio, extensive air shower and acoustic detection technique are proposed. Between 10^{11} and 10^{16} eV the Čerenkov technique is used.

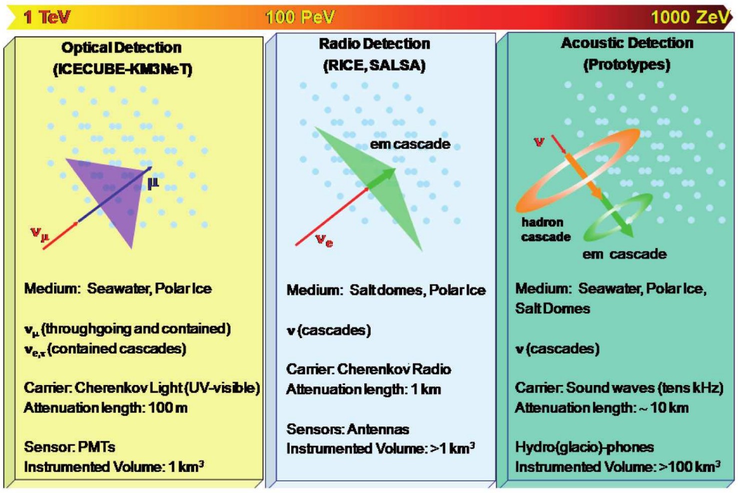

Figure 2.3: Detection techniques for high-energy astrophysical neutrinos as a function of the neutrino energy range [35].

2.2 Radio detection technique

The radio detection technique is based on the direct measurement of the electromagnetic signal emitted by the secondary charged particles produced by the neutrino interactions in the polar ice or in underground salt-domes. When a Ultra High Energy (UHE) neutrino interacts in the a dense dielectric, it produces, through the Askaryan effect, a shower of particles wherein the number of electrons exceeds the number of positrons by about ten percent, because of Compton scattered electrons and positron annihilation. The relativistic motion of this negative charge imbalance ΔQ in a volume of few cm^3, produces a coherent Čerenkov signal proportional to ΔQ^2, in the RF range $f \approx 100$ MHz $\div$ 1 GHz. Since ΔQ is proportional to the neutrino energy E_ν, the electromagnetic signal is proportional to ${E_\nu}^2$. Askaryan radio pulses produced by UHE neutrino interaction in ice can be detected using an array of radio receivers buried in bulk ice. The RICE (Radio Ice Čerenkov Experiment) experiment, consisting of a 20-channel array of dipole radio receivers, located at the South Pole at 100 - 300 m depths, has accumulated data from 1999 to

2005. An upper limit of $E^2\ \Phi(E) = 6 \cdot 10^{-7}$ GeV cm^{-2} s^{-1} sr^{-1} on the incident neutrino flux in the energy regime between 10^{17} eV and 10^{20} eV has been established [36]. Following the RICE experience the AURA (Askaryan Under-ice Radio Array) detector was deployed on top of Ice-Cube strings at depths of 1450m and 250 m [37]. In the South Pole another project based on the Askaryan effect has been developed, called ANITA (Antarctic Impulsive Transient Antenna). ANITA is a Long Duration Balloon (LDB) experiment that flew above the South Pole in three different flights. The ANITA experiment aimed at the detection of neutrino-induced radio pulses emerging from the polar ice-cap. ANITA set a 90% C.L. integral flux limit on a pure E^{-2} spectrum for 10^{18} eV $\leq E \leq 10^{23}$ eV equal to $\mathrm{E}_\nu^2 F_\nu \leq 2 \cdot 10^{-7}$ GeV cm^{-2} s^{-1} sr^{-1}. This is the strongest constrain, to date, on the cosmogenic UHE neutrino flux [38].

2.3 Extensive air shower detection

Another method to detect UHE neutrinos is the reconstruction of quasi-horizontal extensive atmospheric showers, initiated by CC or NC neutrino interaction in very deep atmosphere (close to ground). Identification of neutrino-induced showers is based on the idea that neutrinos can penetrate large amounts of matter and generate "young" inclined showers developing close to the ground. Unlike the showers induced by charged particles, that produce a narrow signal in time on the surface array detectors, a broad signal is expected from a neutrino-induced shower. Analysis of atmospheric showers reconstructed by the surface array detector of Auger in the energy range 10^{17} eV $\div$ 10^{19} eV is on going [39]. Another method to detect UHE neutrinos consists in looking at up-going showers in atmosphere initiated by the decay products of an emerging (Earth-skimming) τ lepton, originated in the interaction of an upgoing or Earth-skimming ν_τ close to the Earth surface or inside a mountain [40] These showers produced by the decay of τ in the atmosphere can be observed by air fluorescence detectors, such as HIRES [41] and Auger-FD, or surface detector, such as Auger-SD.

2.4 Thermo-acoustic detection technique

A promising method to detect Ultra High energy neutrinos is based on the thermo-acoustic model. This detection technique, that is one of the main topics of this PhD thesis, will be described in more details in Chapter 3. Following the hadronic interaction of an Ultra High Energy neutrino (E $\geq 10^{18}$ eV) in water, a large amount of the neutrino energy is deposited in a small pen-shaped volume of few tens metres in length and few centimetres in radius. Instantaneous ionization of water produces heating, thus, a bipolar acoustic pulse, detectable by means of acoustic sensors, called hydrophones [42]. The expected number of such events is very small, order of few in 10 km^3 of water per year. Thus, very large acoustic arrays are required. The first efforts to develop and built acoustic array for neutrino detection are reported in Chapter 3.

2.5 Cherenkov detection technique

The most widely exploited method to detect astrophysical neutrinos in the energy range $E_\nu = 10^{11} \div 10^{16}$ eV is based on the detection of the Čerenkov light induced by the charged leptons produced in the neutrino interactions within large volumes of water or ice. Given the expected neutrino flux at Earth and the neutrino-nucleon cross section, very large detection volumes (≥ 1 km^3) have to be used. In the 1950s the Russian physicist Markov proposed for the first time the use of large homogeneous volumes of natural elements, such as seawater or polar ice [43] [44]. Sea water and ice act both as radiator for the Čerenkov light and as a shield for atmospheric muons. The layer of water or ice above the detector absorbs the abundant low-energy component of the atmospheric muons, generated by the interactions of the cosmic rays with the atmosphere. At a depth of 3000 m the atmospheric muon flux is reduced by a factor 10^6 with respect to the flux at the surface [45]. Since neutrino is the only Standard Model particle that can cross unabsorbed the Earth diameter, neutrino events are unequivocally identified, by discriminating the muons coming from below the detector (*up-going*). Underwater Čerenkov neutrino telescopes are affected mainly by two kinds of background: a irreducible background due to atmospheric neutrinos and the background due to atmospheric muons, that are wrongly reconstructed as *up-going*. Since the expected neutrino flux is extremely low, it is crucial to reduce, as much as possible, the contribution related to *down-going* muon flux.

The Čerenkov light is detected by an array of high sensitivity optical sensors, typically photomultiplier tubes (PMT), filling the detector volume, distributed at average inter-distances of some tens of meters. The golden channel for the neutrino detection occurs in case of charged current neutrino interaction with muon production. In the energy range of interest the outcoming muon can propagate in the detection medium for several kilometres and cross the detector. This results in the possibility to detect neutrino events generated in a volume much larger than the physical dimension of the detector. Moreover, accurate geometrical reconstruction of the track is possible. The differential loss of energy of the muon in the medium is given by

$$-\frac{dE}{dx} = a + b \cdot E_{GeV}, \tag{2.4}$$

where $a = 0.2$ GeV/m and $b = 4{\cdot}10^{-4}$/m (the muons release about 0.25 GeV per m in water) [46]. A small fraction of energy of the muon is released via Čerenkov photons, that propagate in water at a characteristic angle with respect to the relativistic muon direction:

$$\theta_c = cos^{-1}\frac{1}{n\beta}, \tag{2.5}$$

depending by the refraction index n (in sea-water $n= 1.33$) and the ratio β of the muon velocity v to the speed of light c [7].

The number of the photons emitted by the muons travelling through the detector per unit of length dx depends on the photons wavelength λ as:

$$\frac{d^2N}{dxd\lambda} = \frac{2\pi\alpha Z^2}{\lambda^2}\left(1 - \frac{1}{n^2\beta^2}\right), \tag{2.6}$$

where Z is the charge of the radiating particle, that is $Z_\mu = 1$, and α is the fine-structure constant [47]. In seawater, the largest part of the Čerenkov emission occurs in the blue-UV range of the electromagnetic spectrum. In this range the number of radiated photons is

$$\frac{dN}{dx} \approx \text{ 300 photons/cm.} \tag{2.7}$$

Given this small amount of light, PMTs have to be placed in such a way that the average distance between optical sensors should not exceed 2 times the light absorption length in the medium. Seawater is transparent only to a narrow range of wavelengths (350 nm $\leq \lambda \leq$ 550 nm). The blue light attenuation length is about 70 m for clear ocean water [48], while in ice deep polar ice it is about 100 m [49]. So, more than 5000 optical sensors are needed to instrument a km^3-scale Čerenkov telescope. Muon track reconstruction is performed during offline analysis of space-time correlated PMT signals. The arrival time t of the Čerenkov photons emitted along the muon track on the PMTs with respect to a initial time t_0 is given by the causality relation:

$$t = t_0 + \frac{l}{c} + \frac{2k}{c \cdot sin(2\vartheta_C)} \tag{2.8}$$

as shown in Fig. 2.4, where l is the projection of the PMT position along the muon track at distance k, ϑ_C is the Čerenkov angle and c is the speed of light in seawater.

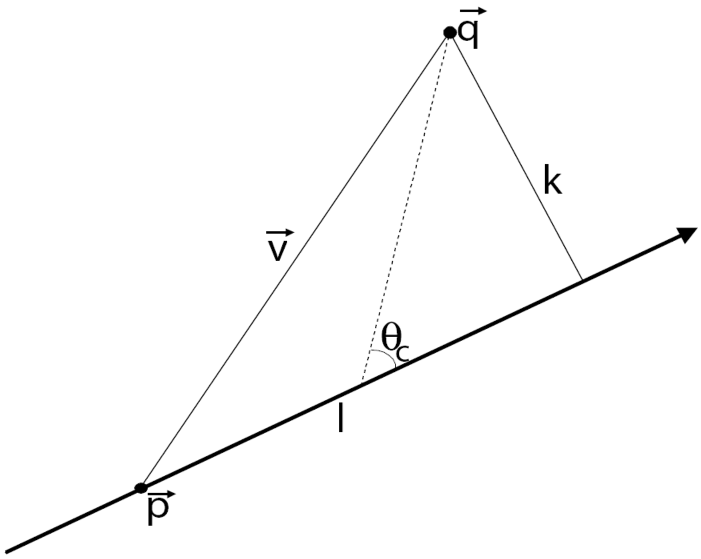

Figure 2.4: Schematic view of the detection principle of a Čerenkov neutrino telescopes. The muon track is reconstructed by correlating the time of arrival of the Čerenkov light emitted by the muon to the optical sensors of the detector. The positions of the muon and the PMT are indicated respectively with $\overrightarrow{p}$ e $\overrightarrow{q}$, l is the component along the muon direction of the vector $\overrightarrow{v}=\overrightarrow{q}-\overrightarrow{p}$, k is the minimum distance between the track and the sensor, ϑ_C indicates the Čerenkov angle in sea water.

The reconstruction of the muon track permits the identification of the neutrino arrival direction. Indeed, for $E_\nu \geq 1$ TeV the secondary muon and primary neutrino are almost collinear. The mean angle between the muon and the incoming neutrino depends on the neutrino energy and it is about $0.7°/(\mathrm{E}_\nu/\mathrm{TeV})$ [47].

Since the neutrino and the secondary muons are almost collinear, the muon track reconstruction allows the search of point sources of cosmic neutrino for the production of a neutrino sky map. The detection of electron and tau neutrinos is also possible in telescopes optimised for muon neutrino detection but the detection efficiency for these neutrino types is lower. Electron and tau neutrinos are detected through the Čerenkov light radiated by the hadronic and electromagnetic showers produced in the interaction vertex. Since the showers propagate for a few tens of meters [50], their light tracks are too short to be detected and well-reconstructed by a sufficient numbers of PMT. The first efforts to build an underwater neutrino detector have been lead by the DUMAND Collaboration [51] between 1980 and 1995 off the coast of Hawaii, but the project was cancelled because, at the time, the deep-sea technology was not sufficiently advanced to perform this challenge. Important steps towards the Čerenkov neutrino construction has been taken by the end of the 1990s with the construction of the Baikal NT-200 [52] and AMANDA [53] detectors, that allowed a measurement the atmospheric muons spectrum up to TeV energies. NT-200 was deployed in the water of the Baikal lake (Russia). AMANDA was installed in the polar icecap of Antarctica. AMANDA was the prototype for IceCube neutrino telescope.

2.5.1 IceCube

IceCube is the first km^3-scale neutrino telescope in operation. It is accomplished at the end of 2010 and consists of 5160 digital optical modules (DOMs) deployed on 86 vertical strings, buried at $1450 \div 2450$ meters under the surface of the ice. Each string contains 60 DOMs, placed at a verticals distances of 17 m. The strings are connected to a counting house placed on the surface, at the center of the array, by means electro-optical cables. As shown in Fig. 2.5, the detector includes 6 additional strings, located in the clear ice of the bottom center of the telescope, that,with the 7 central IceCube strings, form a “compact” sub-detector, called DeepCore [54]. DeepCore enhances the sensitivity of IceCube for low neutrino energies down to $\sim$ 10 GeV, probing a range of parameters of Dark Matter models not covered by accelerator- based experiments. Moreover, DeepCore allows atmospheric neutrino oscillation measurement from muon neutrino disappearance or tau neutrino appearance in an energy region not well tested by beam-experiments. IceCube includes also IceTop, an array of detectors placed in the ice-cap surface. IceTop consists of 160 ice tanks, equipped with 2 DOMs , at a mean distance of 125 m. This spacing allows the observation of cosmic rays shower in the energy range $10^{14} \div 10^{17}$ eV. IceTop is also used as veto for the down-going background of atmospheric muons.

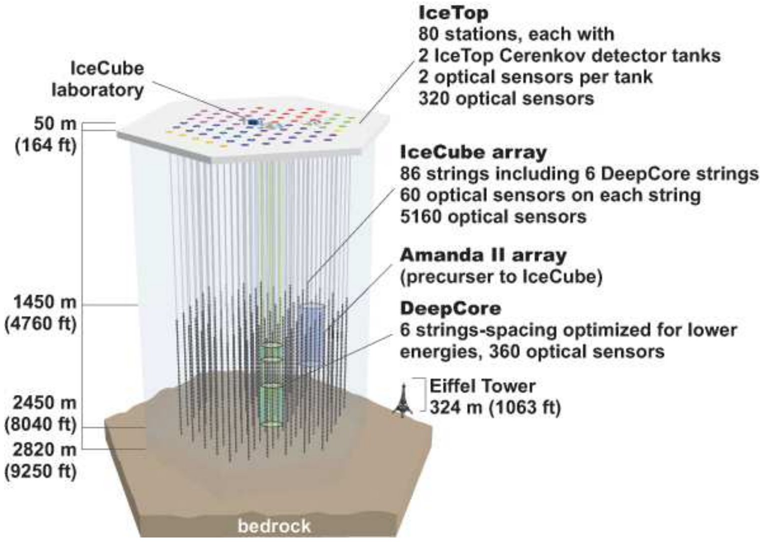

Figure 2.5: Three-dimensional view of the IceCube detector layout.

From the analysis of data collected in the half completed configuration (40-string) of the IceCube detector, which operated between April 2008 and May 2009, no evidence for a diffuse flux of astrophysical neutrinos was found. In Fig. 2.6 the corresponding 90% upper-limits on muon neutrinos diffuse flux derived by data analysis are compared to other limits and flux models [24].

Data analysis excluded, also, with a confidence of 90% the more accredited predictions of neutrino-flux from GRBs based on fireball model [55]. Since IceCube, situated at the South Pole is sensitive mainly to upward-going neutrinos, originated in the Northern sky, most of the Galactic plane, including the Galactic Centre, is not visible by the de-

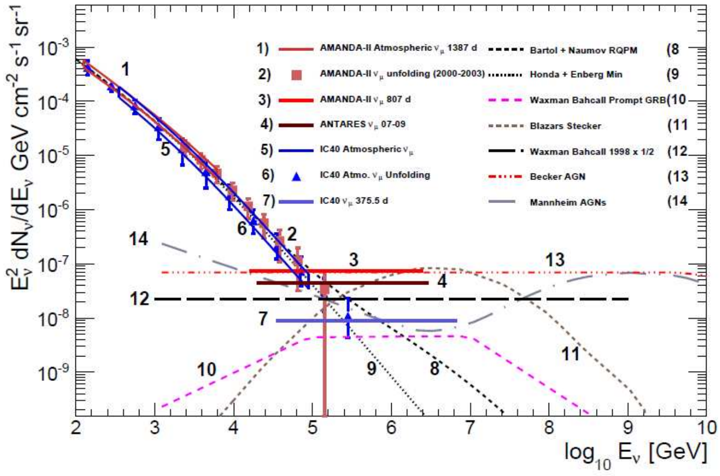

Figure 2.6: Upper limits on astrophysical muon neutrino flux with an E^{-2} spectrum derived by the IceCube 40-string configuration data (IC40 ν_μ 375.5 d) compared with the upper limits from AMANDA-II, ANTARES and with theoretical model predictions of diffuse astrophysical muon neutrinos from different sources. The atmospheric ν_μ measurements from AMANDA and IceCube 40-string are shown as well [24].

tector. For a full sky coverage an additional neutrino telescope in the Northern hemisphere is required and proposed by the scientific community.

2.5.2 KM3NeT

In order to explore the sky-region uncovered by the IceCube telescope, a large European collaboration is working to design and construct a large underwater neutrino telescope in the Northern hemisphere, called KM3NeT [56]. The KM3NeT neutrino telescope will be located in the Mediterranean Sea, at a latitude λ between 36° and 43° North. At this latitude most of the sky (about 3.5 π sr) is visible through upward-going neutrinos. Declinations below -90° + λ are always visible, while those above 90° - λ are never visible. Declinations between these two values are visible for part of the sidereal day as shown in Fig. 2.7 [57].

The detector design presented by the KM3NeT Collaboration [58] is

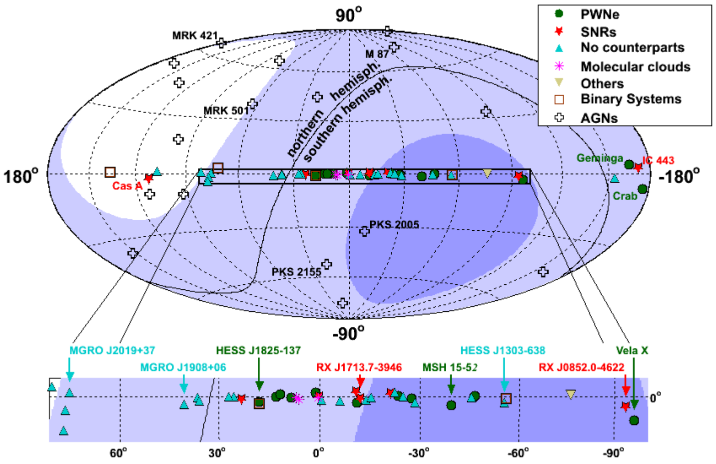

Figure 2.7: Sky coverage in Galactic coordinates for a detector located in the Mediterranean Sea and at the South Pole. The shading indicates the visibility for a detector in the Mediterranean with 2π downward coverage; dark (light) areas are visible at least 75% (25%) of the time. The main high-energy gamma sources are also indicated [57].

optimised for the detection of neutrino point-like sources with a power law energy spectrum E_ν^{-2} in the TeV-PeV energy range. The KM3NeT design is based on detection units (DUs), used to mechanically sustain OM, built with PMTs. The detector will consist of modular blocks of about 150 DUs arranged on the seabed in a roughly circular layout. In each block, the DUs have an average distance of about 150 m. Different mechanical designs have been proposed for DU. In the "tower" layout, each DU is a sequence of 20 rigid bars, $6 \div 8$ m long, placed orthogonally to each other with a vertical spacing of 40 m. Each bar is equipped with 6 optical modules hosting a large area (10" diameter) PMT, or with 2 multi-PMT DOM, that is an optical module containing smaller PMTs with a diameter of about 3 inch. In Fig. 2.8 the expected discovery flux and sensitivity of the full KM3NeT detector to neutrino point sources with an E^{-2} spectrum for one year of observation, as a function of the source declination, is shown.

KM3NeT profits from the technological experience accumulated within

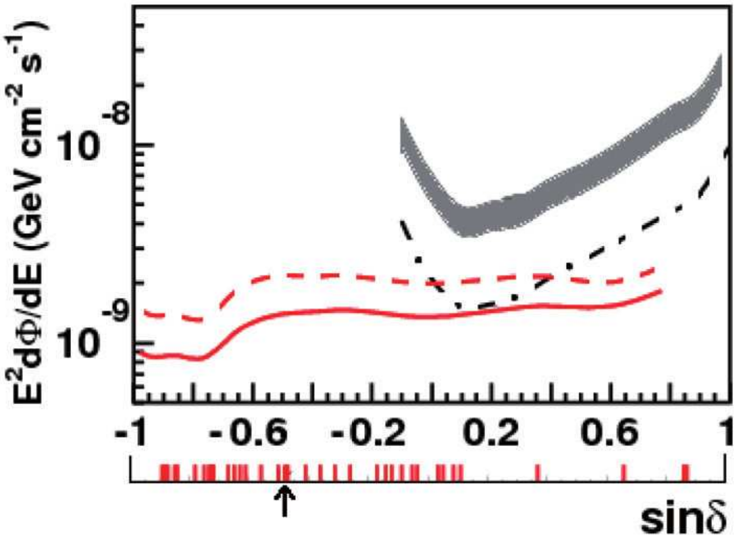

Figure 2.8: Discovery flux (5σ, 50% probability; dashed red line) and sensitivity (90% confidence level; full red line) of the KM3NeT detector to neutrino point sources with an E^{-2} spectrum for one year of observation, as a function of the source declination. For comparison IceCube discovery flux (5σ, 50% probability;shaded grey band) and sensitivity (90% confidence level; dash-dotted black line) are also indicated.

the three pilot neutrino telescope projects operating in the Mediterranean Sea: NESTOR [59], ANTARES [60] and NEMO [61], described in the following sections.

NESTOR

The NESTOR Collaboration was the first experimental group that worked on the design of an underwater neutrino telescope in the Mediterranean Sea. The proposal of the NESTOR Collaboration is a modular detector to be installed at depths $\geq$ 3800 m in the Ionian Sea, off the coast of Greece. Each module consists of 12 hexagonal mechanical structures with a diameter of 32 m, called floors, spaced by vertical intervals of 20 m. Highly sensitive photomultipliers of large surface area are installed at the corner points of the mechanical structures. A first prototype of a module has been deployed in 2003 at a depth of 3800 m. From data collected in about a month of activity, the cosmic ray muon flux as a function of the zenith angle was measured [62].

ANTARES

The ANTARES neutrino telescope is the largest neutrino detector in the Northern hemisphere, located about 40 km from Toulon off the Southern French coast at a depth of 2000-2475 m. The detector has been completed in June 2008 and it comprises 885 optical modules distributed over twelve detection lines, covering a surface area of 0.1 km^2. Each detection line is equipped with 25 storeys consisting of 3 pressure-resistant Optical Modules, each one containing a 10" down-looking PMT oriented at 45°. The detection lines are interlinked in a Junction Box connected through 45 km long electro-optical cable to the shore station at La Seyne sur Mer (close to Toulon, France). Using a full detector simulation, an average angular resolution of $0.5° \pm 0.1°$, defined as the median angle between the neutrino and the reconstructed muon direction, has been determined for a E^{-2} neutrino spectrum. A search for cosmic sources of muon neutrinos has been carried out using data collected in the years between early 2007 until the end of 2010, corresponding to an integrated live time of 813 days. Data collected by the ANTARES telescope set the strongest upper limits to neutrino flux for the Southern sky, and competitive with those set by the IceCube observatory for declinations $\delta \leq$ -30°, as shown in Fig. 2.9 [63].

NEMO

The NEMO Collaboration is carrying out, since 1998, an R&D program for the construction of a km^3 scale underwater detector for astrophysical neutrinos in the Mediterranean Sea at depths greater than 3000 m. The main activities performed by the NEMO Collaboration were: the search and characterization of an optimal deep sea site , the

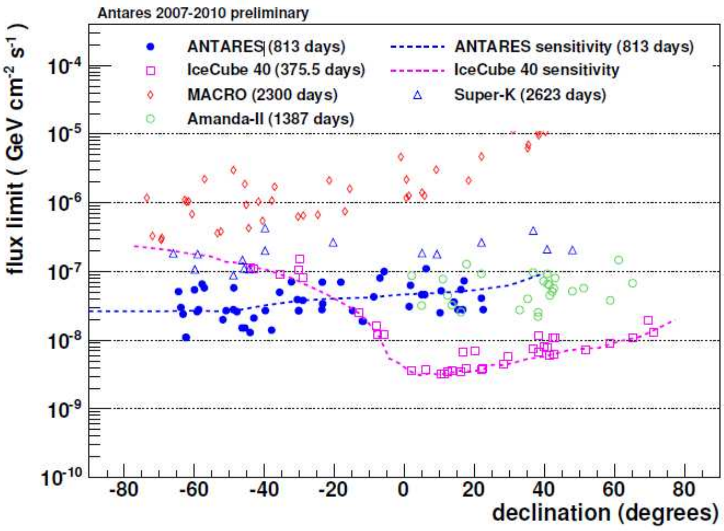

Figure 2.9: Preliminary flux limit (90% C.L.) as a function of source declination for a list of 50 potential neutrino sources assuming an E^{-2} spectrum obtained by the ANTARES telescope (blue dots). The sensitivity (blue dashed line) is given as the median of the flux limits for the tested sources. For comparison, the flux limits set by various experiments are shown, as well [63].

development of key technologies for the construction and installation of a km^3 underwater telescope, the study of detector architecture based on technological issues and physics performances. In order to validate the technologies developed for the realization of the km^3 detector in deep sea environment, the NEMO Collaboration built and operated in 2006 a fully equipped test facility, deployed at the underwater Test Site of the Laboratori Nazionali del Sud, 25 km off-shore Catania (Sicily), at 2000 m depth. The infrastructure includes all the key elements of a km^3 neutrino detector: a shore station, an electro-optical deep-sea cable, a junction box (JB), that provides the distribution of power and data from and to shore, and a small-scale detector prototype composed of a sequence of 4 horizontal structures (floors) mechanically interconnected by means of synthetic fibre ropes. Down-going atmospheric muons have been observed and their tracks have been reconstructed. The vertical muon intensity as a function of depth has been measured and the collected data are in good agreement with the theoretical predictions and previous results (Fig. 2.10) [64] [65].

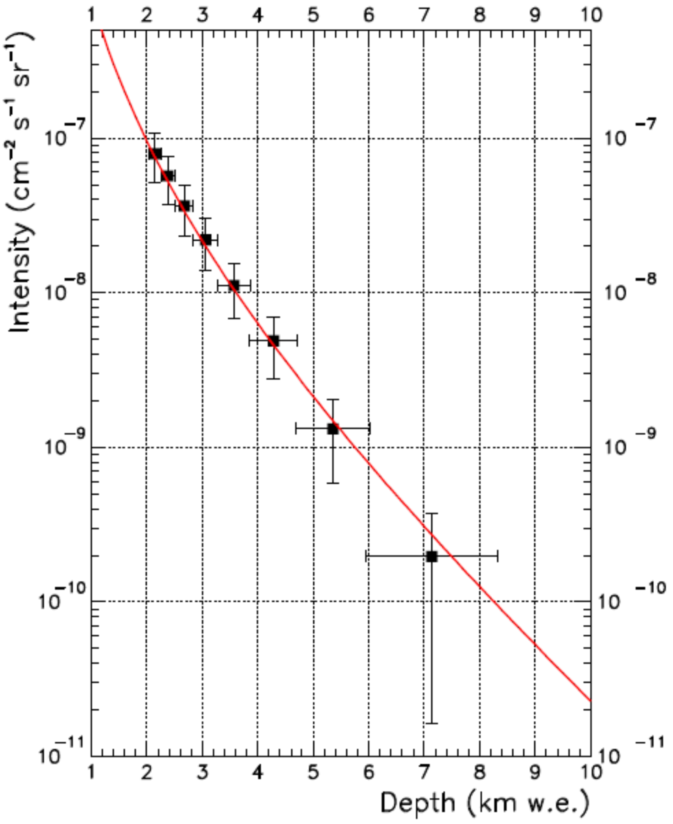

Figure 2.10: Vertical muon intensity versus depth. The solid lines gives the prediction of Bugaev et al. [64] [65].

The NEMO Test Site infrastructure is nowadays used to host multidisciplinary experimental activities, as described in Chapter 7. A new project, called NEMO Phase-II, is nowadays conducted by the Collaboration. Phase-II aims at the tests the technologies proposed for the construction of the KM3NeT detector at depth of 3500 m in the Capo Passero Site. The project foresees the operation of a fully instrumented detector unit prototype, in Capo Passero Site by the first months of 2013.

The completion of Phase-II will fully establish the technology for deployment and connection and, at the same time, set-up a continuous long term on-line monitoring of the site seawater properties, whose knowledge is essential for the installation of the full km^3 detector. NEMO Phase-2 hosts also the SMO acoustic detector. A detailed description of the NEMO Phase-2 and SMO projects is given in Chapter 4 and Chapter 5 of the thesis.

Chapter 3

Neutrino acoustic detection

One of the most promising methods to detect neutrinos with energy higher than 10^{18} eV is based on the detection of acoustic waves produced by deposition of a large amount of energy following a UHE interaction of neutrinos in sea/lake-water. Thanks to the long attenuation length of the acoustic waves in water, the acoustic detection technique permits to instrument very large detection volumes with a sparse array of acoustic sensors. In this chapter the thermo-acoustic technique will be described and a brief overview of the main pilot experiments on acoustic detection will be presented.

3.1 The thermo-acoustic model

The acoustic detection technique, first proposed by Askaryan in 1957, is based on the so called thermo-acoustic model [66]. Following the interaction of a UHE neutrino in seawater, a hadronic shower develops at the interaction vertex at the speed of light. The shower carries about 25% of the neutrino energy, releasing a macroscopic amount of energy in the medium by ionisation processes. The energy, deposited in the medium, can be dissipated through different mechanisms: heat conduction, viscous friction and thermo-acoustically. Considering that the characteristic time of the heat conduction and viscous friction are much bigger than the characteristic time for a pressure wave propagation in water, it is safe to assume that the dissipation of the shower energy occurs mainly by pressure wave propagation. The pressure amplitude of the produced acoustic wave in the position $\overrightarrow{r}$ and at the time t can be described by the following wave equation [67]:

$$\frac{1}{c_s^2}\frac{\partial^2 p(\overrightarrow{r},t)}{\partial t^2} - \bigtriangledown^2 p(\overrightarrow{r},t) = \frac{\beta}{C_p}\frac{\partial^2 E(\overrightarrow{r},t)}{\partial t^2}, \qquad (3.1)$$

where p is the deviation from the hydrostatic pressure , c_s is the sound velocity in the medium, E is the energy deposition in form of heat, β is the expansion coefficient of the medium and C_p is the specific heat capacity at constant pressure.

The Eq. 3.1 can be solved using the Kirchhoff integral:

$$p(\overrightarrow{r},t) = \frac{\beta}{4\pi C_p}\int \frac{dV'}{|\overrightarrow{r}-\overrightarrow{r}'|}\frac{\partial^2}{\partial t^2}E\left(\overrightarrow{r}',t-\frac{\overrightarrow{r}-\overrightarrow{r}'}{c_s}\right) \tag{3.2}$$

Decomposing the energy deposition into a temporal and a spatial parts and assuming an instantaneous energy deposition, we have:

$$E(\overrightarrow{r},t) = E_r(\overrightarrow{r})\Theta(t-t_0) \tag{3.3}$$

where Θ is the Heaviside step function and t_0 the time of the energy deposition.

From (3.3) it follows:

$$\frac{\partial}{\partial t}E(\overrightarrow{r},t) = E_r(\overrightarrow{r})\delta(t-t_0) \tag{3.4}$$

Including (3.3) and (3.4) in the Kirchoff integral (3.2) we obtained:

$$p(\overrightarrow{r},t) = \frac{\gamma}{4\pi}\frac{\partial}{\partial R}\int_S \frac{E_r(\overrightarrow{r}')}{R}d\sigma \tag{3.5}$$

where the integration is performed over spherical shells of radius $R = c_s t$ centred on $\overrightarrow{r}$. The acoustic pressure in r at time t results from the sum of all contributions that can reach this point propagating at the speed of sound.

The term $\gamma= \beta c^2/C_p$ is called Gruneisen parameter. It depends in the thermo-acoustic properties of the medium and it is related to the maximum amplitude of the acoustic pulse. The γ parameter expresses the conversion efficiency of the thermal energy into acoustic pressure. The dependence of the Gruneisen parameter on depth for different waters is shown in Fig. 3.1.

In a more realistic case, in which the energy deposition is not instantaneous, the first time derivative of the energy density is gaussian like

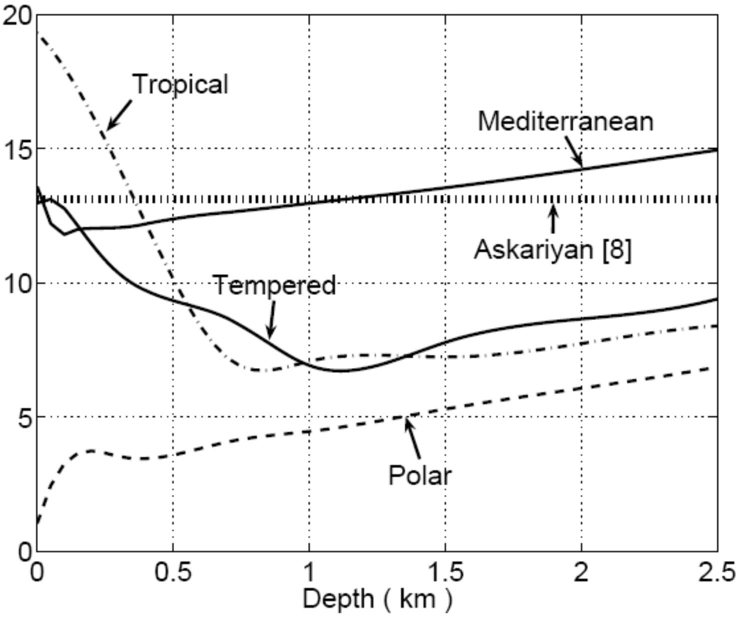

Figure 3.1: Gruneisen parameter value expressed in % for different waters as a function of the depth. The value expresses the conversion efficiency of the thermal energy into sound.

and the solution of (3.1) for $\overrightarrow{r} \approx 0$, as shown by Learned in [68], can be written as:

$$p(\overrightarrow{r} \approx 0, t') = -\frac{E\beta}{4\pi C_p r}\frac{t'}{\sqrt{2\pi}\sigma^3}e^{-\frac{t'^2/\sigma^2}{2}}, \tag{3.6}$$

with $t' = t - r/c$.

This solution shows a typical bipolar behaviour, as shown in Fig. 3.2.

Acoustic pulses from particle showers were first observed at Brookaven NL in 1979 [69], using a beam of 200 MeV protons with a total energy deposition in water from 10^{19} eV to 10^{21} eV. A bipolar pulse has been observed as expected by the thermo-acoustic model, with a clear dependency of the signal amplitude on energy E, volume expansivity K, specific heat C_p and beam diameter. Test measurements carried out in

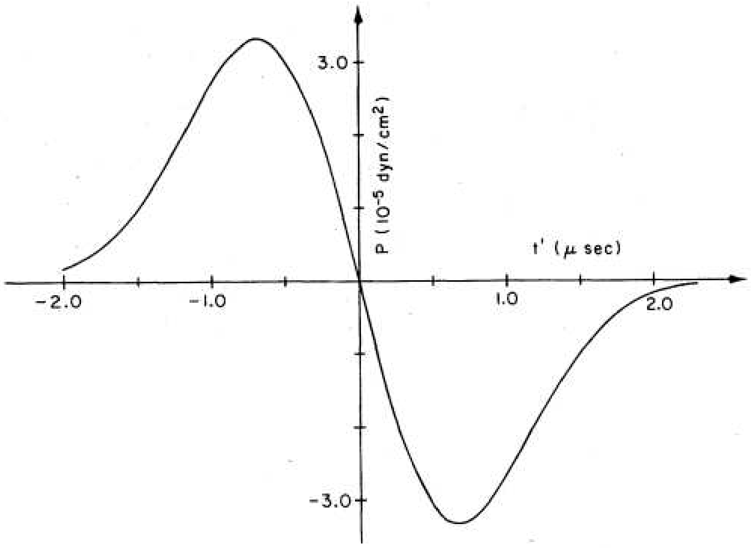

Figure 3.2: Acoustic bipolar pulse obtained by a Gaussian time distribution of heat in a point-like region [68].

the recent years with intense laser and proton beams have confirmed the thermo-acoustic sound generation in water [70]. The measurement are in good agreement with simulation and theoretical predictions. Fig. 3.3 shows the comparison between experimental data collected at ITEP (Institute of Theoretical and Experimental Physics) accelerator facilities in Moscow by using a proton beam with an injection energy of 200 MeV and a radius of 5 centimetres and simulation [71].

3.2 Landau-Pomeranchuk-Migdal effect

As described in Section 2.1, in the neutrino-nucleon interaction a fraction of the neutrino energy is released though electromagnetic or hadronic shower. In case of CC interactions of electron neutrino, about 80% of the incident neutrino energy is retained by the lepton (see Fig. 2.2). Nevertheless, for UHE neutrino the thermo-acoustic process is more efficient in case of hadronic shower. Indeed, for energy greater the 10^{17}

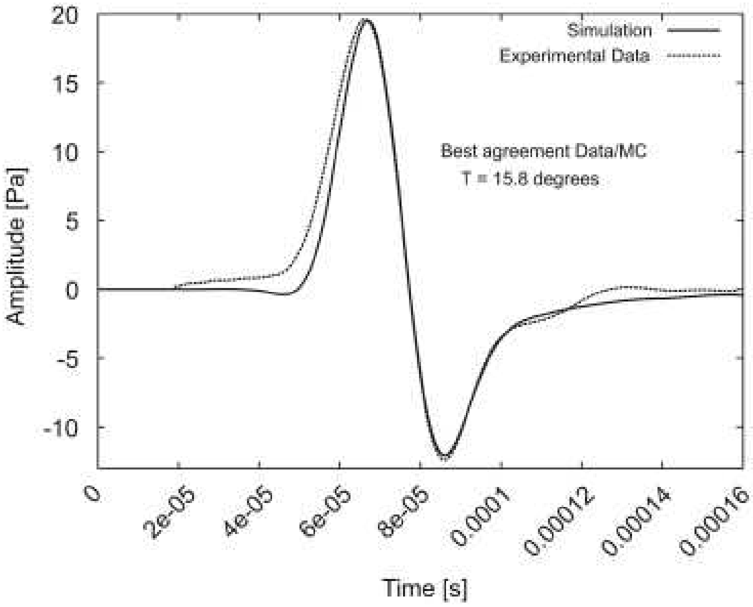

Figure 3.3: Comparison between experimental data and simulation. The experimental data has been collected at ITEP by injecting bunches of 200 MeV protons in a water tank [71].

eV, the cross sections for bremsstrahlung and pair production decrease as $\sqrt{E}$. This effect is called LPM by the names of the scientists Landau, Pomeranchuk and Migdal. They noticed that as the energy increases the inter-atomic distance, seen in the frame of reference of the ultra relativistic particle, decreases until distance is comparable with the wave packet length of the particle and the scatterings can no longer be treated as independent events. As a consequence, the interaction length starts to increase for the destructive quantum interference effects from multiple scattering centres and the longitudinal profile of the cascade becomes longer. At energy above the LPM threshold (about 10^{17} eV for electron neutrinos), the energy density along the shower no longer increases linearly with the primary neutrino energy. Simulations on the development of neutrino-induced electromagnetic showers as a function of neutrino energy are reported in Fig. 3.4 [72]. As a consequence of the LPM effect, the acoustic signal amplitude produced by electromagnetic showers, despite electrons carry in average more energy, are comparable or lower than to the hadronic ones.

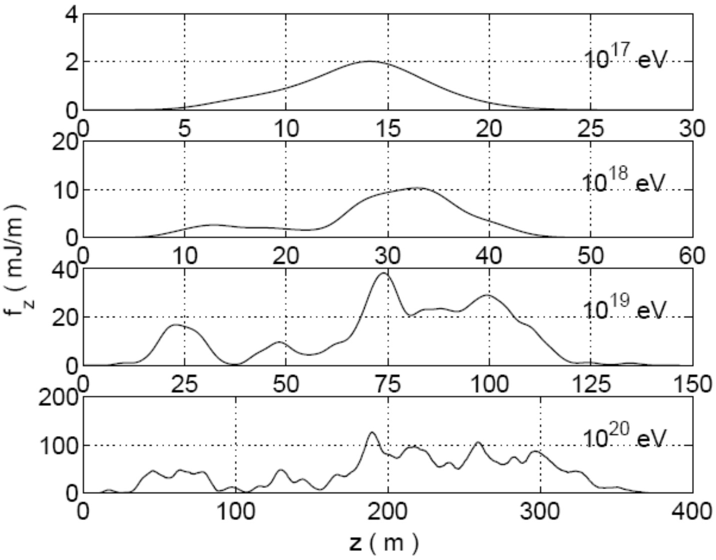

Figure 3.4: Simulations on longitudinal development of the energy density in a neutrino-induced electromagnetic shower for different neutrino energies [72].

3.3 Neutrino acoustic signal

As discussed before, for hadronic showers induced by interactions of high energy neutrinos in water, about 20% in average of the incident neutrino energy is deposited in a cylindrical volume of water of some tens centimetres radius and few tens of meter length. According to Learned work [68], a bipolar acoustic pulse is expected, following the second time derivative of the energy density deposited in the excited medium. Since the power spectral density of the resulting acoustic signal is related to the radial energy deposition in the shower with a transverse spread of few centimetres, the maximum acoustic amplitude is expected at frequency of few tens kHz. The amplitude of the bipolar signal is proportional to the deposited energy density and to the Gruneissen parameter of the medium γ. For deep Mediterranean-Sea water γ is about 0.12. At ultra high energy the shower dimension increase only logarithmically with energy, so the amplitude of the acoustic signal roughly depends linearly on the neutrino energy. The expected acoustic pulse amplitude p_{max} at 1 km produced by a neutrino of energy E_ν in the Mediterranean water is [42]:

$$p_{max} \approx 6 \cdot 10^{-21} \cdot E_\nu [Pa/eV] \,.(3.7)$$

Another feature of the acoustic signal produced by a shower is, indeed, its angular pattern. The nearly simultaneous sound production along the shower track results in a coherent emission in the plane perpendicular to the shower axis. The process of coherent sound emission can be treated in analogy to the Fraunhofer diffraction from a slit of finite size. The sound emitted by two parts of the cylindrical cascade, at distance d, will interfere destructively if the path difference $dsin(\theta)$ is equal to $\lambda/2$, with λ the acoustic wavelength of the emitted pulse. In the "far field" approximation, for a each component $f = c_s/\lambda$ of the signal spectrum the signal amplitude as a function of the azimuth angle $I(\theta)$ is:

$$I(\theta) = I_0 \left(\frac{sin\left(\frac{\pi d}{\lambda} sin(\theta)\right)}{\frac{\pi d}{\lambda} sin(\theta)} \right)^2 , \tag{3.7}$$

where I_0 is the maximum amplitude, related to direction perpendicular to the shower. The far field radiation pattern for a neutrino event is obtained by integrating the contributions from all components of the signal spectrum. Fig. 3.5 reports the expected pressure amplitude for a hadronic shower induced by a neutrino with an energy of 10^{20} eV [73]. Fig. 3.6 shows the shape as a function of time and the amplitude of the acoustic signal as a function of the azimuth emission angle θ, assuming a cylindrical distribution of energy density in the medium [74].

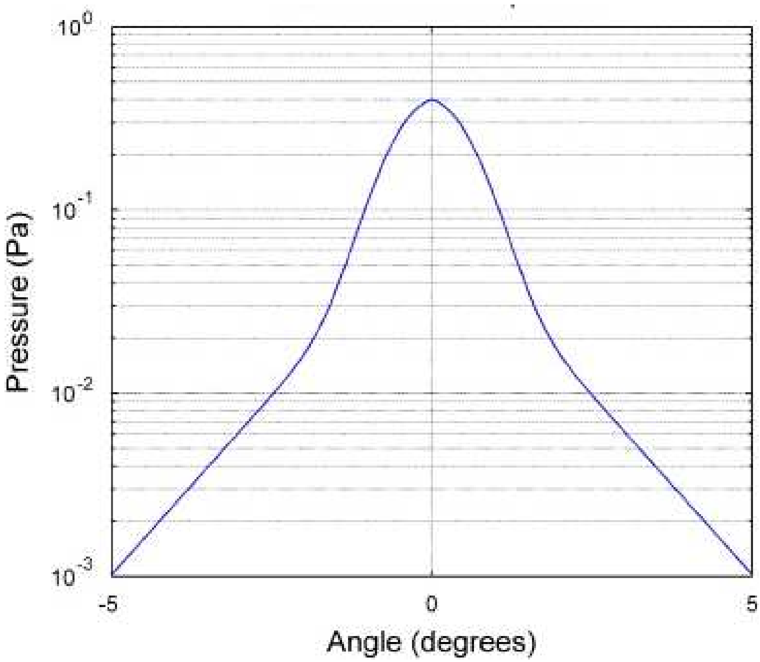

Figure 3.5: Far-field radiation pattern as a function of the emission angle from the plane perpendicular to the neutrino direction. [73].

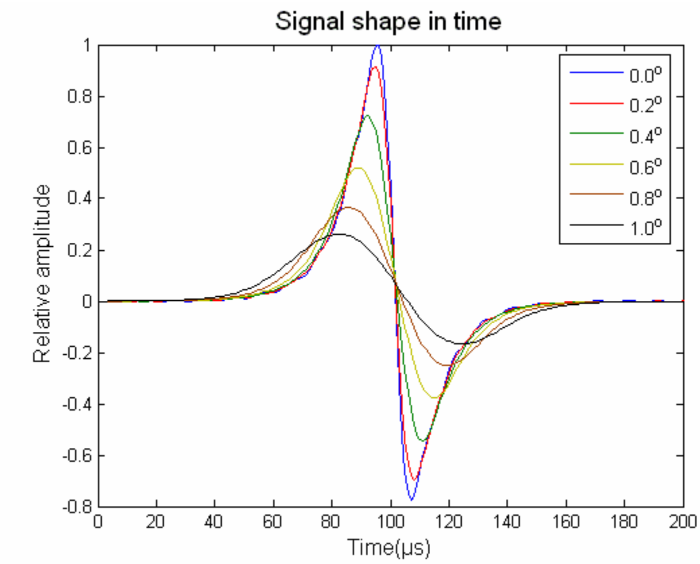

Figure 3.6: Shape in time of the acoustic signal as a function of the azimuthal angle of emission [74].

3.4 Sound propagation

The neutrino acoustic signal, after its generation, propagates through the underwater environment. Due to the characteristics of the medium, the signal suffers both geometrical attenuation and absorption processes related to the salts dissolved in the seawater. The geometrical attenuation can be calculated from the energy conservation law. Since the intensity of the pressure wave, in the spherical expansion assumption, decrease as r^{-2}, the amplitude of the acoustic signal decreases as r^{-1}. For cylindrical symmetry, in the near field approximation a $r^{-1/2}$-dependence of the pressure amplitude perpendicular to the cylinder axis is expected. In seawater the acoustic attenuation as a function of the frequencies is almost totally due to chemical absorption induced by the sound wave. In the range $1 \div 100$ kHz the absorption is dominated by the relaxation processes of the magnesium sulphate $MgSO_4$, at frequencies below 1 kHz the absorption is dominated by the ionic relaxation of the boric acid $B(OH)_3$. Relaxation frequencies for the boric acid f_B and the magnesium sulphate f_{Mg} have been calculated by Ainslie and McColm [75]:

$$f_B = 0.78\sqrt{\frac{S}{35}}e^{\frac{T}{26}}\mathrm{kHz}, \tag{3.7}$$

$$f_{Mg} = 42e^{\frac{T}{17}}\mathrm{kHz}. \tag{3.7}$$

where S is the salinity expressed in ppm and T the seawater temperature in degree Celsius.

The propagation medium acts as a signal filter causing frequency dependent attenuation. The amplitude of the acoustic signal at a distance r from the source, is attenuated by a factor:

$$\alpha(f) = e^{-k(f)}, \tag{3.7}$$

where $k(f)$ is the typical attenuation coefficient of the medium. In Fig. 3.7 the attenuation coefficient $k(f)$ for seawater at temperature of 14 °C, salinity of 35 ppm and a pH equal to 8.2 is reported.

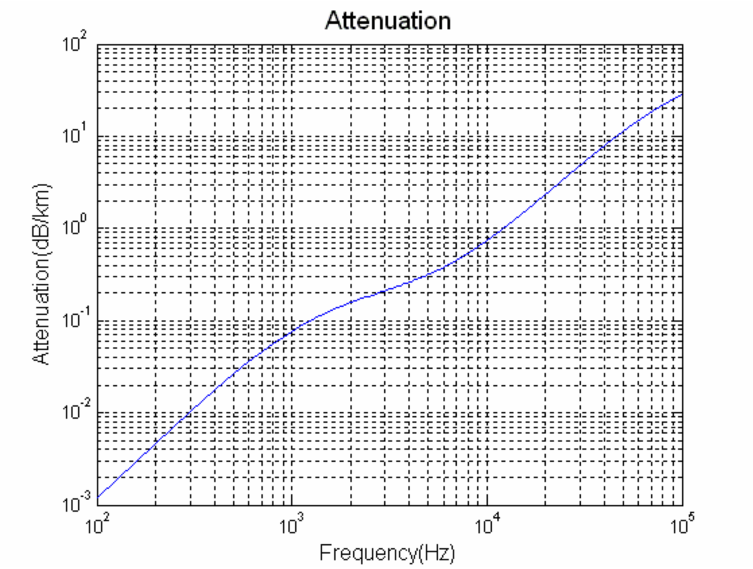

Figure 3.7: Attenuation coefficient in seawater as a function of the acoustic wave frequency in case of a temperature of 14 °C, a salinity of 35 ppm and a pH equal to 8.2

Since these attenuation coefficients depend on the frequencies of the acoustic wave, a change of the power spectral density of the signal is expected during the propagation in the medium, with a consequent distortion of the waveform. In Fig. 3.8 the acoustic signal shape at different distances from the source is shown.

In ice the sound propagation mechanisms are less well understood. Dominant attenuation mechanisms for frequency below a few hundred kHz are related to the absorption due to proton reorientation and to Rayleigh scattering due to bubbles and grains boundaries. Recent measurements show that ice, despite the Gruneissen coefficient is larger, suffer for a stronger sound absorption ($L_{sound} \approx 300$ m at about 400 m depth) compared to water [76].

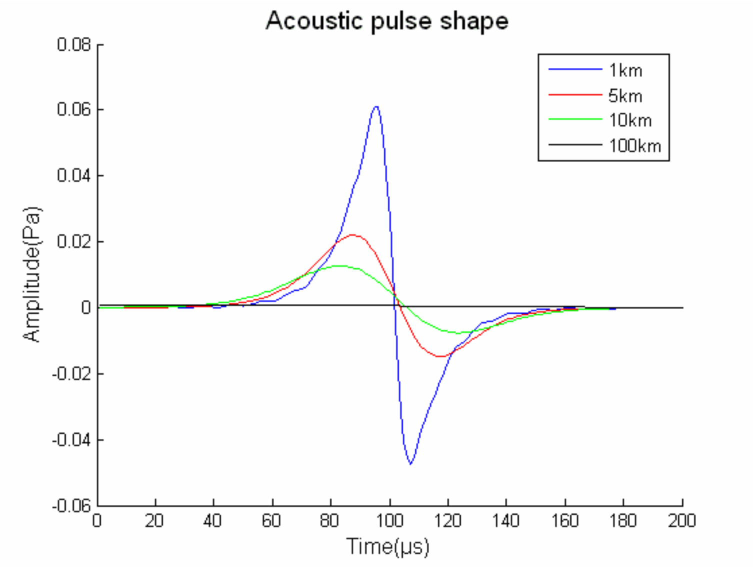

Figure 3.8: Expected acoustic signal shape as a function of the time at different distances from the sources. The change of the pulse shape is due to the frequency dependency of the attenuation coefficient [74].

3.5 Environmental acoustic noise

The energy threshold for neutrino acoustic detection is set by the ratio between ambient noise and signal amplitude. The environmental noise in seawater have been mapped out in detail by military and marine science researchers. Fig. 3.9 shows the typical sound level at different frequencies [77].

At frequencies lower than 1 kHz the noise is dominated by geosismic and shipping noise. Between 1 kHz and 50 kHz, the underwater acoustic noise is strongly dependent by the sea-state condition: the main contribution is due to wind and rain interactions with the sea surface. The power spectral density (PSD) of the acoustic noise in seawater is usually approximated by the Knudsen formula [78]:

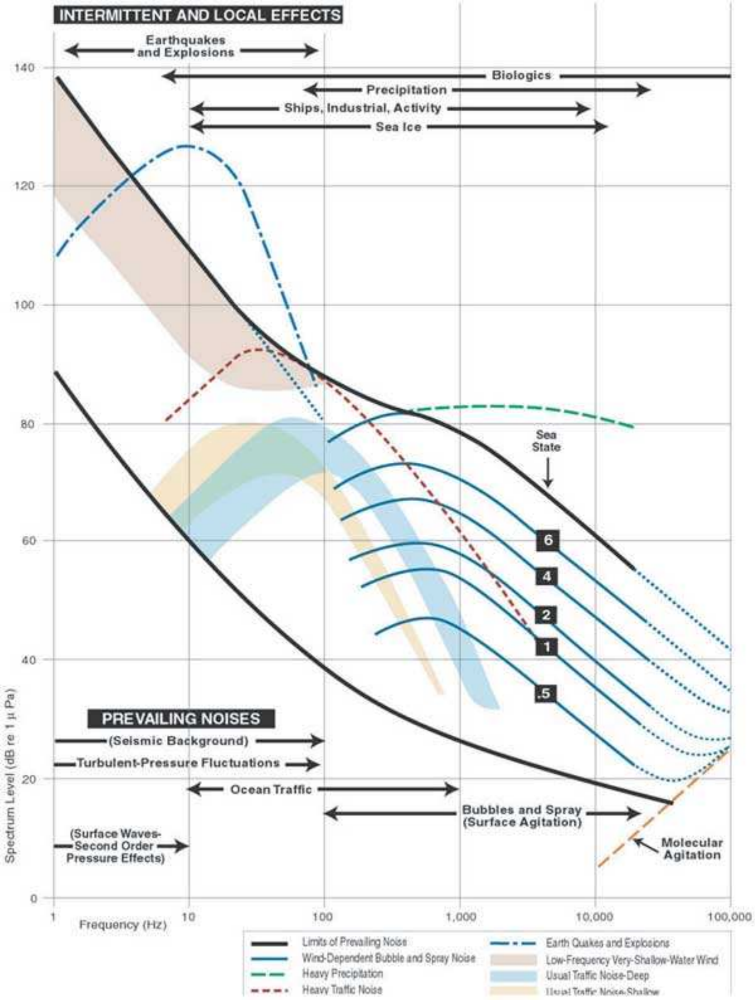

Figure 3.9: Power spectral density of underwater noise measured by Wenz in shallow water.

$$PSD(f_{Hz}, SS) = 94.5 - 10\ \log\ f^{5/3} + 30\ \log\ (SS + 1)\ \text{re}\ 1\ \mu\text{Pa}^2/\text{Hz} \tag{3.7}$$

where SS (Sea State) indicates the conditions of the sea-surface in a scale from 0 (calm sea) to 9. This approximation, however does not take into account transient signals, produced for examples by ship propeller cavitation, sonar and cetaceans. These sources are typically in the frequency range between 1 kHz and few tens of kHz, that is the same range of interest for neutrino acoustic detection. At frequency above 50 kHz, the main contribution to the noise spectrum is due to the thermal vibration of the water molecules, that is proportional to f^2. In the South Pole ice the acoustic noise is assumed to be low and stable because none of the sources mentioned above are expected to contribute. However there is still lack of measurements that do not permit to set firm limits on acoustic noise. Due to the depth dependence of the ice density, the first 200 m of firn ice acts as an acoustic filter, while anthropogenic and environmental noises entering the ice from the surface are refracted back.

3.6 Acoustic neutrino detection: pilot projects

In recent years several experimental groups have started R&D activities on acoustic detection. These groups had take advantage of installing hydrophones on military array or infrastructures of new underwater/ice Čerenkov telescopes. In the next sections the recent prototypes for a future acoustic neutrino detector will be described.

3.6.1 SPATS

The South Pole Acoustic Test Setup (SPATS) [79] consists of four vertical strings deployed in the upper 500 m ot the South Pole ice cap. In each string there are seven stages, each equipped with one transmitter and one sensor module, called *glaciophone*. The activity of the SPATS team has permitted for the first time the experimental measurement of sound attenuation length and the sound velocity in deep polar ice. A sound attenuation length of about 300 m has been measured, a value much less than expected from theoretical estimates. SPATS operates a detector for transient acoustic signals. Out of each hour, 45 minutes are used for triggered data taking while in the remaining 15 minutes environmental monitoring and system health data are recorded, including measurements of the noise floor. The absolute noise level integrated in the bandwidth 10÷50 kHz has been measured for all SPATS channels. The localization performances of the detector have been evaluated by measuring the sounds produced by the near drill operations carried out during the Ice-Cube strings installation. Fig. 3.10 shows a good agreement between reconstructed real and reconstructed simulated events below 170 m depth (localisation precision in the z coordinate of 25 cm). In the upper region of the SPATS array, the performances are largely influenced by the depth dependence of the sound speed in the medium.

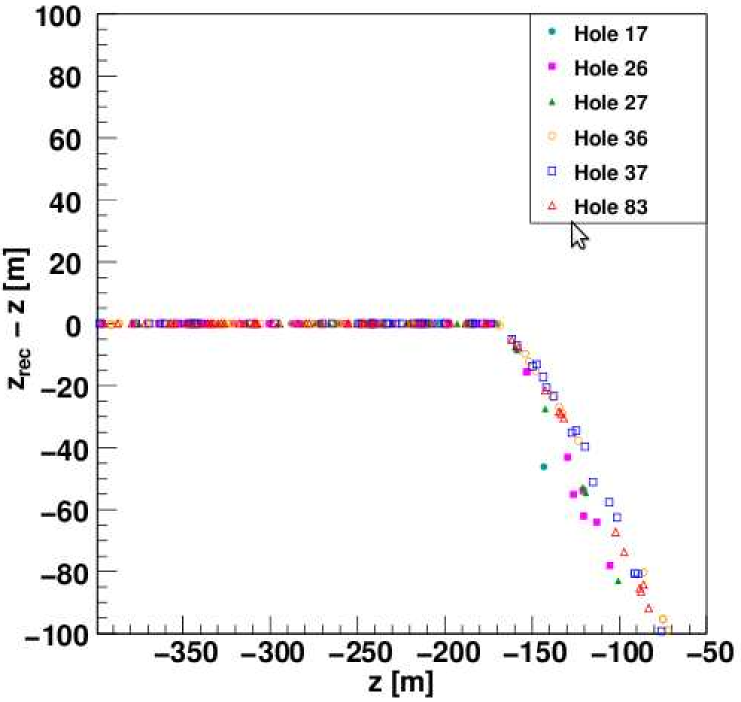

Figure 3.10: Difference beetwen reconstructed real and reconstructed simulated events from Ice-Cube holes drilled.

3.6.2 SAUND

The Study of Acoustic Ultra-high Energy Neutrino Detection (SAUND) Phase-II is the first experiment that read out a large array (about 1500 km^3) of hydrophones undersea for the purpose of detecting UHE neutrinos. SAUND Phase-II follows the first phase where about 15 km^3 were read out at the same site [80]. It employs a large hydrophone array at the US Navy's Atlantic Undersea Test and Evaluation Centre (AUTEC) located at the Tongue of the Ocean (TOTO) in the Bahamas Islands. SAUND II uses 49 of these hydrophones, installed on the sea-floor, transmitting signals to shore over optical fibres. The array spans an area of about 20 km x 50 km with spacing of $3 \div 5$ km, at depths between 1340 m and 1880 m (see Fig. 3.11).

With the SAUND array, an extensive study of the ambient noise has been performed and a hadronic shower parametrization useful for ultra-high energy neutrino detection has been developed.

3.6.3 AMADEUS

AMADEUS (ANTARES Modules for the Acoustic Detection Under the Sea) project aims at the investigation of techniques for acoustic neutrino detection in the deep sea [81]. The AMADEUS system is integrated into the ANTARES neutrino telescope in the form of *acoustic storeys* that are modified versions of standards ANTARES storeys, in which the Optical Modules are replaced by custom-designed acoustic sensors. The AMADEUS system comprises a total of six acoustic storeys, installed on two detection lines of ANTARES. In each storey six acoustic sensors were implemented, arranged at distances of roughly 1 m from each other. The system is operating continuously and automatically since December 2007 and has performed both diffuse and transient signal measurements. Ambient noise has bean measured in the frequency range $1 \div 50$ kHz and their correlation with weather condition has been performed. Transient

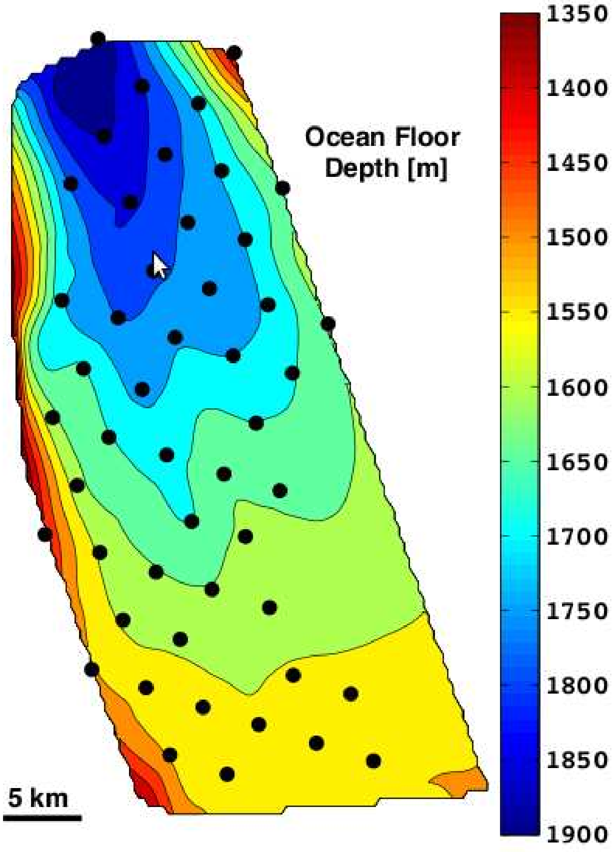

Figure 3.11: Layout of the SAUND II array. Hydrophone locations are marked by bullets. Colour shows the depth of the ocean floor.

acoustic signals are reconstructed with a resolution of about 3° in azimuth and 0.5° in the polar angle. In Fig. 3.12 the map of arrival direction of these acoustic sources is shown. The ANTARES long baseline acoustic beacons are identified as acoustic sources from below the sea surface

3.6.4 OνDE

First studies for acoustic neutrino detection has been conducted by the NEMO Collaboration in the Ionian Sea with the deployment of OνDE (Ocean Noise Detection Experiment). OνDE operated at the NEMO Test Site, 2000 m depth, 25 km off the coast of Sicily, from January 2005

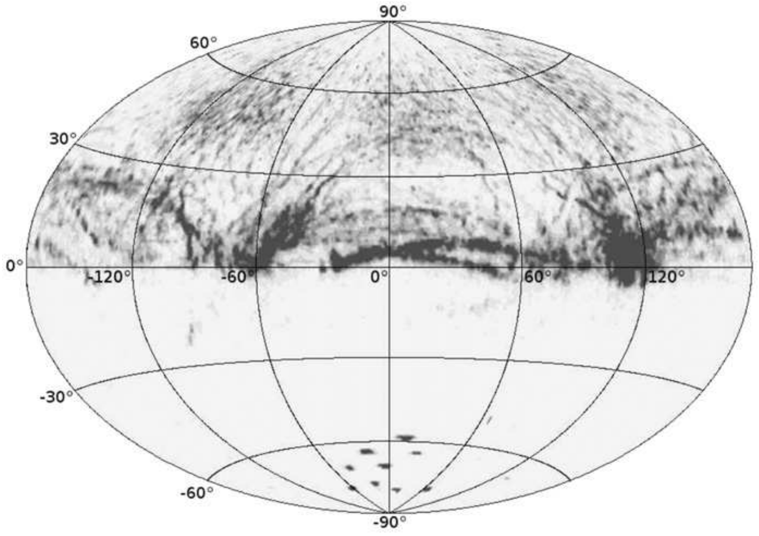

Figure 3.12: Map of the arrival directions of transient acoustic signals detected by the AMADEUS array. The majority of the signals due to naval traffic comes from above. In the lower hemisphere (under the horizon of an observer on the acoustic storey) the ANTARES acoustic position system can be identified.

to November 2006. OνDe hosted four large bandwidth hydrophones arranged on a pyramidal-shaped frame and low-cost electronics for data acquisition and transmission. Data (sampled at 96 kHz and with 24 bit resolution) were continuously transmitted in real-time from deep sea and recorder on shore. Acoustic noise was studied as a function of time, weather conditions, presence of ships and biological sources. The average sound pressure density of sea noise recorded from May 2005 to November 2006 is reported in Fig. 3.13. Dolphins and sperm whales sounds were detected almost daily; this has produced a great interest from the bioacoustic community since sperm whales were considered disappeared in that area [82].

3.6.5 NEMO-SMO

Based on the experience of OνDE, the NEMO Collaboration is working on the realization of an underwater acoustic array that will be in-

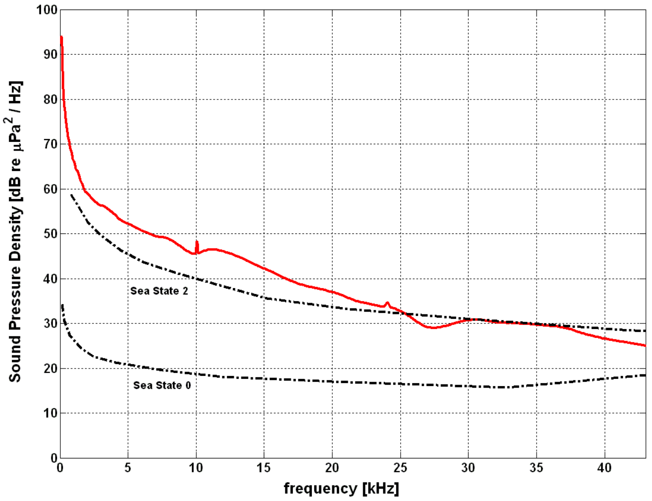

Figure 3.13: Average sound pressure density of sea noise recorded by OνDe from May 2005 to November 2006 (solid red line). The dotted black lines indicates respectively the expected SPD of the sea in conditions of Sea State 0 and Sea State 2

.

stalled in the Capo Passero Site, at a depth of 3500 m, by the first months of 2013. The array, called SMO (Submarine Multidisciplinary Observatory), will be installed on the KM3NeT tower prototype NEMO Phase-II. SMO will be able to work both as positioning system for the tower and acoustic detector, in coincidence with the optical detector. The NEMO phase-II tower prototype and the SMO project will be described in details in the Chapter 4 and Chapter 5 respectively.

Chapter 4

The NEMO Phase-II detector

Within the activities of the NEMO Collaboration and of the KM3NeT Consortium a new demonstrator for a deep-sea neutrino detector is going to be deployed at 3500 m water depth offshore Capo Passero, in Sicily. The detector, NEMO Phase-II, was designed and built taking advantage of the technological and scientific experience of the NEMO Phase-I experiment, that was deployed at a depth of 2000 m, 25 km off-shore Catania, in 2006. The deployment of Phase-II is foreseen by the first months of 2013 and the operation will continue for several years. Phase-II represents a fundamental step toward the construction of KM3NeT, being the first cabled detector deployed at such large depth, optimal to shield atmospheric muon background. It is a full-equipped prototype of a detection unit for the KM3NeT detector, that will be installed in Capo Passero Site. NEMO Phase-II will allow, indeed, the test and qualification of several key technological elements (mechanics, electronics, data transmission, power distribution, acoustic positioning and time calibration systems) proposed for the Mediterranean km^3 detector. The apparatus includes prototypes of the critical elements of a km^3 detector: a Junction Box (JB), the underwater electro-optical cable and a detection unit composed of 32 Optical Modules, hosting large area photomultipliers for the Čerenkov detection, and calibration systems. Moreover the NEMO Phase-II detector hosts the SMO (Submarine Multidisciplinary Observatory) acoustic array that will provide the underwater positioning of the detector and will allow multidisciplinary studies in deep-sea based on underwater sound detection. In this chapter the NEMO Phase-II detector will be described. The acoustic sensors and the positioning system will be discussed in Chapter 5.

4.1 The Capo Passero site and infrastructure

The Capo Passero Site (CPS, latitude 36° 25.010 N, longitude 15° 53.660 E, depth 3500 m), chosen for the NEMO Phase-II installation, shows optimal features to host an underwater Čerenkov detector: low optical background (80 kHz measured on 10” PMTs at 0.5 single photo electron threshold), blue light absorption length of 70 m (close to optically pure water), low currents (3 cm/s in average) and low sedimentation rate [83]. Moreover, the site is located in a wide abyssal plateau, it has very stable environmental conditions and a flat seabed morphology over several hundred km^2, allowing for future possible extension of the telescope (see Fig. 4.1).

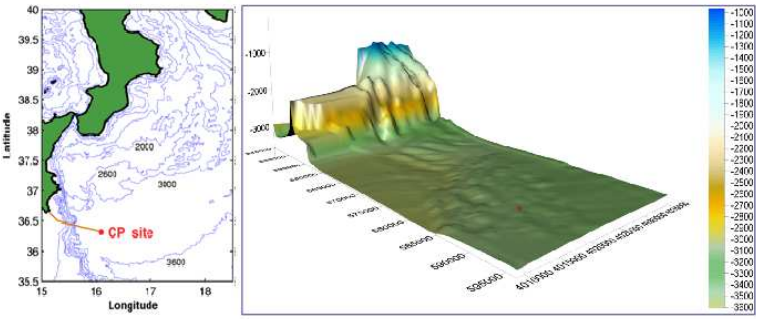

Figure 4.1: Map and bathymetric chart of the Capo Passero Site (CPS), where NEMO-SMO detector will be installed. The site lies at 3500 m water depth on a flat and wide plateau.

A dedicated shore laboratory, located in the harbour of Portopalo di Capo Passero, was built to host the necessary infrastructure and it is connected by means of a 96 km-long electro-optical cable to the underwater detector. The underwater cable is an umbilical underwater e.o. cable containing 20 optical single-mode fibres (standard ITU-T G-655) and 1 electrical copper conductor with sea return, suitable for medium voltage DC power transmission (10 kVDC) up to 80 kW. The underwater cable is presently terminated with a Junction Box (JB) deployed at CPS at the end of 2009. The JB, shown in Fig. 4.2, consists of a CTA (Cable Termination Assembly), an MVC (Medium Voltage Converter from 10 kVDC to 375 VDC), a hybrid electro-optical splitter and 3 ROV (Remotely Operated Vehicle) operable deep sea connectors (ODI Rolling Seal hybrid connector 5 ways - NRH series) [84].

The JB mechanical frame dimensions are about 2x1x1(h) m. Connector outputs provide 375 VDC power supply and multi-fibre optical link [84]. The cable and the JB are fed with 10 kVDC from shore by a PFE (Power Feeding Equipment). The JB then distributes 375 VDC power supply to the underwater detection unit. At present the available maximum power supplied by the JB is 10 kW, while the PFE can provide power supply up to 60 kW.

Figure 4.2: The Capo Passero deep-sea Junction Box, successfully deployed in November 2009. A detail showing the three ROV operable connectors is shown on the right.

A fundamental upgrade of the infrastructure has been accomplished at the end of 2011 with the installation of a dedicated optical fibre link between the Capo Passero shore lab and INFN-LNS. The link has been deployed and is operated by the Italian Consortium for Research Network, within the GARR-X project [85] and it is managed by INFN-LNS. INFN has also improved its capabilities to deploy and manage underwater experiments, owing a deep-sea light-class ROV with 2 manipulators (SeaEye Cougar, 4000-m operative depth, Fig. 4.3). The ROV has been acquired and built in the frame of the PEGASO project, funded by Regione Siciliana and coordinated by INFN and INGV (Istituto Nazionale di Geofisica e Vulcanologia, Italy).

Figure 4.3: Picture of the The PEGASO ROV. It will be employed in the installation of NEMO-SMO detector at a depth of 3500 m.

4.2 General architecture

The NEMO Phase-II detector consists of a vertical sequence of 8 horizontal aluminium structures 8 m long, called "floors", kept vertical by appropriate buoyancy on the top. The vertical distance between two adjacent floors is 40 m, a spacing of about 100 m is added between the lowermost floor and the base of the tower to allow for a sufficient volume of water below the detector (Fig. 4.5). Each floor hosts four optical modules: at each end of the floor two optical modules are installed, one downward looking and one horizontally looking. In addition to the 32 Optical Modules (OMs) the instrumentation installed on the tower includes several sensors for calibration and environmental monitoring. In particular two hydrophones are mounted on the tower base and at the ends of each floor. The hydrophones, together with an acoustic beacon placed on the tower base and other four beacons installed on the sea bed, are used for precise determination of the tower position by means of time delay measurements of acoustic signals (Acoustic Positioning System, APS). This hydrophones array, as mentioned, constitutes the SMO experiment, described in Chapter 6.

4.3 Mechanics and cabling

The mechanical lay-out of the NEMO Phase II detector concept is based on a semi-rigid vertical structure about 400 m high (the "tower") composed of a sequence of horizontal frames (hereafter floors) made of marine grade aluminium, mechanically interlinked by a system of ropes. During the deployment and handling operations on shore and aboard the ship, the floors of the tower are assembled together in a compact structure, to allow easy transportation and mooring (see Fig. 4.4).

The tower is anchored on the seabed by a dead weight. After the deployment of the detector in compact configuration, the buoy on the top of the structure is released and the towers reaches its operational configuration. Once unfurled, each floor assumes an orthogonal orientation with respect to its vertical neighbours, obtaining a three-dimensional displacement of PMTs, as shown in Fig. 4.5

The data acquisition and power distributions systems of the tower floors are hosted in pressure proof vessels (Floor Control Module, FCM) fitted in the middle of each floor. The vessel is a cylinder made of a marine aluminium alloy, to fulfil the requests of resistance to pressure and corrosion. The vessel is 95 cm long and its diameter is 17 cm. Inside the vessel, electronic boards are placed in a custom rack, as shown in Fig. 4.6.

The power distribution and the data transmission to and from the

Figure 4.4: The NEMO-SMO tower in compact configuration during the integration phase.

floors is fulfilled by the inter-floor “backbone” cabling system (see Fig. 4.7). The backbone is a lightweight umbilical subsea cable, produced by Nexans, made of 10 electrical conductors (5 screened pairs) used for the 375 DC power distribution and 12 optical fibres, placed inside a flexible steel tube, used for the data transmission. The backbone is splitted at the level of each floor by means of breakout boxes (BO). The breakouts are plastic vessels (High Density Polyethylene) filled with silicone oil and pressure compensated. Each breakout vessel is equipped with two hybrid penetrators, used to split the backbone, and with two connectors (1 electrical and 1 optical) to connect the backbone to the floor cabling system. In Fig. 4.8 a picture showing the breakout installed on the floor tower and its inner part is reported.

The connections of the FCM with the floor devices (typically 4 optical modules, 2 hydrophones and 1 oceanographic instrument) are performed by electrical connectors and cables, installed on the flange of the external aluminium vessel. In Fig. 4.9 a scheme of the floor cabling system is

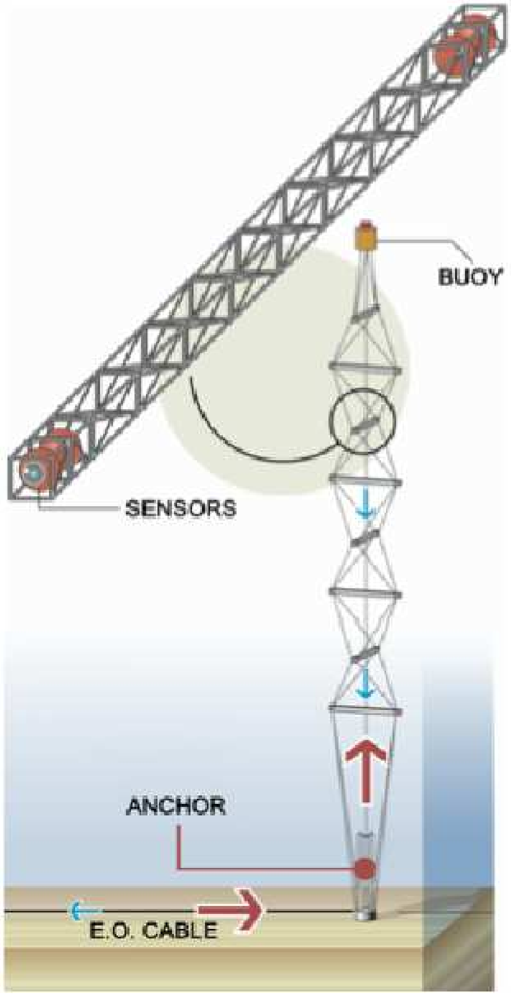

Figure 4.5: Sketch of the NEMO Phase-II tower: a buoy is located above the highest floor and pull the whole structures through a net of synthetic fibre ropes; the tower is anchored at the sea bottom.

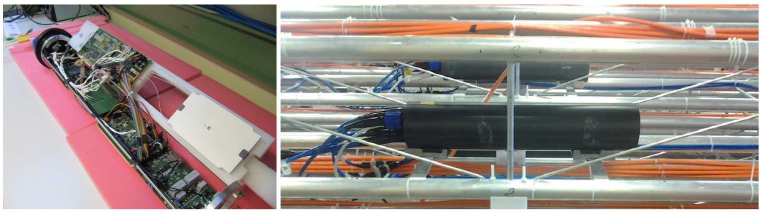

Figure 4.6: Left: The electronics boards of a NEMO-SMO floor fixed in the internal rack of the vessel. Right: The full integrated floor vessel.

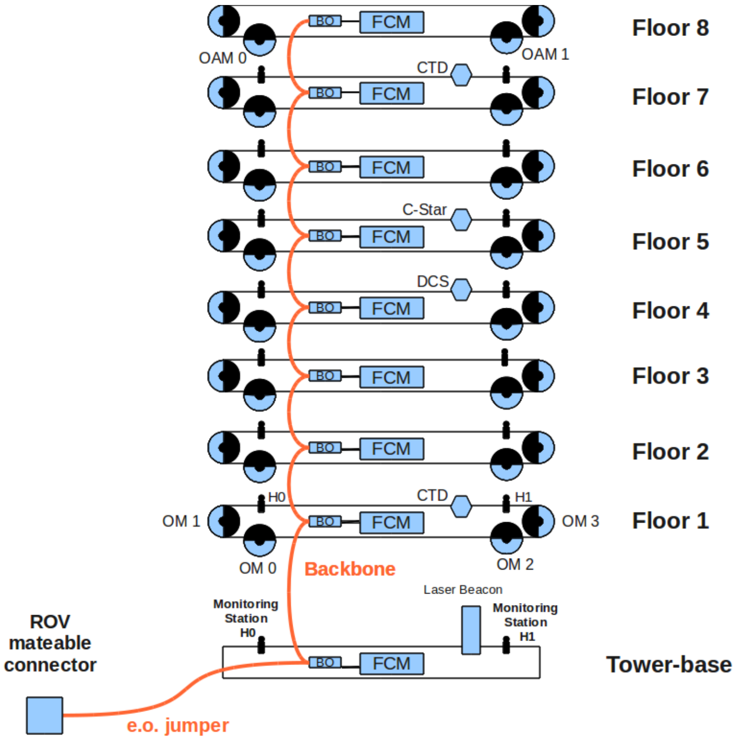

Figure 4.7: Schematic of the NEMO Phase-II, including the backbone cabling (orange), the Floor Control Modules (FCM) and the electro-optical breakouts (BO). Connection to the Junction Box is provided through a ROV-mateable hybrid connector the tower base

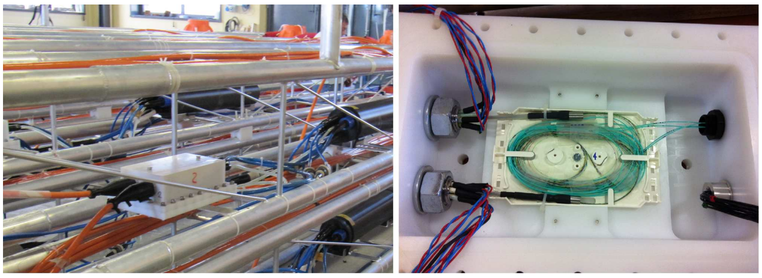

Figure 4.8: Left: picture of the breakout installed in the tower floor. Right: picture of the inner part of the breakout during integration. In order to resist to the underwater pressure the breakout vessel is filled with silicon oil.

shown.

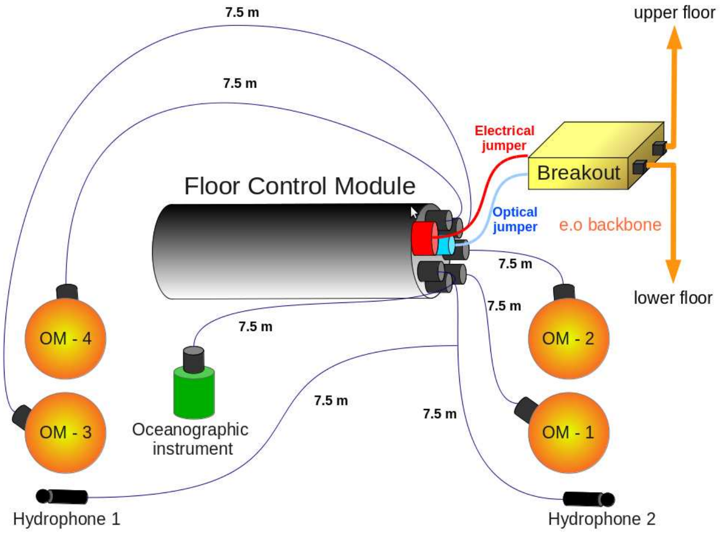

Figure 4.9: Scheme of the floor cabling system of the NEMO-SMO detector.

4.4 The Optical Module

Optical Modules (OMs) are the main detection systems of the Phase-II experiment. Each OM consists of a 13” high pressure resistant (up to 700 bar) borosilicate glass sphere (thickness $\sim$ 1 cm), containing a 10” Hamamatsu PMT R7081-SEL and its read-out and calibration electronics (Front-End Module, FEM Board,TimCal Board) as shown in Fig. 4.10. The Hamamatsu PMT R7081-SEL shows, together with a large photocatode area, a good time resolution of about 3 ns FWHM for single photoelectron pulses with an average charge resolution of $\sim$ 35%. Mechanical and optical contact between the PMT and the internal glass surface is ensured by an optical silicone gel. A μ-metal cage shields the PMT from the Earth’s magnetic field. The Front-End Module Board digitizes the analog signals produced by the PMT, encoding and transmitting these data in the defined communication protocol to a control board, installed in the Floor Control Module, called Floor Control Module Board (FCMB), described in the next section. The FEM samples the PMT signal using two 8-bit Fast Analog to Digital Converters (Fast-ADCs) running at 100 MHz staggered by 5 ns: this technique gives the desired sampling rate yet allowing a lower power dissipation than a single 200 MHz ADC. To match the [0÷ 5 V DC] input dynamic range of the PMT base to the 1.024 V input voltage range of the ADCs, the signal level is shifted and compressed by a non-linear circuit, which applies a quasi-logarithmic signal compression. The equivalent resolution obtained amounts to about 13 bits with a constant relative error. In operating condition, assuming an underwater background rate of 80 kHz from photo-electrons produced by ^{40}K decay, the data rate from each OM to shore will about 10 Mb/s.

Figure 4.10: Left: Semi-sphere of optical module holding the photomultiplier and the Front-End Module board. Right: Optical module fully integrated with connector and pressure meter.

4.5 Power supply and power control system

The power supply of the sensors installed on the NEMO Phase-II tower is provided by a dedicated board, called Control Power Supply (CPS)(Fig. 4.11), installed inside the FCM. The CPS distributes the power to the electronics boards of the floor. It is characterized by an input voltage of 375 VDC, output low voltages of 5 VDC and 12 VDC, a maximum power of 50 W and full load efficiency equal to 0.81. In this board are installed electronic breakers to switch on and off the low voltage required by the floor loads. Moreover, the CPS is equipped with a soft start system, input and output current filters, an opto-isolated high voltage sensor, low voltage and current sensors.

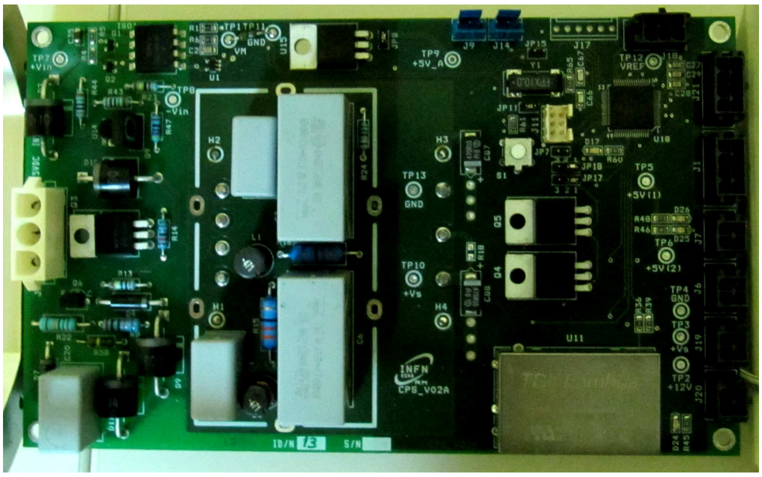

Figure 4.11: Picture of Control Power Supply (CPS) board. It distributes the power to the electronic boards of the floor.

The low voltage output lines of the boards are remotely enabled and disabled from shore by means of a dedicated control software. Moreover, the software allows to monitor the power consumption of each output lines through a graphical interface. A screen shot of the graphical interface is shown in Fig. 4.12.

4.6 Data acquisition and transport system

All data produced in each floor by the PMTs, the hydrophones and other devices used to monitor the apparatus status and the environmental conditions, are collected by the Floor Control Module Board (FCMB). The FCMB (see Fig. 4.13) represents the core of the detector data transmission system. The FCMB acts as a bridge between the different devices, each with specific physical and communication layer, and the data

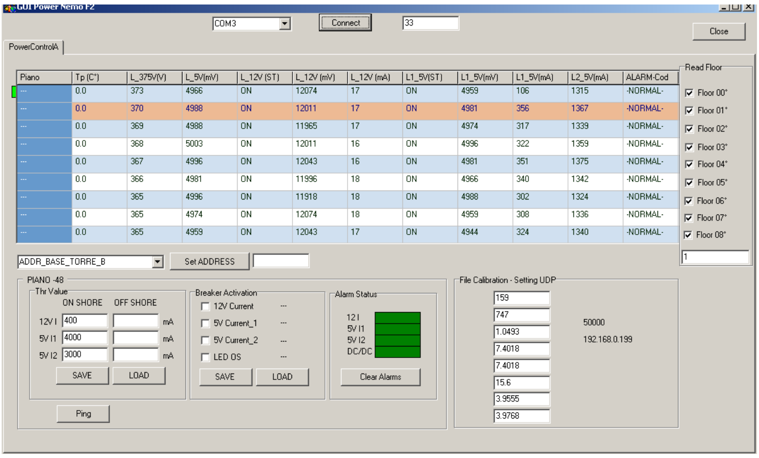

COM3

33

Piano	Tp (C°)	L_375V(V)	L_5V(mV)	L_12V (ST)	L_12V (mV)	L_12V (mA)	L1_5V(ST)	L1_5V(mV)	L1_5V(mA)	L2_5V(mA)	ALARM-Cod
---	0.0	373	4966	ON	12074	17	ON	4959	106	1315	-NORMAL-
---	0.0	370	4988	ON	12011	17	ON	4981	356	1367	-NORMAL-
---	0.0	369	4988	ON	11965	17	ON	4974	317	1339	-NORMAL-
---	0.0	368	5003	ON	12011	16	ON	4996	322	1359	-NORMAL-
---	0.0	367	4996	ON	12043	16	ON	4981	351	1375	-NORMAL-
---	0.0	366	4981	ON	11996	18	ON	4966	340	1342	-NORMAL-
---	0.0	365	4996	ON	11918	18	ON	4988	302	1324	-NORMAL-
---	0.0	365	4974	ON	12074	18	ON	4959	308	1336	-NORMAL-
---	0.0	365	4959	ON	12043	17	ON	4944	324	1340	-NORMAL-

☑ Floor 00°
☑ Floor 01°
☑ Floor 02°
☑ Floor 03°
☑ Floor 04°
☑ Floor 05°
☑ Floor 06°
☑ Floor 07°
☑ Floor 08°

1

ADDR_BASE_TORRE_B

	ON SHORE	OFF SHORE	
12V I	400		mA
5V I1	4000		mA
5V I2	3000		mA

☐ 12V Current ---
☐ 5V Current_1 ---
☐ 5V Current_2 ---
☐ LED OS ---

12 I 🟩
5V I1 🟩
5V I2 🟩
DC/DC 🟩

159
747
1.0493
7.4018
7.4018
15.6
3.9555
3.9768

50000
192.168.0.199

Figure 4.12: Screen shot of the graphical interfaces of the power control software. Voltage and power consumption of each power lines of all floors are reported.

transmission system to shore. The link to shore uses an optical fibre as physical layer and implements a high speed serial link using a proprietary data format. All data are encoded into a serial 800 Mb/s stream by a serializer, converted into optical signal by an electro-optical transceiver and transmitted to the shore station. In the communication protocol used by the NEMO Phase-II detector the data stream is divided in 125 μs long frames of 10000 bytes each. The bytes in the payload are labelled by their position in the frame. To each device a set of bytes in a programmable range is assigned.

Figure 4.13: Picture of the Floor Control Module Board (FCMB).

Detector data are received onshore by dedicated electronics, based on a Virtex 5 development board, that collects the information produced by the underwater electronics and make them available, through a Gigabit Ethernet connection, to the DAQ and storage systems. A picture of this board, called Ethernet Floor Control Module Board (eFCMB), is shown in Fig. 4.14

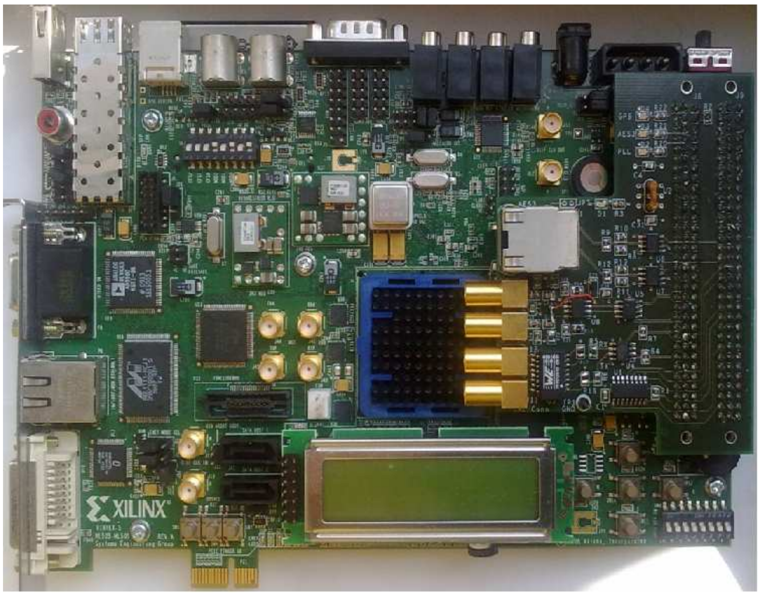

Figure 4.14: Ethernet Floor Control Module Board based on Virtex 5 board. The board receives and parses the underwater data stream, that can be accessed by the on-shore data acquisition system through Gigabit Ethernet connection.

For the NEMO Phase-II detector, a transmission system through optical links based on DWDM (Dense Wavelength Division Multiplexing) technology was chosen. It is implemented by means of "add & drop" passive devices which mux/demux many optical channels at different wavelengths into/from the same fibre, as sketched in Fig. 4.15. A specific wavelength is associated to each floor of the detector. The optical wavelengths are chosen in congruity with the ITU standard grid with 100 GHz frequency spacing in the C-Band thus allowing up to 45 channels per fibre. The DWDM network allows, indeed, a "point to point" communication between the shore-station equipment and the deep-sea apparatus; in such network each communication link shares the same physical medium without being affected by the neighbour links. In the NEMO Phase-II detector, each FCM contains an "add and drop" filter to add or subtract the specific optical wavelength dedicated to the floor. Data from all floors are thus transmitted through the backbone in the same fibre.

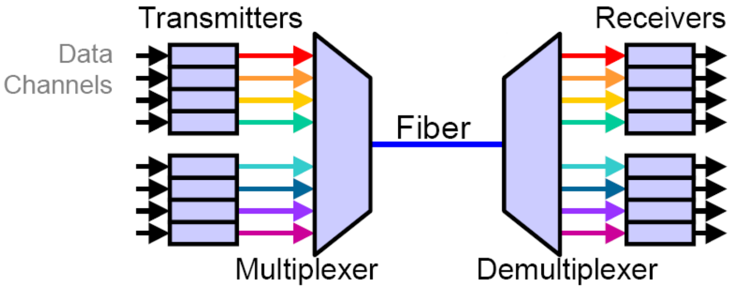

Figure 4.15: Schematic view of the DWDM data transmission technique. At each floor the detector is associated a wavelength. Data from each floor are transmitted from/to shore, embedded in the same fibre.

As shown by detector simulations, in order to reconstruct the track of the secondary muons generated in the neutrino interactions, each signal from OMs is labelled with an absolute time stamp. The required time resolution of the time stamping must be less than 1 ns to allow the muon track reconstruction with optimal angular resolution. This requests implies that read-out electronics of all sensors needs common timing and known latency with respect to a fixed time reference. The described constraint suggested to choose a synchronous protocol which embeds the detector clock and data on the same medium with low and fixed latency. The choice of a synchronous communication protocol allows both to simplify data transmission and to provide synchronization with a unique clock source. All FCMBs are, indeed, driven by the same detector Master Clock (40 MHz), derived from a GPS station on shore based on a Symmetricon XLi GPS receiver. A time alignment procedure must be implemented both to determine and to align the phases of the time stamps produced by different readout boards. In order to properly interpret the time measurements performed by the sensors of the tower, it is necessary to know the time offsets of each acquisition channel and their possible drifts with respect to the reference clock coming from the GPS station on-shore. The GPS receiver provides to the detector both the absolute GPS time, encoded in IRIG-B 100-1344 standard and used for the data time-stamping, and a 10 MHz rate output used as Master Clock. The accuracy of the emission of the Pulse Per Second (PPS) signal produced by the GPS receiver is better than 30 ns RMS with respect to Coordinated Universal Time (UTC). The time differences between the PPS, 10 MHz clock and IRIG-B time signal outputs produced by the GPS receiver and their stability were measured. Each output was connected to a digital oscilloscope. A run of 600 measurements was performed (Fig. 4.16). The measured time differences and their jitters are reported in Table 4.1.

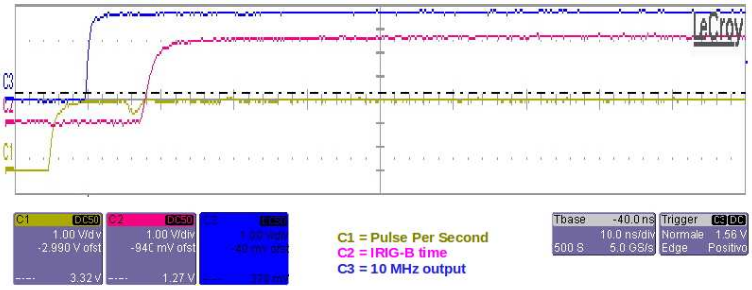

Figure 4.16: Time displacements between the PPS signal (yellow), the 10 MHz output signal (blue) and the IRIG-B time signal (pink) produced by the Symmetricon XLi GPS receiver, measured through a digital oscilloscope.

On-shore, a “timing station” is also implemented for time distribution, synchronization and calibration purposes. The “time station” distributes to the eFCMBs the 10 MHz reference clock, recovered from the GPS re-

	Mean value(ns)	Jitter (ps)
PPS - 10 MHz output time difference	5.21730	29.55
PPS - IRIG-B output time difference	12.89163	36.92

Table 4.1: Values of the time displacements between the PPS signal and 10 MHz output (used as detector Master Clock) and between PPS signal and IRIG-B output of the Symmetricon XLi GPS receiver.

ceiver. All the eFCMBs are synchronized by this clock and time-aligned by a command code, issued every 125 μs, to force the “start” of a communication frame. Each frame is identified with an identity code, which is the time counted in 125 μs unit. If the delay between the command and the start of a frame is constant, the data streams transmitted from shore are synchronous and time-aligned. In the off-shore part of the detector, the FCMBs will receive a synchronous data stream misaligned only because of the different path length of optical fibres, which vary from floor to floor. While the optical paths vary, from an electronic point of view the delay, equalization can be obtained using devices that exhibit a fixed latency in signal propagation. This requirement is more strict than the request of synchronism, because it implies a fixed phase relationship between each link from on-shore to off-shore read-out. The chip-set installed on the electronic boards of the NEMO Phase-II detector guarantees, by design, this fixed latency property.

4.7 The “echo” calibration

The time delay difference of each floor can be obtained by measuring the travel time of a frame sent by the eFCMB to go forth and back over the optical link to the correspondent FCMB on the tower. This delay is the sum of two contributions: the first contribution is related to the electronic latency of the FCMB/eFCMB pair, the second one to the optical path length. In order to evaluate this time delay, TTL signals in coincidence with the emission signal (EchoTx) and reception signal (EchoRx) of the data frames (each is 125 μs long) are recovered by means of two dedicated outputs, installed on the eFCMBs. The emission of the EchoTx signal is phased, by design, with the PPS emitted by the GPS receiver. The PPS-EchoTx time delay has been measured for each eFCMB of NEMO Phase-II using a TDC, model SRS RS620. The values of the measurements are reported in Table 4.2.

	PPS-EchoTX time delay (ns)
Tower Base 1	375.306494
Floor 1	375.302997
Floor 2	375.302997
Floor 3	375.301746
Floor 4	-
Floor 5	-
Floor 6	375.302006
Floor 7	375.302802
Floor 8	375.302006

Table 4.2: Time offset between the PPS signal, recovered from the GPS receiver, and the emission of the correspondent EchoTx signals from the eFCMs. Measurements related to floor 4 and floor 5 are missing because not available during these calibration.

During the detector integration, for each floor of the detector, the time delays with respect to the tower base have been measured setting up a test bench at the LNS. The contribution due to the electronic latency has been measured by using the test bench schematically shown in Fig. 4.17. It included the final FCMB/eFCMB pairs and two time-calibrated optical fibres, one fibre to transmit data from on-shore to off-shore electronics, the other one from off-shore to on-shore electronics. For each FCMB/eFCMB pair, the EchoTx-EchoRx time-distances have been measured by using a TDC, model SRS RS620. The reception time of the data frames on the off-shore electronics (EchoFloor signal, TTL standard) have been also measured, recovering a coincident TTL signal directly from the FCMBs. Table 4.3 reports the values of the EchoTx-EchoRx and EchoTx-EchoFloor time delays for each FCMB/eFCMB pair, after the subtraction of the contributions due to the calibrated fibres.

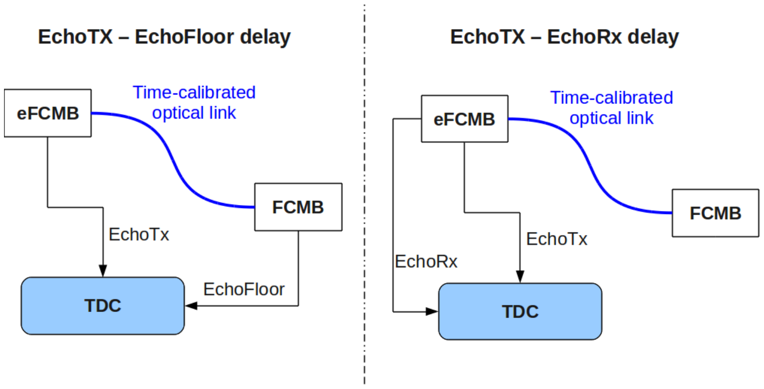

Figure 4.17: Sketch of the setup used to measure the contributions due to the electronic latency on the EchoTx-EchoFloor (left) and EchoTx-EchoRx (right) measurements.

	EchoTx-EchoRx el.delay (ns)	EchoTx-EchoFloor el.delay(ns)
Tower Base 1	969.557	260.946
Floor 1	968.899	261.390
Floor 2	969.372	259.974
Floor 3	969.317	258.257
Floor 4	973.924	263.792
Floor 5	971.094	263.913
Floor 6	968.919	261.067
Floor 7	969.217	259.854
Floor 8	965.717	259.319

Table 4.3: Time delay due to the electronic latency on the EchoTx-EchoFloor and EchoTx-EchoRx measurements for each FCMB/eFCMB couple of the NEMO Phase-II detector.

Since the EchoTx-EchoFloor time-distances can be measured only before the closure of the floor vessels and their installation on board the tower, the EchoTx-EchoFloor time-distances in the final configuration have been calculated by comparing the EchoTx-EchoRx measurements performed on the fully integrated detector with the values of EchoTx-EchoRx and EchoTx-EchoFloor measurements previously described. The measurements performed on the fully integrated detector take into account the time-delay introduced by the inter-floor backbone and the whole optical mux/demux system. The only difference with respect to the operational conditions, is that the main electro-optical cable is not present and it is replaced by a 60 m long test optical link, as shown in Fig. 4.18. The time delay of the data frame arrival to the floors with respect to the tower base is independent from the path length between the on-shore mux/demux system and the underwater ROV-operable connector of the detector. The time delays of each floor with respect to the tower base are reported in Table 4.4. The jitter of the measurements is less than 100 ps.

	Time delay wrt Tower Base (μs)
Floor 1	0.489558
Floor 2	0.775995
Floor 3	1.061151
Floor 4	1.355567
Floor 5	1.642511
Floor 6	1.923448
Floor 7	2.204022
Floor 8	2.498966

Table 4.4: Time delay of the data acquisition chain of each floor with respect to the tower base.

4.8 Optical Modules time calibration system

In addition to the "echo" calibration, that measures the Master Clock distribution delay through the backbone to the FCMs, another calibra-

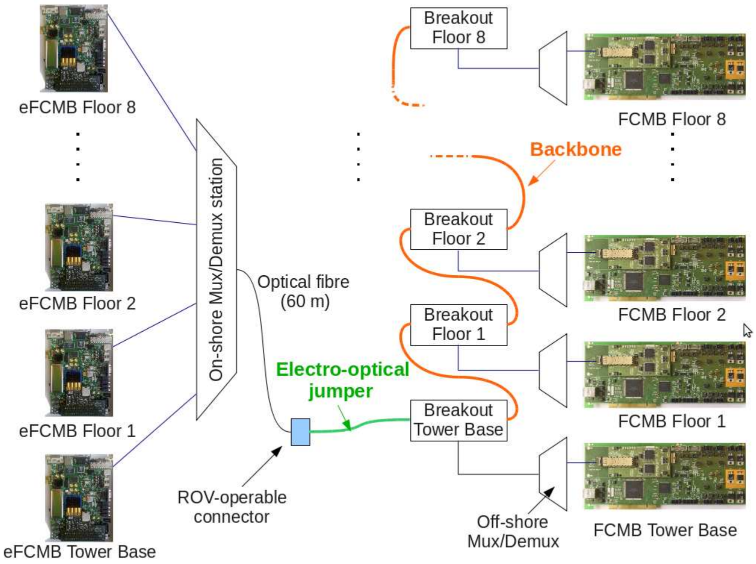

Figure 4.18: Sketch of optical transmission system used for the "echo" timing measurement .

tion procedure is needed to characterized the time offset introduced by each OM. Indeed, the analogue signals from each PMT, sampled at fixed rate of 200 MHz, are time stamped by means of a 16-bit counter incremented at 100 MHz rate, installed on the FEM. In order to evaluate the hit time of a photon on the photocathode from the time-stamping of the PMT pulses, different contribution must be taken into account: the length of cables connecting OMs and FCMBs, the FEM characteristics and the PMT transit time (that depends on the operating conditions and may change with PMT ageing). These offsets are measured during detector integration and during detector operation by means optical pulsers mounted on dedicated boards, called TimCals, installed in each OM. In order to propagate the electrical pulse signal with a known delay from the FCMB to the TimCals, a control board, called TimCtrl, is installed inside the FCM vessel (see Fig. 4.19). This board, based on Cyclone III FPGA by Altera, is capable of measuring the communication delays for the different pulsers, performing TDC measurements of the echo signals generated from the TimCals. The layout of the calibration system for a single floor is shown in Fig. 4.20. The same system is also used to illuminate OMs of different floors, allowing to inter-calibrate the local time of different FCMB. Since each photomultiplier is served by its own pulser, a high confidence in the long-term stability of these boards is mandatory. For this reason, the pulsers have been extensively tested looking for possible ageing effects. All tests performed so far give encouraging results on the feasibility of the system. The achieved time resolution of the readout is ~ 1 ns.

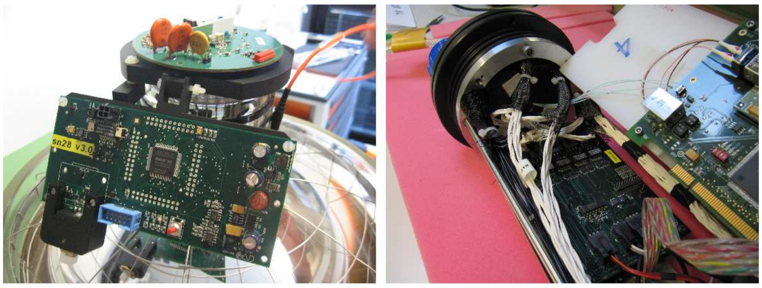

Figure 4.19: Left: TimCal Board installed in the OM. Right: Picture of the TimCtrl board into the FCM

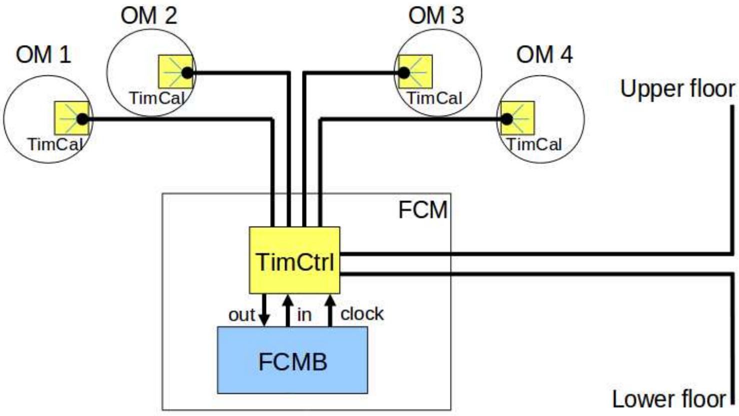

Figure 4.20: Layout of the time calibration system of a floor.

To ensure redundancy in the time calibration and measurement of the water optical parameters, a decoupled system based on optical devices, LEDs and lasers, is installed in the detector. The system determines the time offsets among optical modules by means of a LED pulser, the Nanobeacon, mounted inside selected OMs, close to the PMT and capable of illuminating the photocathode. The Nanobeacon comprises a blue LED mounted in a dedicated mechanical structure inside the OM and pointing upwards to illuminate the upper floors. Geometrical considerations show that a 15° opening angle is sufficient to illuminate OMs in the upper floor including allowance for potential misalignments smaller than 10° (see Fig. 4.21). The LED intensity is remotely controlled by means a control board installed in the OM. This circuit offers a very short rise time (≤ 2 ns). In Fig. 4.22 the pictures of a Nanobeacon and its control board are shown.

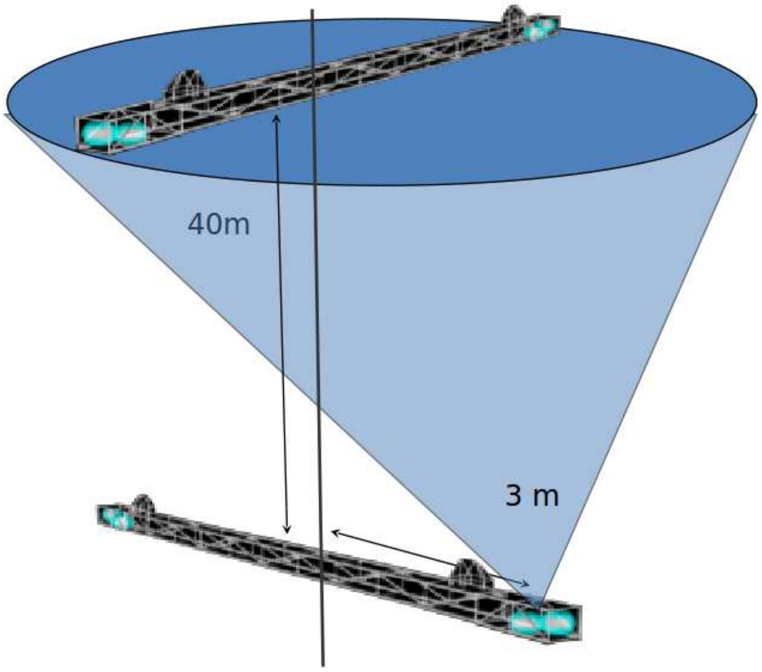

Figure 4.21: Operating scheme of the Nanobeacon system. A 15° opening angle is sufficient to illuminate OMs above the beacon even in perpendicular arrangement including potential misalignment .

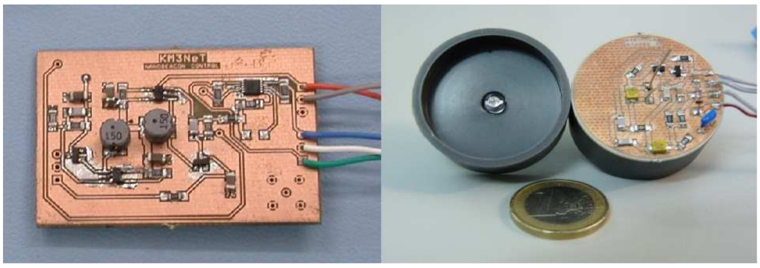

Figure 4.22: Left: Control Board of the Nanobeacon that is installed inside the OM. Right: mechanical structure supporting the LED of the Nanobeacon and its electronics.

In view of the km^3-scale telescope, the NEMO Phase-II detector hosts also a Laser Beacon that is installed at the base of the tower. The Laser Beacon has been designed to stimulate the first floors of adjacent detection units and determine possible time offsets among different detection units. The same system is capable to illuminate the whole tower, giving an independent check of the detector time calibration. The Laser Beacon optical source is a STG-03E-1S0 from Teemphotonics [86], which produces very short light pulses, below 400 ps (FWHM), of high intensity ($\sim 3.5\ \mu$J) and at a wavelength of 532 nm. The light intensity emitted by the laser can be varied using a voltage controlled optical attenuator, a linear polariser followed by a liquid-crystal retarder and a second linear polariser. The polarization of output light can be changed through variation of the voltage applied to the retarder, varying the transmission of the attenuator. The Laser Beacon, shown in Fig. 4.23 is housed in a titanium container and fixed at the tower base. The system can be also used to monitor the influence of the water characteristics on the photons propagation.

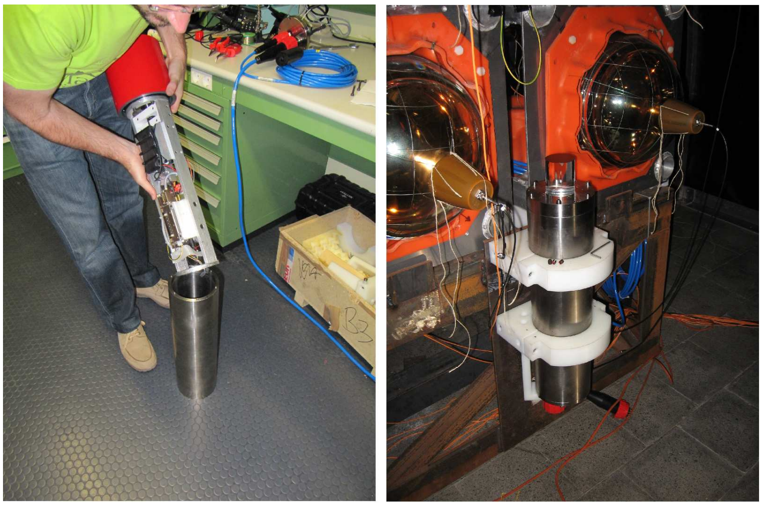

Figure 4.23: Pictures of the Laser Beacon during integration. The internal electronics is clearly visible (left); the laserbeacon fully integrated with the titanium external vessel installed in the tower base (right).

4.9 Environmental instrumentation

Monitoring of oceanographic and optical properties of deep seawater during the detection operation is also important since they can have an impact on the detector performances. For this reason several environmental probes are installed on the NEMO Phase-II tower: two Conductivity-Temperature-Depth (CTD) gauges used for the monitoring of the water temperature and salinity; a light transmissometre used for the measurement of blue light attenuation in seawater; a Doppler Current Sensor (DCS) used to monitor deep sea currents. Fig. 4.24 shows the positions of the environmental instruments on the tower.

Data from oceanographic instruments are managed by a dedicated board, called Slow Control Interface (SCI), installed in the each Floor Control Module.

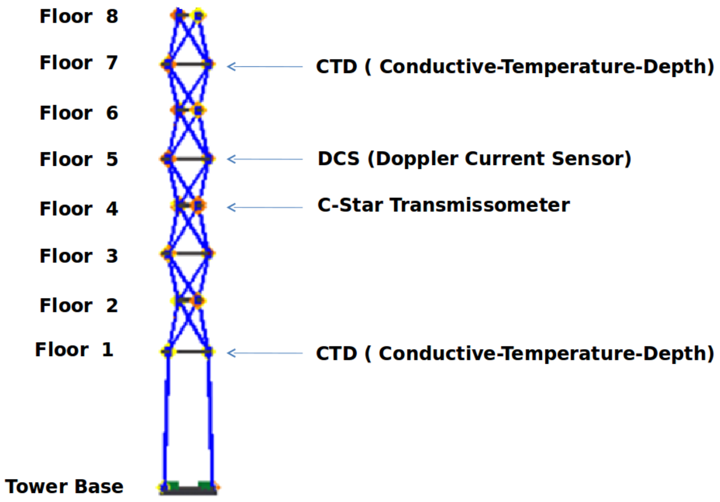

Figure 4.24: Geometrical disposition of the environmental instruments on the NEMO Phase-II tower.

4.9.1 Slow Control Interface

The Slow Control Interface (SCI), shown in Fig. 4.25 is an electronic board designed to interface the RS-232 serial data provided by commercial oceanographic instruments installed on the floor with the main data acquisition and transmission system of the detector. The SCI also distributes the power supply to the instruments by means of optically insulated breakers and it monitors the communication line status and the line power consumption. Each SCI module has, also, two analogue sensors to monitor the humidity and the temperature inside the FCM vessel. SCI exchanges data with the FCMB through a Serial Peripheral Interface (SPI), allowing 8 bits of data to be synchronously transmitted and received simultaneously. The software and the communication protocol of the SCI provides a point-to-point-like serial asynchronous link between off-shore instrumentation and on-shore laboratory.

Figure 4.25: Picture of the Slow Control Interface (SCI). The SCI is interfaced with environmental instrumentation using serial ports (RS-232).

4.9.2 CTD

CTD (Conductivity-Temperature-Depth) probes are installed on the 1^{st} and 7^{th} floors of the tower. The used CTDs is the 37-SM Micro-CAT CTD manufactured by Sea Bird Electronics [87](see Fig. 4.26), that allows high-accuracy measurement of water temperature, salinity and pressure. Each CTD requires a 12 VDC power supply, provided by the SCI, and it communicates through standard RS-232 serial interface with the SCI board. Temperature, salinity and pressure are relevant parameters that characterize sea-water properties, that can be correlated to underwater current. The CTD fulfils also another task, i.e. the indirect measurement of the sound velocity in the site derived by the Mackenzie algorithm [88], a critical parameter for the acoustic positioning system. Moreover, CTDs provide and independent measurement of the tower height.

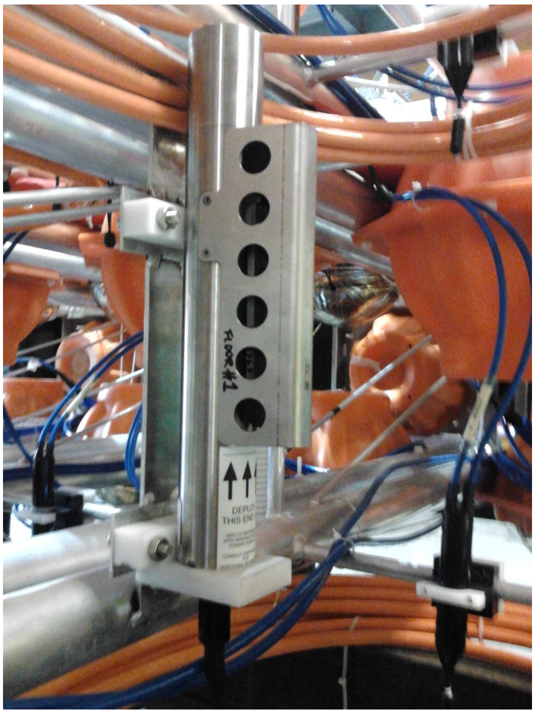

Figure 4.26: The 37-SM MicroCAT CTD (manufactured by Sea Bird Electronics) installed on the 1^{st} and 7^{th} floor of the tower

.

4.9.3 Digital C-star transmissometre

The C-Star light transmissometre is mounted on the 4^{th} floor of the tower in order to measure light transmittance in seawater. The C-Star manufactured by Wetlabs measures light transmittance at a specific wavelength over a known path [89]. The instrument installed on the Phase-II Tower is configured to have a path length of 25 cm and a wavelength of 470 nm. The C-Star requires a power supply of 12 V, provided by the SCI board. The measurement of light transmittance in situ is a fundamental input parameter in simulations of the detector response. The C-Star provides also hints on the presence of organic and inorganic particles dissolved in seawater. A picture of the Wetlabs C-Star is shown in Fig. 4.27.

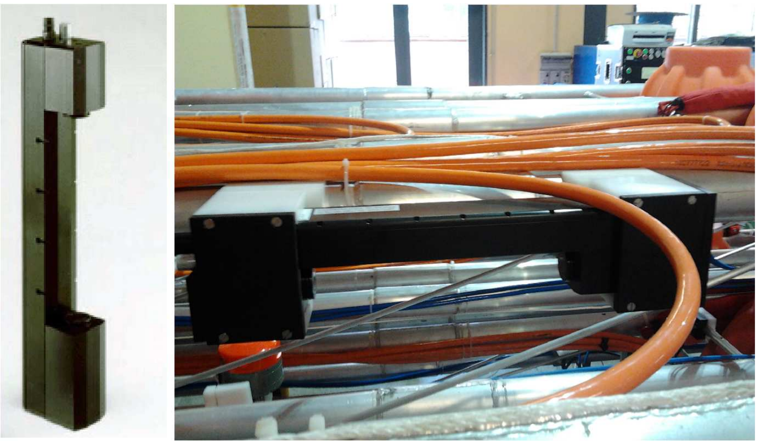

Figure 4.27: The Wetlabs C-Star (470 nm) installed on the 4th floor of the NEMO Phase-II tower.

.

4.9.4 Doppler Current Sensors

In order to monitor underwater sea currents along the full height of the tower, a Doppler Current Sensor (DCS) Anderaa 3820 R [90] is installed on the 5th floor of the Tower (Fig. 4.28). The DCS performs current measurements based on the backscatter acoustic Doppler principle. Four transducers transmit short pulses (pings) of acoustic energy along narrow beams. The same transducers receive backscattered signals from scatterers (normally plankton, gas bubbles, organisms) that are present in the beams (from 0.4 m to 1.8 m from the sensor), which are used for calculation of the current speed and direction. Thanks to internal compass circuit the sensor is able to determine the current speed and direction. The DCS chosen for NEMO Phase-II has a range of 0 to 300 cm/s and accuracy of 0.15 cm/s with a nominal standard deviation of 0.45 cm/s.

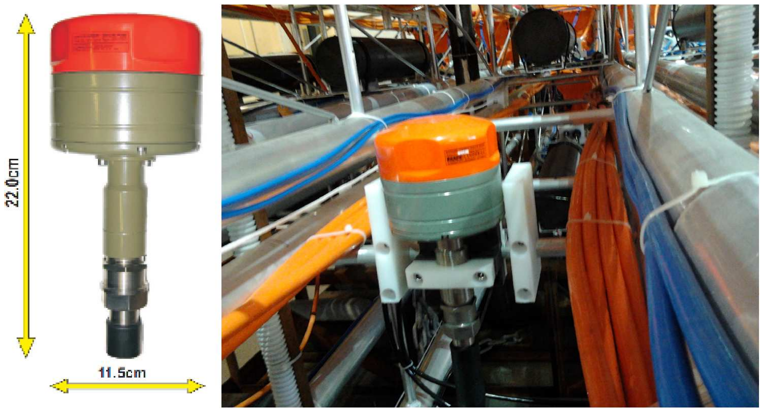

Figure 4.28: The Doppler Current Sensor 3820 R (manufactured by RD Anderaa) mounted on $5^{th} floor$

.

4.9.5 Attitude Heading Reference System board

The real time monitoring of yaw, pitch and roll of each floor is provided by an Attitude Heading Reference System (AHRS) board, developed by INFN, placed inside each FCM vessel (Fig. 4.29). It consists of MEMS gyroscopes, accelerometers and magnetometers on all three axes. The yaw, pitch and roll are calculated by means of a 9^{th} order extended Kalman filter with a dynamic angular resolution of 0.01°. The output maximum rate is 130 Hz. These measurements, together with acoustic positioning performed by the SMO array, permit to estimate the tower position with the desired accuracy of ≤ 10 cm.

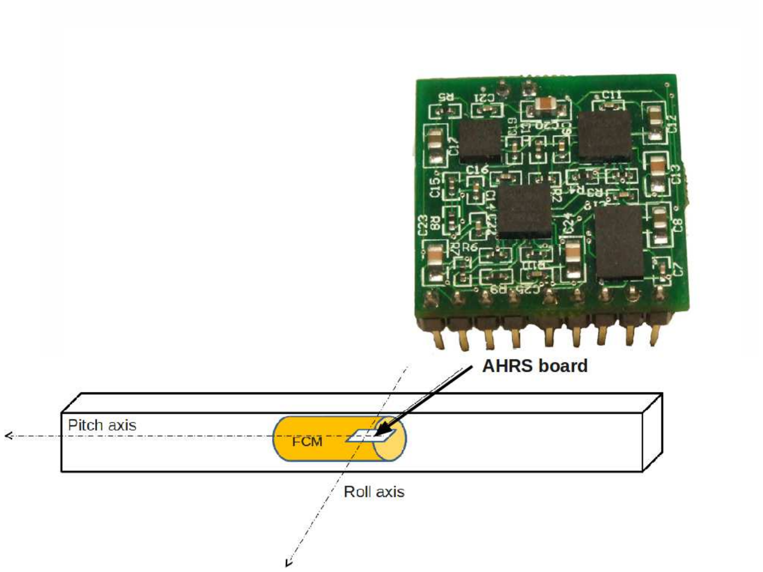

Figure 4.29: Picture of the Attitude Heading Reference System (AHRS) board installed in the FCM vessel. The position of the board inside the FCM vessel with respect to the floor direction is shown

.

Chapter 5

The NEMO-SMO project

The SMO (Submarine Multidisciplinary Observatory) [91] project aims at performing multidisciplinary studies in deep-sea based on acoustic detection. SMO is a 3D array of 14 broad-band (10 Hz ÷ 70 kHz) acoustic sensors installed on board of the NEMO Phase-II detector. The sensors are installed on both ends of each floor and on the base of the detector (monitoring station), to compose an acoustic array about 400 m height. The SMO data acquisition system is fully integrated on the detector electronics. For NEMO's sake, the SMO array will provide the acoustic positioning of the tower, detecting acoustic signals produced by a long baseline of acoustic beacons anchored on the sea-floor. The main purpose of the SMO Collaboration activity is addressed to detection of bio-acoustic sounds (marine mammals), acoustic environmental monitoring, tests of novel tsunami detection technique and studies on acoustic neutrino detection. For SMO a novel technology for underwater GPS time-stamp of acoustic data was implemented and tested. Thanks to the employment on an "all data to shore" philosophy, all acoustic data from deep-sea will be available at the shore station in real-time.

5.1 The acoustic sensors

One of the main tasks of NEMO-SMO was addressed to the selection and characterization of hydrophones suitable for very deep sea installation. Most of commercially available hydrophones, in fact, are not rated for long term deployment at 350 bar pressure (3500 m depth water equivalent), and their calibration curve as a function of depth is not known. For this reason a new hydrophone, the SMID TR-401 (Fig. 5.1), has been developed for INFN by the SMID company [92].

A set of 40 hydrophones and preamplifiers has been acquired, tested and certified at the NATO Undersea Research Centre [93] of La Spezia (Italy). For each hydrophone the receiving sensitivity has been measured between 5 kHz and 70 kHz. The calibration curves of all hydrophones,

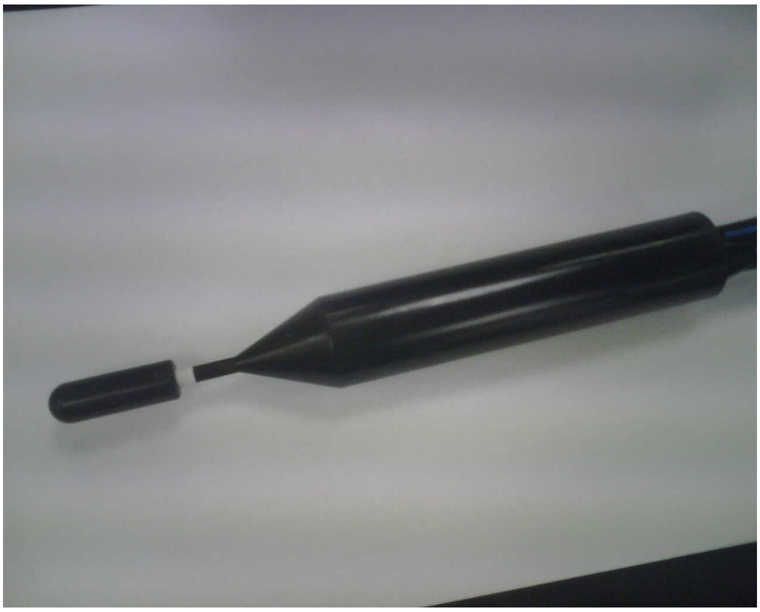

Figure 5.1: Picture of the SMID TR-401 hydrophone and SMID AM-401(V)1 preamplifier.

measured at 1 bar pressure, are shown in Fig. 5.2. The curves are obtained coupling the hydrophones with a SMID AM-401(V)1 preamplifier, having gain of +38 dB. The hydrophone-preamplifier system features an overall sensitivity of -172±3 dB re 1 V/μPa, flat in a large frequency range (10 Hz ÷ 70 kHz), as shown in Fig. 5.2. Fig. 5.3 shows, for the 40 acquired hydrophones, the relative change of sensitivity as a function of pressure, measured using a 20 kHz calibration signal, at a pressure of 50, 300 and 400 bars (500 m, 3000 m and 4000 m water equivalent). The change of sensitivity, as a function of pressure, is less than ± 1 dB and it is therefore negligible in typical acoustic apparatus. Horizontal beam-patterns at 30 and 50 kHz were measured with 20° angular resolution; the directivity pattern of the hydrophone is omnidirectional.

The selected SMID hydrophones are installed in the tower base and in the first 6 floors of the NEMO Phase-II detector. The SMID hydrophones installed on the floors 1÷6 are coupled with SMID AM-401(V)1 pream-

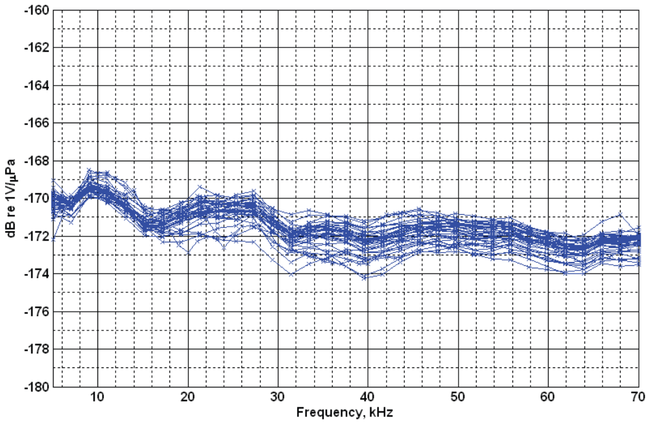

Figure 5.2: Sensitivity curves for 40 SMID TR-401 hydrophones as a function of frequency (at 1 bar pressure).

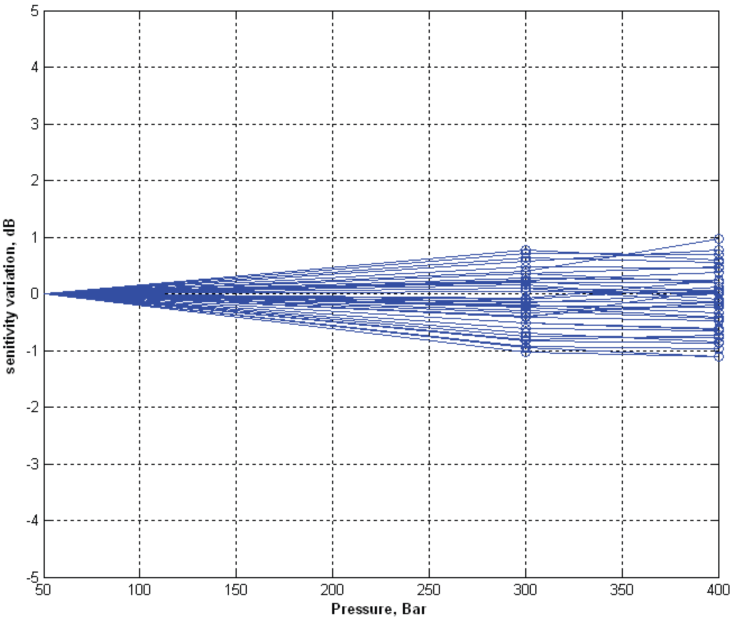

Figure 5.3: Relative change of sensitivity for 40 SMID TR-401 hydrophones between 50 bar and 400 bar (at 20 kHz).

plifiers, having a a gain of +38 dB. In the tower base, in order to avoid possible overload on the data acquisition system due to the proximity (about 2 m) of the hydrophones to one of the acoustic beacons used for the positioning of the detector, lower gain (+20 dB) preamplifier is employed, model SMID AM-401(V)2. For both models the equivalent input noise is about 1 nV/$\sqrt{Hz}$. The electrical properties of the SMID AM-401(V)1 preamplifier are reported in Table 5.1. Hydrophone and preamplifiers are cabled and moulded in a 7.5 m long deep-sea cable connected to the FCM.

Gain	38 dB (32 dB single-ended)
Z_{IN}	100MΩ/40pF
Z_{OUT}	50Ω
I_{OUT}	30mA
Frequency range	4Hz÷150kHz
Equivalent input noise	1 nV/$\sqrt{Hz}$ (f=25kHz, C=2nF)
Distorsion	1 % (V_{IN}=20mV)
V_{IN-MAX}	50mVptp
$V_{OUT-MAX}$	1.7 V_{RMS}
V_{ALIM}	4÷6 V (80mA)

Table 5.1: Electrical properties of the SMID AM-401(V)1 preamplifier. The SMID AM-401 (V)2 preamplifier differs only for the different gain, +20 dB instead of +38 dB.

In the 7^{th} floor of the tower, 2 free flooded rings (FFR) hydrophones manufactured by Sensor Technology Ltd, model SX-30 (see Fig. 5.4) [94] and provided by UPV [95] in collaboration with CPPM-CNRS [96] are installed. The performances of these FFR hydrophones have been evaluated by UPV. Their sensitivity is about -193 dB re 1 V/μPa in the range 20 kHz ÷ 40 kHz, as shown in Fig. 5.5 . Tests performed at INFN-LNS have demonstrated the full compatibility of the sensors with the SMID AM-401(V)1 preamplifier.

In the 8^{th} floor, 2 custom piezo-sensors developed by Erlangen Centre for Astroparticle Physics (ECAP) [97] are installed in a special Opto-Acoustic Module, built by INFN. The piezo-sensors are glued in the internal part of the NEMO Phase II optical module, in contact with

Figure 5.4: Free flooded rings hydrophones Sensor Technology Ltd SX-30 + SMID AM-401(V)1 premplifiers, moulded in a deep-sea cable 7.5 m long.

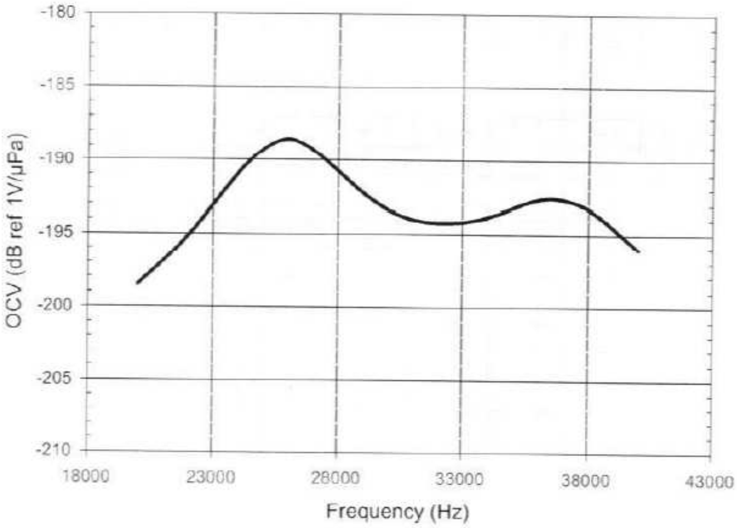

Figure 5.5: Receiving Voltage Response of the Sensor Technology Ltd SX-30 FFR hydrophone measured at a depth 0.6 meters and a temperature of 20 °C.

the glass. Acoustic signals are detected through the glass oscillation. NEMO-SMO will test for the first time the performances of the OAMs, suggested as cost-effective solution for the acoustic positioning system of KM3NeT [57].

In Fig. 5.6 a piezo-sensor and its respective preamplifier board inside the Opto-Acoustic Module are shown.

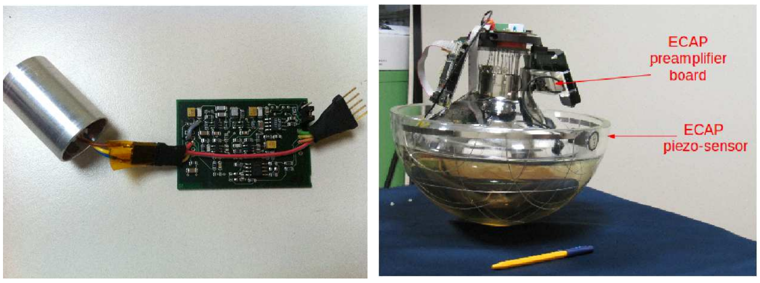

Figure 5.6: Left: picture of the ECAP piezo-sensor and preamplifier board. Rigth: piezo-sensor and preamplifier board integrated in an Opto-Acoustic Module.

5.2 Off-shore acquisition electronics

The data acquisition system of the SMO acoustic array is fully integrated with the NEMO Phase II detector one. The analysis of the acoustic signals is entirely performed on-shore, i.e. the acquisition system is based on an “all data to shore” philosophy. All acoustic signals acquired by the acoustic sensors are sampled underwater and continuously sent to shore through the NEMO Phase-II data transmission system. A schematic view of the data acquisition system for a single floor of the NEMO-SMO detector is shown in Fig. 5.7.

For each acquisition channel of the array, the signals from the acoustic sensor and its respective preamplifier are digitized underwater by a dedicated electronic front-end called “AcouBoard“. The AcouBoard, shown in Fig. 5.8, is installed inside the FCM vessel. It is composed of two separated parts, both fed at 5 VDC by the CPS . One of them distributes the power to the preamplifiers, the other one is dedicated to the digitiza-

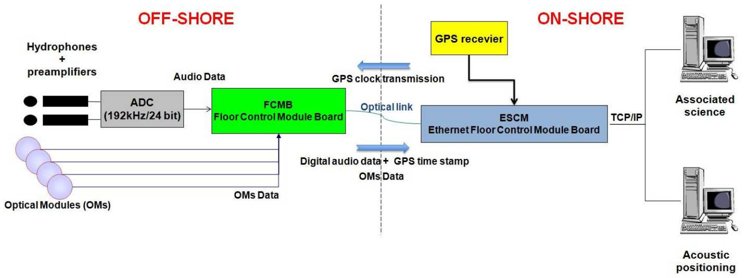

Figure 5.7: Data acquisition chain of a floor of the NEMO-SMO detector. The signals from hydrophones are sampled off-shore, time labelled and continuously sent to the shore station for real-time analysis

tion of the analogue signals coming from the acoustic sensors. The power section distributes power to the hydrophone's preamplifiers through two isolated output power lines (one for each hydrophone) at 5 VDC. The typical current for a couple of hydrophones is 200 mA. The board is kept safe from short-cuts, due to possible water seepages, by means of two *slow blow* fuses (one for each output line) that interrupt the power supply in case of prolonged over-current (1 A, 100 ms). The part of the AcouBoard dedicated to digitization of the signals coming from acoustic sensors, has been designed using professional audio technology components. This choice reduces costs and improves reliability with respect to custom systems developed by the other KM3NeT groups. The AcouBoard features two input audio channels, galvanically insulated from the input sources (hydrophones) by means of audio transformers. Analogue signals from transformers pass through signal conditioning circuit, having a nominal gain of +3 dB, and are sent to Crystal CS-5381 stereo analog-to-digital converter [98]. The later is a professional audio Multi-bit Delta-Sigma converter, that performs digitisation at 192 kHz rate with a resolution of 24 bit. The maximum input voltage of the Crystal CS-5381 is 2 V_{rms}. The nominal dynamic range of the converter is 120 dB at 96 kHz. The output signals from the analog-to-digital converter are encoded into the AES/EBU standard stereo protocol [99] by a Digital Interface Transmitter (DIT) Crystal CS-8406 [98]. The use of a standard protocol interfaces allows to manage the audio data with professional sound boards and commercial software and firmware reducing the costs and implementations time with respect to custom protocols. All AcouBoards are driven by the same Master Clock, derived by the NEMO Phase-II Master Clock, as described in Chapter 4. A novel technology was implemented to time-stamp audio data underwater with absolute GPS time. The digital AES/EBU data stream produced from the AcouBoard is, indeed, continuously sent to the FCMB. The FCMB labels the AES/EBU audio blocks (containing 192 audio samples) with the GPS time received from shore, embedding it in the audio protocol. In particular, the GPS time is written in the 192 bit control word composed by the *user bits* of a single AES/EBU block. The resolution of the acoustic data time labelling is 25 ns.

Figure 5.8: Picture of the AcouBoard. The AcouBoard distributes the power to the preamplifiers and performs the digitization of the acoustic signal at a frequency of 192 kHz with a resolution of 24 bit.

The audio data, labelled with the absolute GPS time of acquisition, are sent to shore in the main data stream together with the optical modules and oceanographic instruments data through the whole data transmission system of NEMO Phase-II detector. The time labelling calibration of the acoustic data is described in details in Chapter 6. The data stream for each acoustic sensor is about 6.3 Mbit/s.

5.3 On-shore data acquisition system

On shore, the audio data from each floor, written in AES/EBU standard, are extracted from the main data stream by the eFCM. The eFCM addresses acoustic data to a dedicated computer, called ADS (Acoustic Data Server), that hosts a professional AES/EBU sound card, model RME Hammerfall DSP AES-32 (Fig. 5.9) [100].

Figure 5.9: Picture of the sound acquisition card RME Hammerfall DSP AES-32.

For the SMO projects, 3 ADS are employed; each one acquires data from 3 floors (6 acoustic sensors). In each ADS a dedicate software developed by the SMO Collaboration, called AcouServer, acquires the AES/EBU data blocks from the the sound card, parses them in a proprietary data protocol (IADP - INFN Acoustic Data Protocol), described in Tab. 5.2, and addresses them via TCP/IP connection to a computer farm for analysis. Audio data will be available in real-time to science community for remote analysis. Following the recent refurbishment of the INFN-LNS Capo Passero infrastructure, SMO will be the first cabled large bandwidth acoustic array deployed in the deep Mediterranean Sea, at 3500 m depth, and it will be fully connected via optical fibre to the GARR (Italian Consortium for Research Network) backbone.

Header		28 byte
IDO	Observatory ID	1 byte
IDS	Storey ID (0-8)	1 byte
IDH	Hydrophone ID (0-1)	1 byte
FS	Sampling frequency (kHz)	1 byte
TGPS UW	Underwater UTC Time	10 byte (∗)
NFRM	Number of data frames	1 byte
NBITS	Number of bits per datum	1 byte
TGPS OS	On-shore UTC Time	10 byte(∗)
unused		2 byte
Payload		768byte
DATA	Acoustic samples	NFRM x 32bit words

(∗)TGPS Format
year: 1 byte
day: 2 bytes
seconds: 3 bytes
25ns units: 4 bytes

Table 5.2: INFN Acoustic Data Protocol (IADP). This protocol is used by the AcouServer to send via TCP/IP the data embedded in each AES/EBU block.

The data stream from the AcouServers is managed by a software architecture developed by the SMO Collaboration. The architecture is based on a modular structure, shown in Fig. 5.10. The analysis of the acoustic data is performed by a collection of software tools, called AcouModules, each AcouModule is installed in a dedicated computer called AcouFilter. The management of the AcoulFilters and the AcouModules is carried out by a graphical user interfaces, the AcouRun. The

AcouRun allows and controls IP connections between the AcouServers and the AcouModules and to it monitors the status of the AcouFilters (e.g CPU use, RAM use) and the data stream payload transmitted to each module by the AcouServers. An independent application was developed for detector positioning purpose as described in the following paragraph.

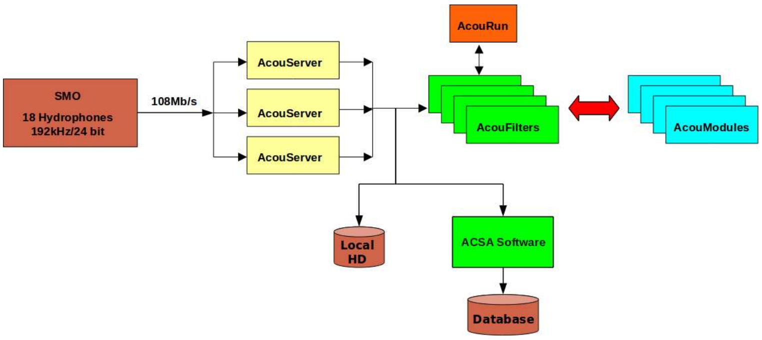

Figure 5.10: Synoptic view of the SMO data management system.

5.4 Acoustic positioning of the detector

As described in Chapter 2, the arrival direction of neutrinos in underwater telescopes is deduced by the Čerenkov track produced by secondary muons. In order to reconstruct the muon track with an accuracy of a few tenths of a degree, that is the necessary accuracy to point back the candidate neutrino sources, the position of each optical sensor of NEMO Phase-II has to be known with an accuracy of better than 20 cm, that is the diameter of the PMTs. Underwater acoustic positioning is performed by means of a Long Baseline (LBL) of acoustic beacons, anchored in known positions, and an array of acoustic sensors, hydrophones, installed in the mechanical structures to be positioned. Beacons' positions will be accurately geo-referenced and displaced at about 200 m from the tower, to form a Cartesian reference system of orthogonal axes. In Fig.

5.11 the scheme of the NEMO-SMO positioning system is shown. Accurate time of flight (TOF) measurement between beacon signal start-time (TOE - Time of Emission) and hydrophone signal reception stop-time (TOA - Time Of Arrival), will permit hydrophone positions' calculation by converting acoustic time of flight into distances and applying a triangulation method.

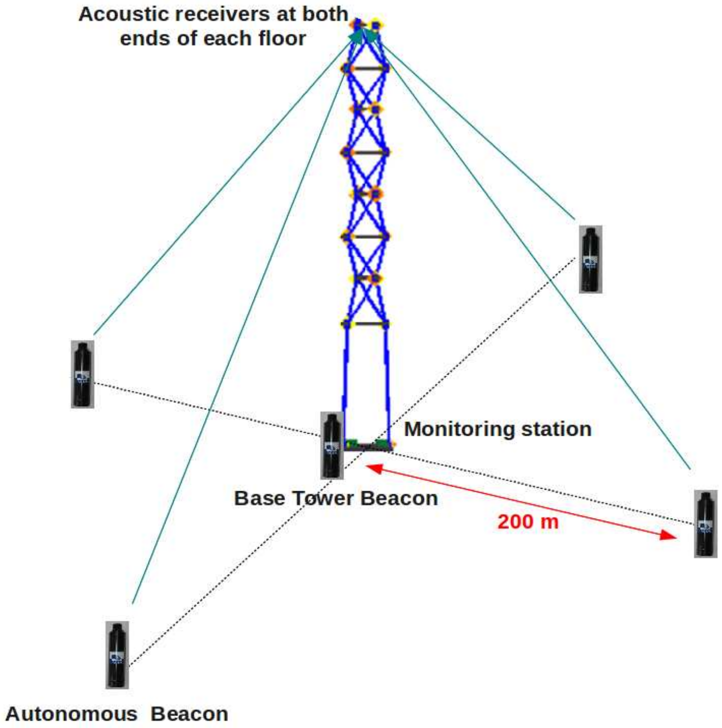

Figure 5.11: NEMO-SMO positioning system is based on the measurement of the time of flight of acoustic signals between a long baseline of acoustic beacons, anchored on the sea-floor, and target acoustic receivers, rigidly connected to the mechanical structures of the detector.

In order to calculate distances from TOF, the sound velocity along the water column must be also known. Sound velocity v_s in seawater is a function of temperature T, salinity S and pressure P and it varies between 1400 m/s and 1600 m/s in the Mediterranean Sea. The variation of these parameters with depth produces a vertical sound speed profile.

A empirical relation for the speed of sound in sea water was calculated by Mackenzie [88]

$$v_s(T,S,D) = a_1+a_2T+a_3T^2+a_4T^3+a_5(S-35)+a_6D+a_7D^2+a_8T(S-35)+a_9TD^3; \tag{5.0}$$

where T, S, and D are temperature in degrees Celsius, salinity in parts per thousand and depth in metres respectively and a_1,a_2, $\cdots$, a_9 are empirical constants. The range of validity of the Mackenzie relation covers: temperature from 2 to 30 °C, salinity from 25 to 40 parts per thousand, depths from 0 to 8000 m. In NEMO Phase-II the sound velocity in the site is calculated using pressure, temperature and salinity data measured with the CTDs installed on the 1^{st} floor and in the 7^{th} floor of the detector. Measurements of these quantities have been performed by the NEMO Collaboration many times in the past years in Capo Passero Site. Salinity and temperature are almost constant at depths ≥ 1000 m, as shown in Fig. 5.12 [83], and the sound velocity depends mainly on depth.

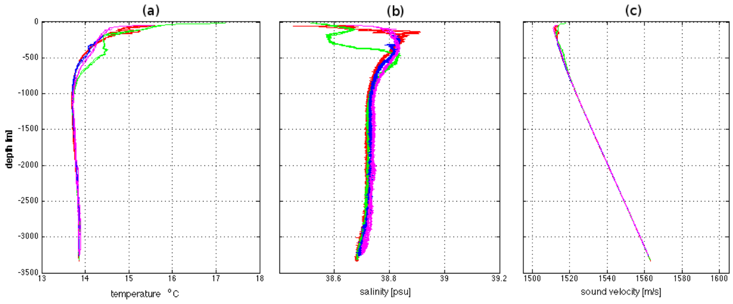

Figure 5.12: Profiles of temperature (a) and salinity (b) measured in the Capo Passero site. The profiles refer to the campaigns performed during December 1999 (2 deployments, blue lines), March 2002 (4 deployments, red lines) and May 2002 (2 deployments, green lines), August 2002 (3 deployments, pink lines) [83]. In panel (c) the sound velocity profiles calculated trough the Mackenzie relation from the measurements of each campaign .

Once the distances between the beacons and the monitoring station, and the sound velocity in the water column have been determined, one is able to calculate the TOF, as difference between TOA and TOE. In more details, the TOE of each beacon pulse, is obtained measuring the TOA of this pulse at the hydrophones mounted on the base tower (monitoring station) that are anchored on the seafloor in known positions.

5.4.1 Acoustic beacons

As described above, the positioning system is based on the measurements of beacons pulses time of arrival (TOA) at a given acoustic receiver. The positioning of the NEMO-SMO detector is performed using 5 acoustic beacons, manufactured by ACSA [101] (Fig. 5.13). Four of them are autonomous beacons, anchored on the seabed at about 200 m from the base of the detector, one additional beacon, located at the base of the detector is connected with the power electronics of the tower (12 V). The autonomous beacons are fed by a battery pack installed in pressure resistance glass spheres. In order to unequivocally recognize which beacon has emitted the pulse, a technique called Time Spectral Spread Codes (TSSC) has been adopted. Opposite to traditional tracking pingers, that transmit pulses at regular intervals, a TSSC family of codes is based on pseudo-random suites of acoustic pulses, time spaced in such a way that the codes of the family form an orthogonal base in the time domain. In this way all the beacons can transmit their characteristic pulse sequence at the same acoustic frequency. Each beacon transmits its TSSC sequence with a period of about 12 sec, i.e. a pattern of 6 pseudo-random pulses (spaced by $\sim$ 2 sec) that is different from the others. In this way a typical beacon pulse sequence can be recognized without ambiguity. Each pulse is a sinusoidal packets of 32 kHz ant its duration is about 5 ms. The sequence of pulses is defined in such a way to avoid overlap between two consecutive pulses. The amplitude of each pulse is 180 dB re 1 μPa at 1 m. In Tab. 5.3 we report the TSSC codes lookup table of the five beacons used NEMO-SMO project.

Figure 5.13: Picture of an ACSA beacon used for the positioning of the NEMO-SMO detector.

	Beacon 1	Beacon 2	Beacon 3	Beacon 4	Beacon 5
Pulse 1	0.000	0.000	0.000	0.000	0.000
Pulse 2	1.800	1.891	1.956	2.138	1.852
Pulse 3	3.808	3.886	3.860	4.120	4.003
Pulse 4	5.829	6.011	6.024	5.933	5.881
Pulse 5	7.772	7.928	8.084	7.798	7.954
Pulse 6	9.611	9.754	10.183	9.832	10.001
Rate	11.697	11.684	12.295	11.801	12.178

Table 5.3: Time of emission of each beacon pulse.

In the shore station software tools developed by ACSA are installed in a dedicated PC. This tools decode the “raw” hydrophone data sent by the AcouServers and calculate the position of each hydrophone as a function of time. The software recognizes and extracts the pulses of a specific beacon from the hydrophones raw data stream. The beacons are unequivocally identified thanks the use of the TSSC codes lookup table. From the monitoring station data, emission times of the beacon pulses are obtained taking into account the sound velocity in the medium. The time of flight (TOF) of each beacon pulse to reach each hydrophone installed on the detector floors results from TOF =TOA-TOE. Since the sound velocity profile in the water column is known, the TOF gives the distance between hydrophone and beacon. Hydrophones positions are calculated by means of geometrical triangulation. A synoptic view of the APS software is shown in Fig. 5.14.

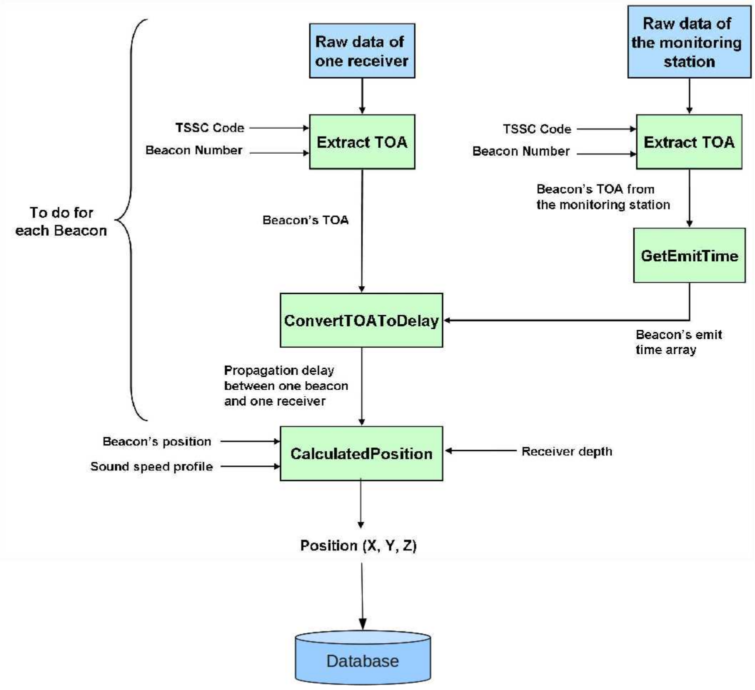

Figure 5.14: Block diagram of the software used to calculate the hydrophones positions.

5.4.2 LBL calibration and clock drift monitoring

To achieve required accuracy on the detector positioning an accurate calibration of the LBL must be performed and the clock drift of the stand-alone beacons must be taken into account. The acoustic position reconstruction procedure relies on the precise knowledge of the beacon position, that must be known with an accuracy of the order of 15 cm. The beacon absolute positions and relative distances are determined, acoustically, during the detector deployment operations using a ROV equipped with a GPS time synchronized USBL (ultra-short baseline) positioning system, a receiver and a high accuracy pressure sensor. This procedure permits to determine the LBL coordinate system, necessary to calculate the hydrophones absolute position. The knowledge of the correct orientation of the reference system is important to determine the tower position and orientation, in order to evaluate the absolute direction of the reconstructed muon tracks.

Chapter 6

Test and characterization of the NEMO-SMO acoustic array

In this chapter the tests carried out to measure the performances of the NEMO-SMO acoustic array are described. Tests on the acoustic data acquisition chain were performed at the INFN-LNS, where a complete test-bench, including final electronic boards, electric connections and power supply system were set up. A 100 km long optical link was also used to simulate the data transmission along the real underwater electro-optical cable. Extensive calibration test of the devices, performed at the CNR-IDASC (Consiglio Nazionale delle Ricerche - Istituto Di Acustica e Sensoristica "Corbino") facility [102], are described and first results are reported

6.1 Intrinsic electronic noise measurement

In order to evaluate the performances of the SMO array, the intrinsic electronic noise of the data acquisition system has to be measured. This measurement allows to estimate the smallest amplitude of the acoustic signals that can be detected by each hydrophone. As described in Chapter 5, SMO hosts: fourteen SMID TR-401 hydrophones on the base and on floors 1÷6 of the detector, two Sensor Technology Ltd SX-30 FFR hydrophones on floor 7 and two custom piezoelectric sensor installed into special Opto-Acoustic Modules (OAM). All hydrophones are interfaced with SMID AM-401 preamplifiers, whose input (and thus output) noise level provides the largest contribution to electric noise. OAM are novel devices, integrated and operated for the very first time within this experimental activity.

The electric noise of each acoustic sensor channel has been measured at INFN-LNS with a test bench including hydrophones preamplifiers, a standars AcouBoard, a standard FCMB, a standard eFCMB and a RME HDSP acquisition sound card. The communication between FCMB and eFCMB was set up using two 100 km long optical fibres (one fibre for on-shore/off-shore data transmission, the other one for off-shore/on-shore data transmission), having the same optical properties of the fibres employed in the main underwater electro-optical cable of the Capo Passero Site. The noise of each hydrophone channel was measured including, in the DAQ chain described above, a preamplifier SMID AM-401, with shorted input. In order to avoid external electromagnetic noise (that is not present in the underwater environment) the preamplifier was put in a shielded metallic box. Audio data have been thus acquired and analysed by means of a dedicated MATLAB macro, performing a periodogram obtained by a Fast Fourier Transform at 32768 pts. In Fig. 6.1 the typical spectrum of electronic noise for the hydrophone channels is shown: the total noise power, that is the integral of the average electric noise spectrum is equal to -72 dB re 1 V_{rms}.

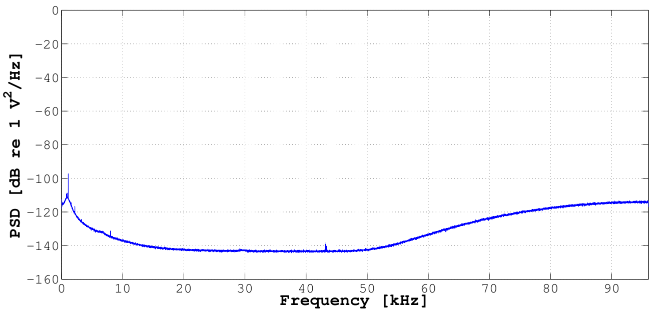

Figure 6.1: Spectrum of the SMO data acquisition electronic noise of the SMID TR-401 and Sensor Technology Ltd SX-30 hydrophones. The total power is -72 dB re 1 V_{rms}.

The increase of electric noise at frequencies above 50 kHz is mainly due to the contribution of the intrinsic noise of the analog-to-digital converter (Crystal CS-5381) installed on the AcouBoard, that has been previously measured [103].

The measured electronic noise was then converted in units of equivalent acoustic pressure (Fig. 6.2) taking into account the typical sensitivity of the SMID TR-401 hydrophone (including preamplifier), that is almost constant in the whole bandwidth, and it is about -172 dB re 1 V/μPa.

In Fig. 6.2 the equivalent pressure level spectrum of the electric noise is compared to the expected acoustic noise in deep sea (dot blue lines). The SS0 (Sea State 0) line indicates the background acoustic noise in condition of calm sea and absence of impulsive acoustic sources.

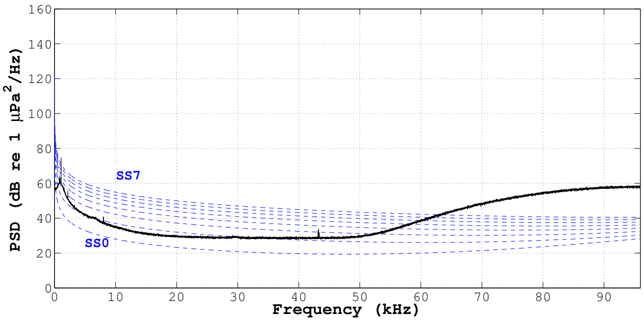

Figure 6.2: Average power spectral density of the intrinsic electric noise of the SMO data acquisition system in equivalent acoustic pressure for the SMID TR-401 hydrophone (solid black line). The dotted blue lines represent the expected background acoustic noise for different sea-state conditions.

Obtained results clearly show that SMO system is suitable for searching of impulsive signals with power spectral density larger than 30 $\mu\mathrm{Pa}^2/\mathrm{Hz}$ in the range between 10 kHz and 50 kHz.

The electrical noise of the channels reading-out the piezo-sensors developed by ECAP, installed in the Opto-Acoustic Modules (OAMs) of the NEMO floor 8, has been also measured. In this case, acoustic data were acquired powering up the piezoelectric sensor and preamplifier board. The measurement was carried out in final sensor configuration, that is mounted inside the OAM (Fig. 5.6). In order to measure the occurrence of electromagnetic interferences due to PMT readout electronics, the PMT and the FEM were also switched on. The spectrum obtained for the OAM channel is shown in Fig. 6.3: The noise total power is -35 dB re 1 V . In Fig. 6.4 we eventually compare the typical average electronic noise of ECAP and SMID channels in units of equivalent acoustic pressure with the expected beacon pulses at reference distances of 100 m and 1000 m. We have assumed, from data sheet provided by the ECAP group, that the sensitivity of the ECAP piezo-sensor is flat and equal to -145 dB re 1 V/μPa.

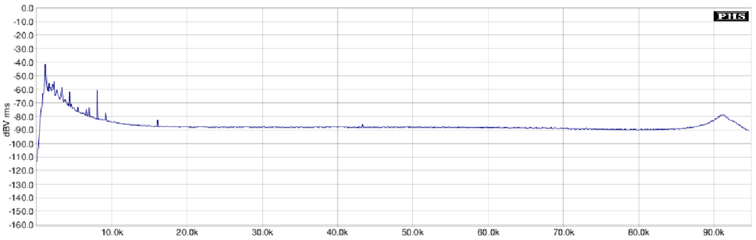

Figure 6.3: Spectrum of the data acquisition electronic noise of the piezoelectric sensors installed in the OAM. The total power is -35 dB re 1 V$_{rms}$.

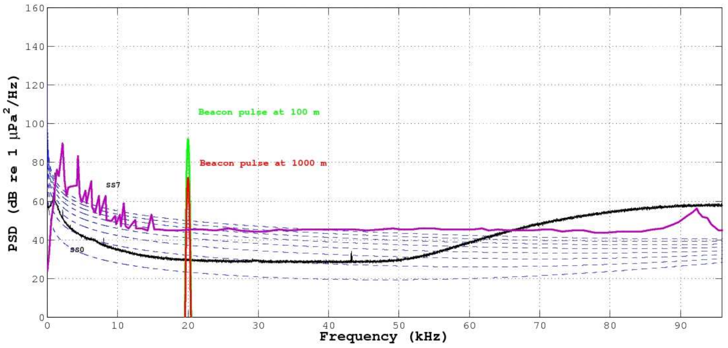

Figure 6.4: Noise spectrum of the data acquisition system in equivalent acoustic pressure for the SMID TR-401 hydrophone (black line) and piezo-sensor installed in the Optical-Acoustic Module (pink line) compared with the expected beacon pulse at distances of 100 m (green line) and 1000 m (red line).

6.2 SMO tests in waterpool

In November 2011 two full SMO floors were tested at the waterpool of CNR-IDASC (Istituto di Acustica e Sensoristica “Orso Mario Corbino”) of Rome [102]. The dimension of the water pool are 4 m x 5 m x 5.30 m (h) (Fig. 6.5). For these tests the waterpool was equipped with motorized mechanical arms to locate transducer and receivers at known distances. Salinity and temperature of the water were constantly monitored thanks to dedicated probes, in order to determine speed of sound in water.

Figure 6.5: Picture of the CNR-IDASC waterpool, used for the tests in water of the SMO hydrophones.

The aim of the tests was twofold: check the calibration in amplitude and frequency of a typical channel (SMID hydrophones) and of a FFR channel; measure the latency time of a whole typical acquisition channel of SMO (see Section 5.6). The test bench used for SMO floor characterization in water is sketched in Fig. 6.6. The setup can be logically divided in two parts: the acoustic waves emitter system, provided by the CNR-IDASC, and the SMO floor acoustic signal detection system, provided by the NEMO-SMO Collaboration. The acoustic waves emitter system consists of a calibrated spherical transducer, model ITC 1032 [104], an AGILENT 33220A waveform generator [105] and a DC-5 MHz high voltage amplifier, model Falco Systems WMA-300 [106]. The SMO floor acoustic detection system includes: a Symmetricon XLi GPS receiver [107], a time distribution board (Fan Time), 2 eFCMB, 2 FCMB, 2 AcouBoards, two SMID TR-401 hydrophones (S/N 14 and S/N 25) and two Sensor Technology Ltd SX-30 Free Flooded Ring (FFR) hydrophones (S/N 05 and S/N 788), integrated with preamplifiers and moulded with the final cables. The FFRs used in the test are the ones integrated on floor 7 of SMO, the SMID hydrophones were chosen among the same production batch of sensors integrated on SMO.

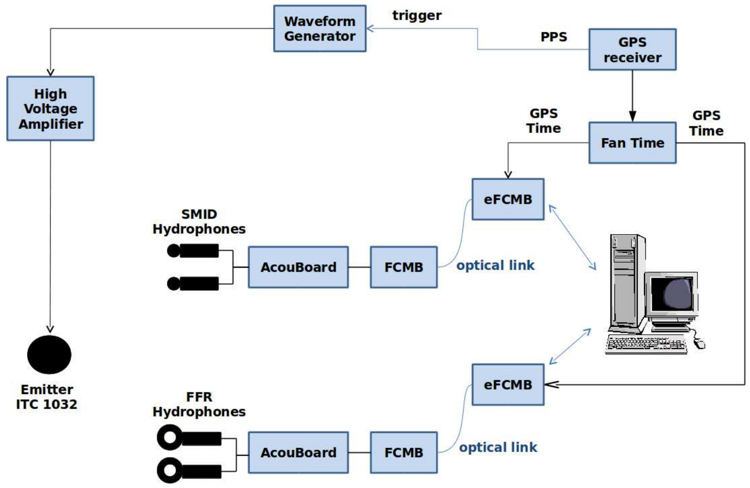

Figure 6.6: Sketch of the test-bench used for the measurements in waterpool. The test bench included all key-elements of the SMO data acquisition system.

The background noise of the test environment was measured acquiring signals recorded by the hydrophones dip into the waterpool in absence of transducer signals. Fig. 6.7 shows for each hydrophone the periodograms of the recorded data. The average total power measured with SMID hydrophones was about -38 dB re 1 V, the average total power measured by the FFR hydrophones was about -49 dB re 1 V. The measured background noise can be attributed to cumulative effects of acoustic and electromagnetic environmental noise. The presence of several spikes in the measured noise spectrum shows that the environment is densely electromagnetically polluted, a measurement condition that is much worse than expected in deep sea.

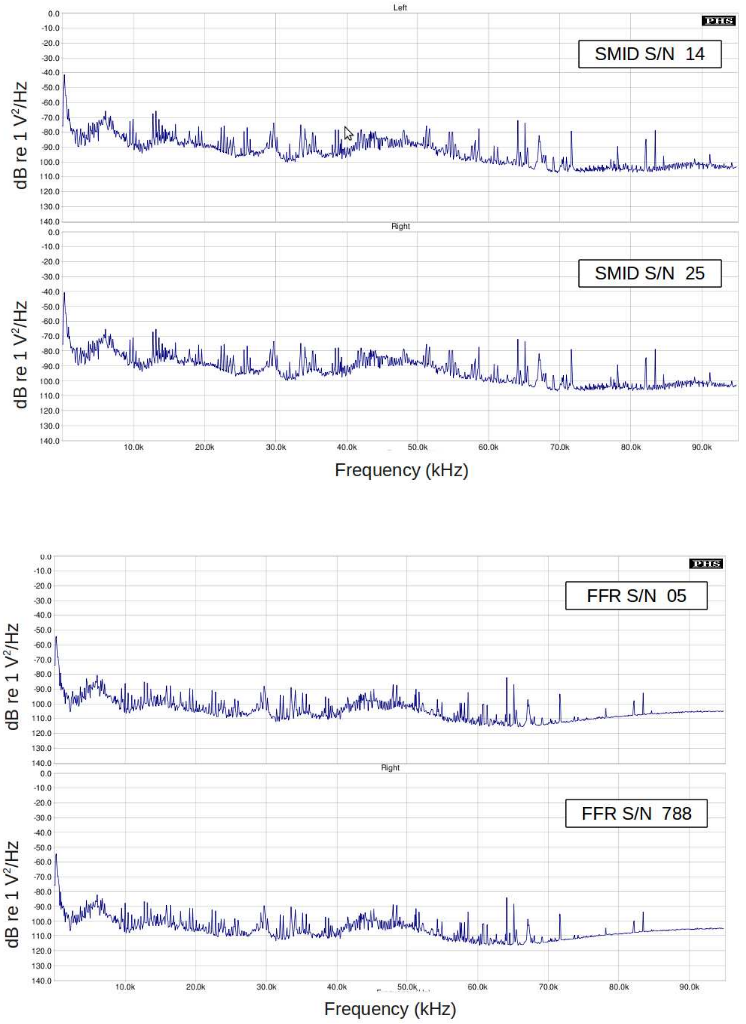

Figure 6.7: Periodograms of the average background noise at the CNR-IDASC waterpool measured with SMID (top) and FFR hydrophones (bottom).

Hydrophones characteristics have been measured using, as calibration signals, sinusoidal acoustic waves of different frequencies and amplitudes. Amplitudes, frequencies and lengths of the test signals have been set up by means of the user interface of the waveform generator. In order to avoid acoustic interference effects due to reflections of the acoustic waves on either waterpool walls or water surface, the measurements have been performed placing the transducer and hydrophones at the centre of the pool and using, as calibration signals, short sinusoidal pulses of 5 cycles. The emission of the pulses has been triggered using the PPS (Pulse Per Second Signal) output signals provided by the GPS receiver. Acoustic pulses have been recorded by the 4 test hydrophones, placed at known distances from the acoustic source, as shown in Fig. 6.8.

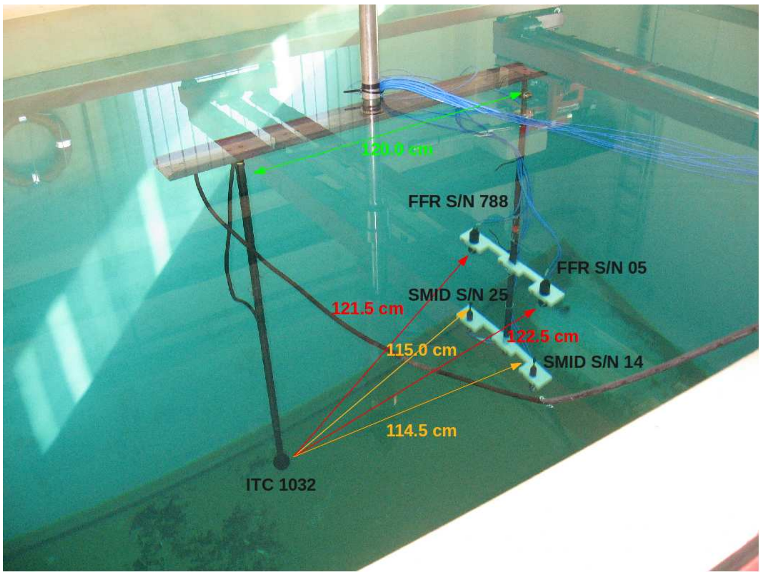

Figure 6.8: Geometrical setup for the evaluation of the hydrophone ceramics response time.

The measurements have been carried out using calibration signal of frequencies of 10 kHz, 20 kHz, 32 kHz, 40, kHz and 50 kHz. For each frequency, runs of 120 acoustic emissions at 3 different input voltage levels (thus acoustic pressure) have been performed. In particular, the measurement have been performed setting the amplitude of the input electrical signal produced by the waveform generator at 100 mV$_{rms}$, 200 mV$_{rms}$ and 400 mV$_{rms}$. Fig. 6.9, Fig. 6.10, Fig. 6.11, Fig. 6.12 and Fig. 6.13, show, for each frequency, the acoustic pulses recorded by the 4 hydrophones. For frequencies of 10 kHz, 20 kHz, 40, kHz and 50 kHz the figures show the results obtained using the waveform generator output amplitude of 400 mV$_{rms}$; Fig. 6.11 shows the results for 32 kHz pulses of amplitude set to 200 mV$_{rms}$. Each figure shows the 120 acoustic pulses superimposed.

The figures highlights that the response of each individual sensor is almost identical in the same run. This means that the transfer function of each channel depends only on amplitude and frequency of the input acoustic wave. It is also worth to mention that the response to a given acoustic excitation of SMID hydrophones does not change as a function of frequency. Moreover, the signals acquired by SMID hydrophones reproduce exactly the number of sinusoidal cycles emitted by the calibrated transducer and the amplitude of each cycle is almost constant. On the contrary, for FFR hydrophones, the waveform of the acquired signals changes as a function of the frequency: FFR hydrophones do not reproduce the same number of cycles of the test acoustic pulses and, in each pulse, the amplitude of each cycle is not constant. In addition, while both SMID channels show an almost identical response to the same acoustic

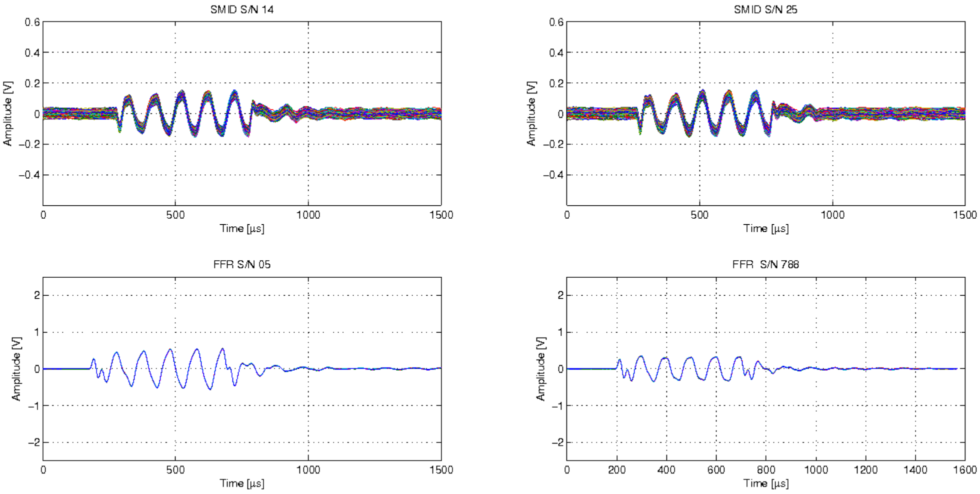

Figure 6.9: Acoustic signals acquired by the SMID and FFR hydrophones using as electrical input signals of the IDASC acoustic emission system a 5 cycles-long sinusoidal pulses with a frequency of 10 kHz and an amplitude of 400 mV$_{rms}$.

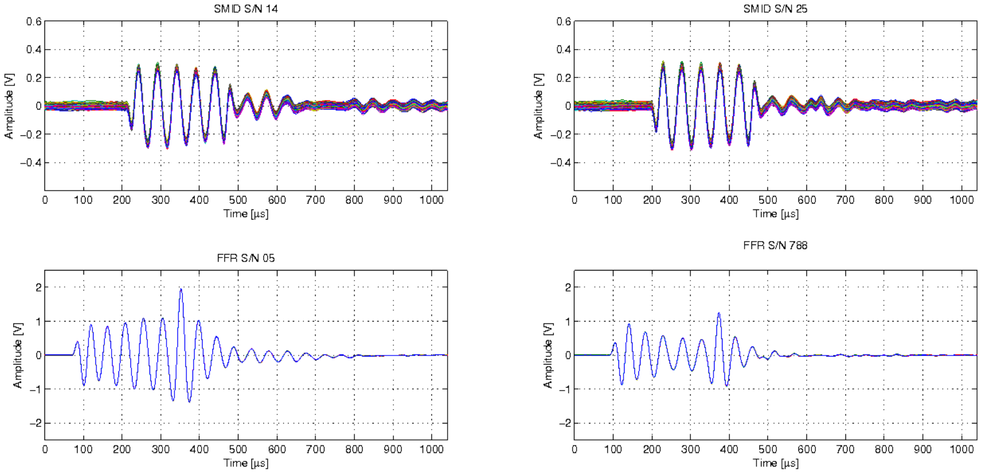

Figure 6.10: Acoustic signals acquired by the SMID and FFR hydrophones using as electrical input signals of the IDASC acoustic emission system a 5 cycles-long sinusoidal pulses with a frequency of 20 kHz and an amplitude of 400 mV_{rms}.

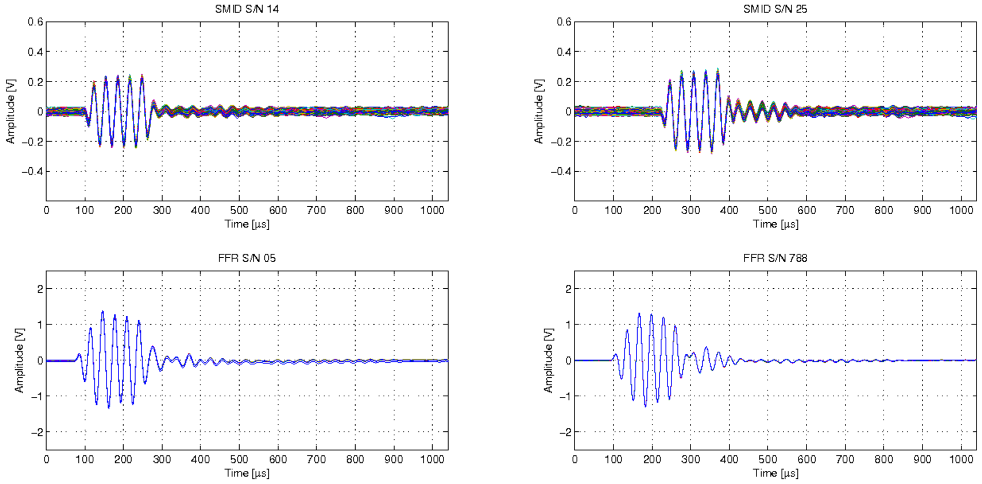

Figure 6.11: Acoustic signals acquired by the SMID and FFR hydrophones using as electrical input signals of the IDASC acoustic emission system a 5 cycles-long sinusoidal pulses with a frequency of 32 kHz and an amplitude of 200 mV_{rms}.

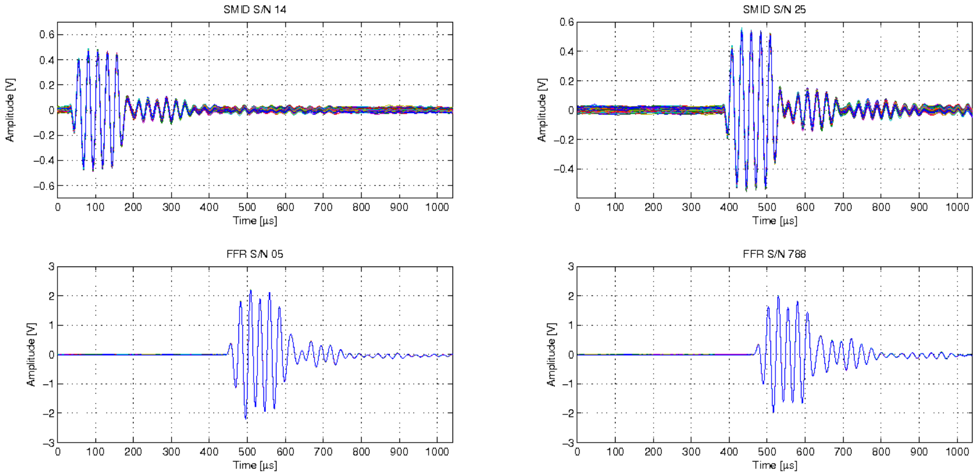

Figure 6.12: Acoustic signals acquired by the SMID and FFR hydrophones using as electrical input signals of the IDASC acoustic emission system a 5 cycles-long sinusoidal pulses with a frequency of 40 kHz and an amplitude of 400 mV_{rms}.

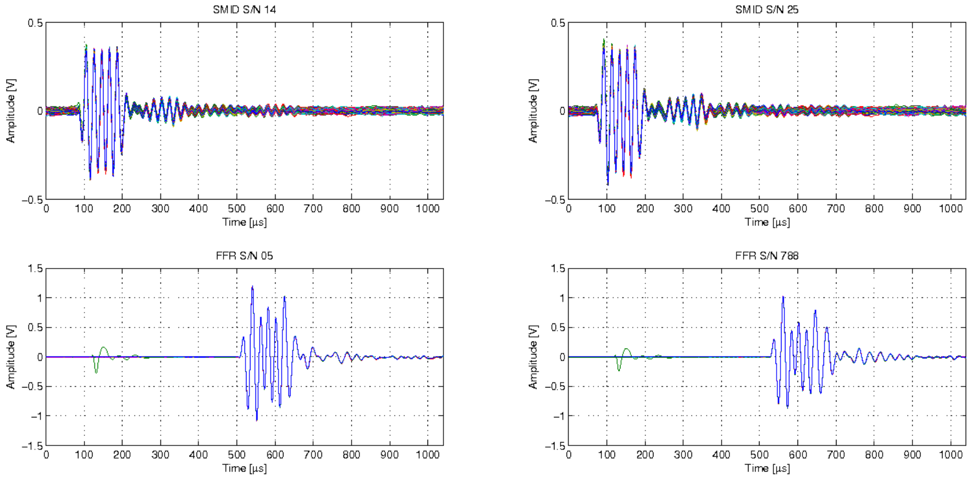

Figure 6.13: Acoustic signals acquired by the SMID and FFR hydrophones using as electrical input signals of the IDASC acoustic emission system a 5 cycles-long sinusoidal pulses with a frequency of 50 kHz and an amplitude of 400 mV_{rms}.

pulse, acoustic signal acquired by the two FFR hydrophones appear very dissimilar. This implies that the use of FFR hydrophones for KM3NeT detector will require a preliminary calibration procedure for each sensor. For SMID hydrophones, proposed by the NEMO and SMO Collaborations, *in prima facie* the same transfer function can be adopted for all hydrophones. For SMID hydrophones the linearity of the response of ceramics to acoustic pressure amplitude (as a function of frequency) has been also verified. These results confirm the ones provided by the manufacturer and previous calibrations performed at NURC (NATO Undersea Research Centre). The analysis of all data sets described before was carried on. For each data set, the amplitude of the received signal has been determined as the mean value of the envelope of the signal Hilbert transform. The results of the analysis for the channel equipped with SMID S/N 14 hydrophone are shown in Fig. 6.14, Fig. 6.15, Fig. 6.16, Fig. 6.17 and Fig. 6.18, that highlight the linearity of the ceramics response. The linearity of the data acquisition electronics, including hydrophone preamplier (gain of +38 dB) had been verified in previous tests reported in [103].

In the above mentioned figures, the experimental data with the fit obtained using a regression line passing through the axis origin (red line) are shown together. For each frequency, the regression lines are in good agreement with the experimental data. The goodness of the fit has been estimated calculating the coefficient of determination R^2, shown in each figure.

Eventually, the sensitivity of the data acquisition system of SMID hydrophone channels, i.e. the voltage response of the whole system to a given pressure wave as a function of the frequency, has been measured. The measurements were carried out analysing data taken at frequencies of 10 kHz, 20 kHz, 32 kHz, 40 kHz and 50 kHz and input amplitude of 400 mV_{rms}. For each frequency, the sensitivity of the channel *S(f)* is

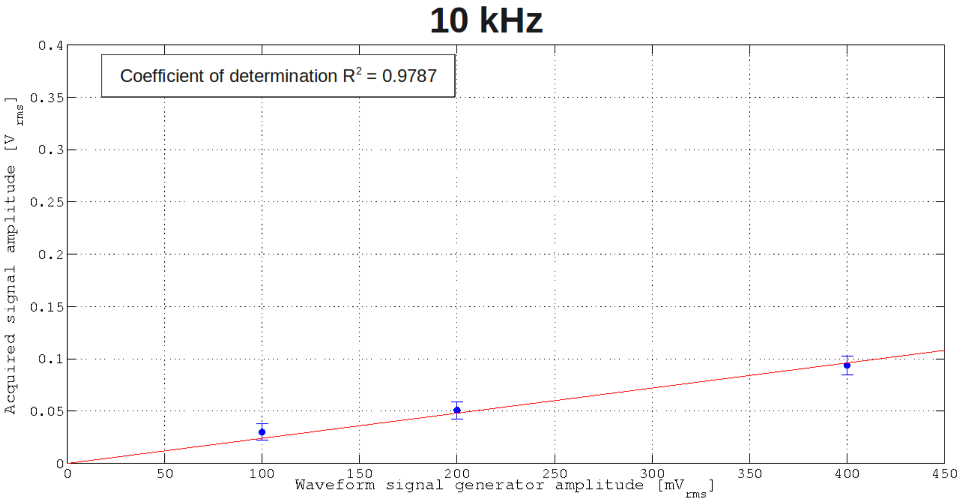

Figure 6.14: Amplitude of 10 kHz sinusoidal acoustic pulses acquired through the SMID S/N 14 hydrophones as a function of the amplitude of the input electrical signals produced by the waveform generator. The red line indicates the regression line passing for the axis origin.

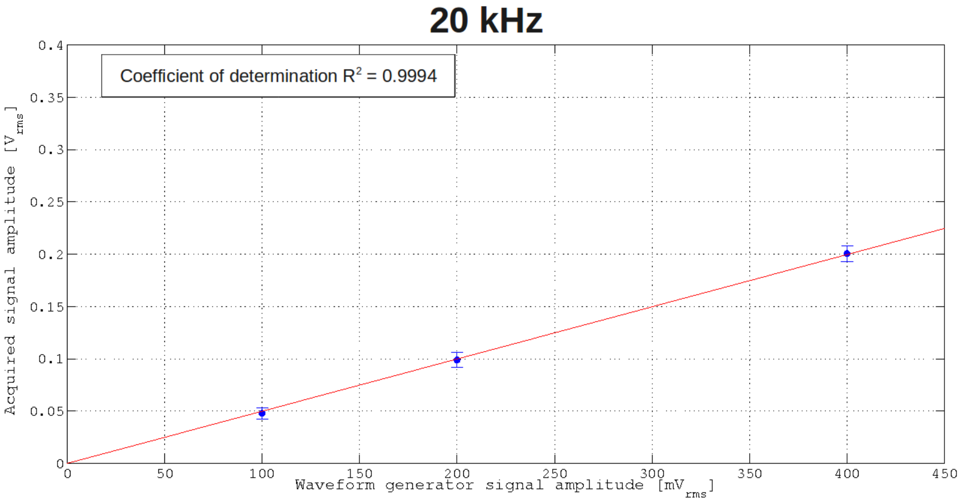

Figure 6.15: Amplitude of 20 kHz sinusoidal acoustic pulses acquired through the SMID S/N 14 hydrophones as a function of the amplitude of the input electrical signals produced by the waveform generator. The red line indicates the regression line passing for the axis origin.

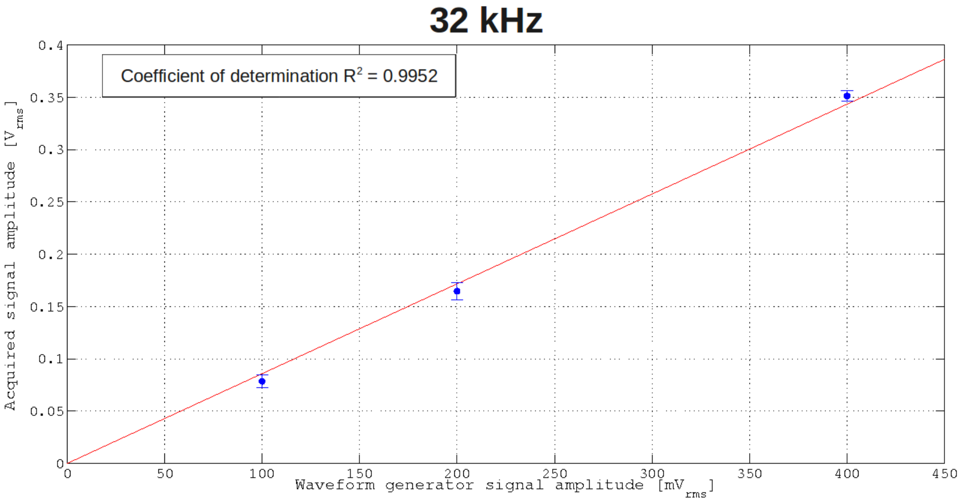

Figure 6.16: Amplitude of 32 kHz sinusoidal acoustic pulses acquired through the SMID S/N 14 hydrophones as a function of the amplitude of the input electrical signals produced by the waveform generator. The red line indicates the regression line passing for the axis origin.

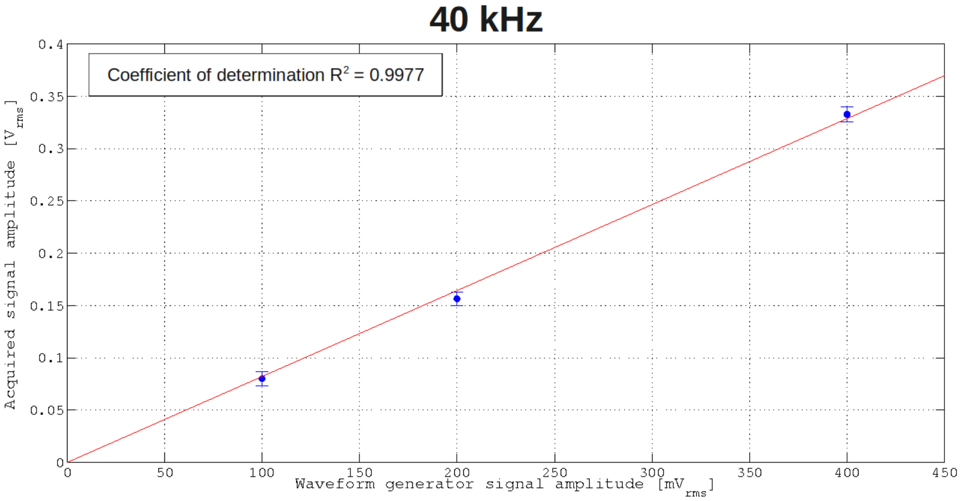

Figure 6.17: Amplitude of 40 kHz sinusoidal acoustic pulses acquired through the SMID S/N 14 hydrophones as a function of the amplitude of the input electrical signals produced by the waveform generator. The red line indicates the regression line passing for the axis origin.

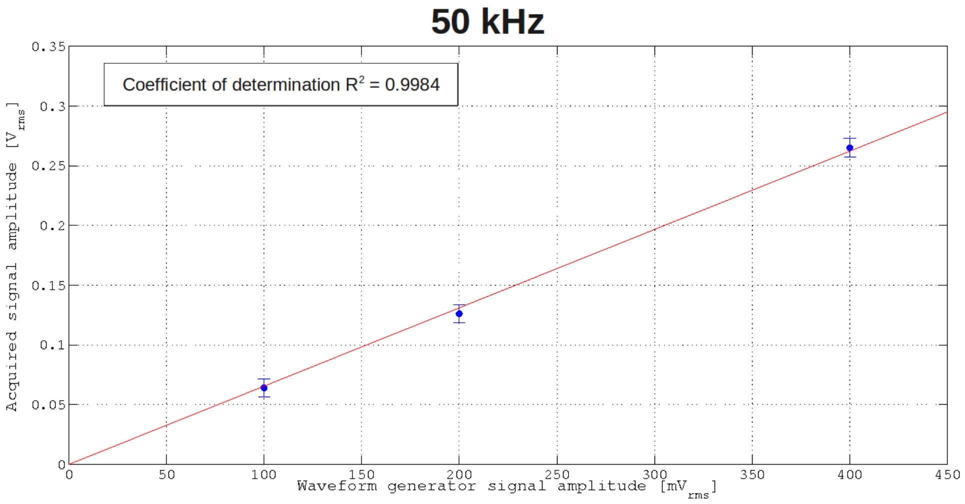

Figure 6.18: Amplitude of 50 kHz sinusoidal acoustic pulses acquired through the SMID S/N 14 hydrophones as a function of the amplitude of the input electrical signals produced by the waveform generator. The red line indicates the regression line passing for the axis origin.

given by:

$$S(f) = \frac{A_{acq}(f)}{A_{press}(f)}. \tag{6.0}$$

where A_{acq} is the average amplitude of the signal recorded by the SMO data acquisition system and $A_{press}(f)$ is the amplitude of the pressure wave that reaches the hydrophone. $A_{press}(f)$ has been calculated taking into account the TVR (transmission voltage to response) of the ITC 1032 transducer, provided by the manufacturer (see Tab. 6.1), the distance between emitter and hydrophone, the output voltage of the signal generator, the gain of the preamplifier (x46 constant at all frequencies and amplitudes) and the electrical line losses due to the impedance matching of the CNR-IDASC acoustic emission system.

Fig. 6.19 and 6.20 show the sensitivity of the whole SMO data acquisition channel (blue dots), measured respectively for the channels including SMID S/N 14 and SMID S/N 25 hydrophones, compared with

Frequency (Hz)	Transmitting Response to Voltage (dB re 1uPa/V)	Expand. uncert. (dB)		Frequency (Hz)	Transmitting Response to Voltage (dB re 1uPa/V)	Expand. uncert. (dB)
5000	114,9	1,3		28000	145,7	0,9
6000	118,0	1,2		29000	146,6	0,8
7000	121,0	1,1		30000	147,4	0,8
8000	123,1	1,0		31000	147,8	0,9
9000	124,7	1,0		32000	148,6	0,9
10000	126,3	1,0		33000	148,7	0,9
11000	127,7	1,0		34000	148,3	0,9
12000	129,1	1,0		35000	148,1	0,9
13000	130,3	0,9		36000	147,7	0,9
14000	131,8	0,9		37000	147,0	0,9
15000	133,0	0,9		38000	146,5	0,9
16000	133,9	0,9		39000	145,9	0,9
17000	134,7	0,9		40000	145,1	1,0
18000	135,6	0,9		41000	144,4	0,9
19000	136,3	0,9		42000	144,0	0,9
20000	137,3	0,9		43000	143,8	0,9
21000	138,5	0,9		44000	143,1	0,9
22000	139,7	0,9		45000	142,9	0,9
23000	141,0	0,9		46000	142,6	0,9
24000	142,0	0,9		47000	142,4	0,9
25000	142,9	0,8		48000	142,2	0,9
26000	143,8	0,9		49000	141,7	0,9
27000	144,9	0,9		50000	141,6	0,9

Table 6.1: Transmitting response to voltage of the ITC 1032 transducer as function of the frequency. In the third column the measurement accuracy is reported.

the sensitivity of the assembly hydrophone + preamplifier (shaded area), previously measured at NURC.

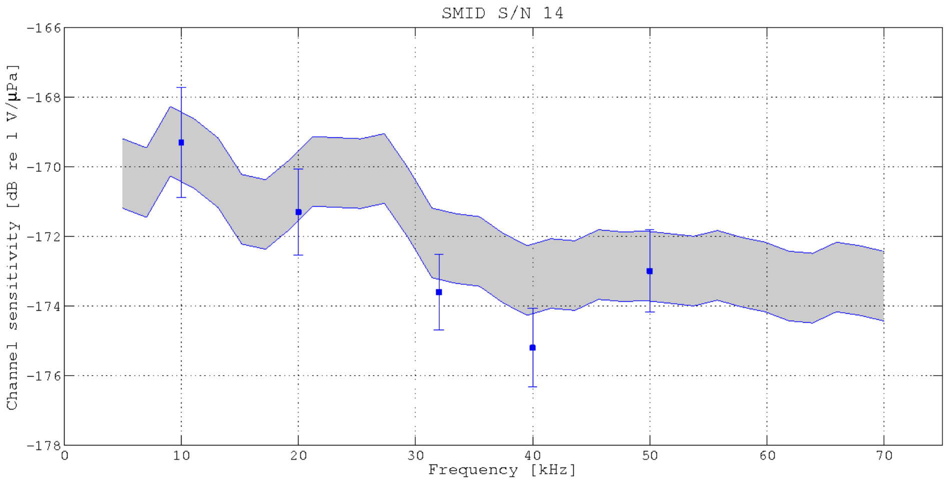

Figure 6.19: Sensitivity of the whole SMID S/N 14 acquisition channel (blue dot), compared with the sensitivity of only hydrophone+preamplifier assembly (shaded area).

Our experimental data are in agreement, within the experimental error, with the nominal sensitivity of the hydrophone + preamplifier

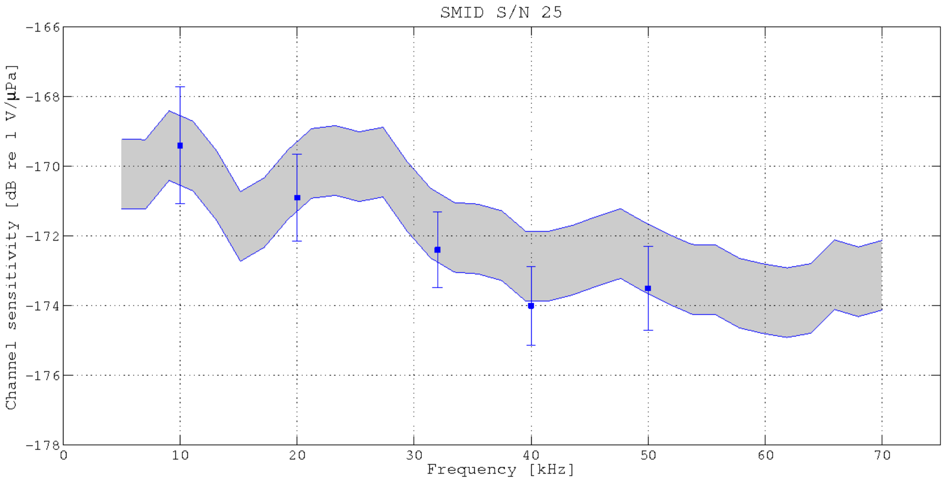

Figure 6.20: Sensitivity of the whole SMID S/N 25 acquisition channel (blue dot), compared with the sensitivity of only hydrophone+preamplifier assembly (shaded area).

system. These results confirm the hypothesis that data acquisition electronics of SMO does not introduce further undetermined amplification coefficients on the measurements of the amplitude of the acoustic wave.

6.3 Time calibration measurements

As described in Chapter 5, one of the main tasks of the SMO array is to provide acoustic positioning of the NEMO Phase II detector mechanical structure, detecting acoustic signals emitted by the long baseline of acoustic beacons anchored on the sea-floor. The performances of the acoustic positioning system (APS) are directly related to the uncertainty on the measurements of the Time Of Arrival (TOA) of the beacon signal at the acoustic sensors. TOA uncertainty depends on the accuracy stability of the beacons' clocks and on the accuracy of hydrophones clock. As for OM time calibration (see Chapter 5), the electronic latency of acoustic devices must be fixed and known. The latency time of the SMO data acquisition chain has been therefore measured. the total latency of system can be attributed to two contributions: one depends on the data front-end of data acquisition electronics; the other one depends on the mechanical response of hydrophones ceramics to acoustic waves. These two contribution have been measured separately, as described in the following. The setup used for the measurements of the electronic latency is sketched in Fig. 6.22. It included the whole acoustic data acquisition system of a typical SMO floor, a GPS receiver Symmetricom Xli, providing absolute GPS time for the time stamping of the data and reference clock for the FCMB, and a waveform generator, model AGILENT 33250A. The electronics latency has been measured sending a known electrical signal, produced by the waveform generator to the AcouBoard input at known time. The time difference between the signal emission time and the signal reception time embedded in the recorded audio signal was therefore measured. The two signals were measured using the same absolute GPS time: the trigger for the waveform generator emission was, in fact, provided by the FCMB. Using FCMB trigger, the absolute emission time of each pulse (T_{em}) is known, in fact, with an accuracy of 100 ps [108]. For these latency measurements the electrical signal fed into preamplifier was a 156.3 μs long sinusoidal wave of 32 kHz. The input signal was acquired by the SMO electronics chain (sampling rate of 192 kHz). The absolute time of the recorded signal was recovered using the absolute GPS time stamps embedded by the FCMB in the data stream. In details, the absolute arrival time of the acquired signal was determined using a cross-correlation function beetween the acquired signal and the input signal. The acquired data were re-sampled offline at 192 MHz, to reach an accuracy in time resolution of about 5.2 ns (see Fig. 6.21).

The GPS time attributed to the sample showing the maximum of the cross-correlation function (T_{corr}) is therefore the absolute time associated by the acquisition electronics to the arrival of the digitized test signal. Eventually, the absolute time delay and thus the electronic la-

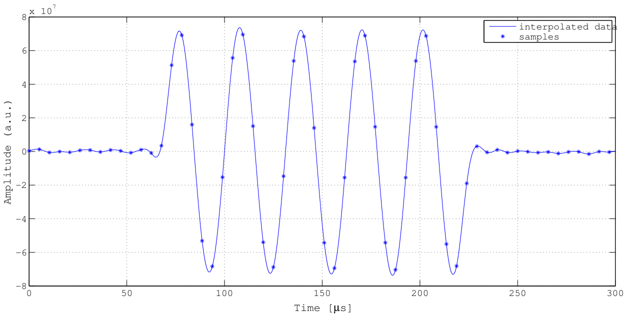

Figure 6.21: In order to improve the resolutions of the measurements of the electronics latency, the test signal, acquired at 192 kHz, has been resampled at 192 MHz (resolution of about 5 ns).

tency ($T^{el}_{latency}$) was calculated through the relation:

$$T^{el}_{latency} = T_{corr} - T_{em} - (T_{gen} + T_{cabling}). \tag{6.0}$$

taking into account the signal generator latency time (T_{gen}= 75 ± 5 ns) and cable delays ($T_{cabling}$).

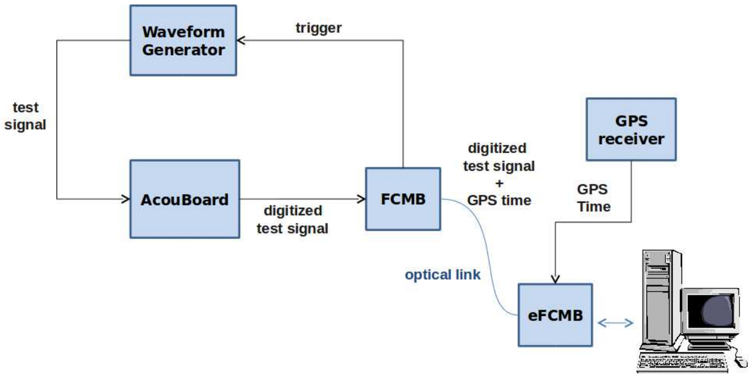

Figure 6.22: Schematic view of the test-bench used for the time latency measurement of the SMO acquisition electronics.

As quoted before, the data transport system ensures very low jitter (∼ 100 ps) and known and fixed time latency. On the contrary, deterministic latency of the AcouBoard haven't measured before. In order to verify the stability and to measure the latency time of the board, 20 acquisition runs were performed using the setup described before, each containing 100 test signals. At the end of each run the whole DAQ system was switched off and restarted. The average value of the latency per each run are reported in Table 6.2. The errors are ≤ 5 ns. The values are all consistent with the latency time expected by the Crystal CS-5381 ADC and Crystal CS-8406 DIT [98].

Run	Latency time (μs)		Run	Latency time (μs)
1	39.320		11	39.350
2	39.349		12	39.268
3	39.259		13	39.359
4	39.358		14	39.267
5	39.294		15	39.319
6	39.395		16	39.341
7	39.346		17	39.285
8	39.391		18	39.337
9	39.297		19	39.278
10	39.288		20	39.380

Table 6.2: Latency time measurements of the SMO floor electronic chain.

The time differences between different runs (average= 39.325 μs, standard deviation =0.043 μs) are due to unpredictability of the locking (absolute phase) of the AcouBoard clock (24.576 MHz) with the Master clock provided by the FCMB(40 MHz). This implies that, at each switch of the detector, the absolute time stamping of acoustic data is known with an error of about 50 ns. However, once the detector is on, the system latency is fixed and constant with an uncertainty ≤ 5 ns. It's worth to mention that the overall time accuracy due to the electronics corresponds, since the velocity of acoustic wave in water is ~ 1500 m/s, to an indetermination of less than 1 mm. Given the excellent performances of the absolute GPS time-stamp system, provided by the SMO electronics, we could also evaluated contributions to the latency time due to hydrophone ceramics. These measurements were performed during the waterpool tests at

CNR-IDASC. As described before, the emission of the acoustic pulses from the calibrated transducer were triggered by the PPS signal, provided by the GPS receiver. In addition, the time delays introduced by the CNR-IDASC emission system were measured by means of a 5 GHz sampling oscilloscope. It was, therefore, possible to determine the contribution due only to latencies introduced by mechanical movements of the hydrophones and of the emitting ceramics (T_{cer}). This latency time is given by the following relation:

$$T_{cer} = T_{acq} - T_{PPS} - (T_{gen} + T_{cabling}) - T_{el} - T_{dist} \tag{6.0}$$

where T_{acq} is the absolute GPS time associated by the SMO data acquisition system to the detected pulse, T_{PPS} is the emission time of the PPS signal, T_{gen} is the latency time of the emission system electronics (waveform generator and high voltage amplifier), equal to 460 ns ± 5 ns, $T_{cabling}$ is the delay due to electric and optical cabling of the used setup, T_{el} is the latency time of the SMO data acquisition electronics (known by previous measurement), T_{dist} is the transit time of acoustic pulse to reach the hydrophone in water. The absolute time of the acquired pulse (T_{acq}) was calculated using a correlation function on resampled signal (as described before). T_{dist} was calculated taking into account the hydrophone-transducer geometrical distance and considering a sound velocity in water of 1497 m/s, deduced by the water environmental parameters measured at CNR-IDASC pool. In this analysis we assumed also that emission and reception of the acoustic wave happened at the centre of the ceramics. Since the waveform of the data signals acquired with Sensor Technology Ltd FFR hydrophones does not well reproduce the expected shape of the test signals, the analysis for the evaluation of the ceramics latency of the sensors has been carried out only on SMID hydrophones data. Fig. 6.23 shows the values of T_{corr} obtained for SMID S/N 14 hydrophone, pulsing the acoustic emitter with 32 kHz sinusoidal waves, at different input voltages (100 mV$_{rms}$, 200 mV$_{rms}$, 400 mV$_{rms}$). Each experimental point is obtained averaging out the results obtained with 120 pulses. The error associated to the data takes into account the statistical error ($\leq$ 10 ns), the error on latency time of SMO DAQ electronics ($\leq$50 ns) and the error due to the T$_{Dist}$ $\sim$ that is 1 cm/1497 m/s $\approx$ 7.5 μs

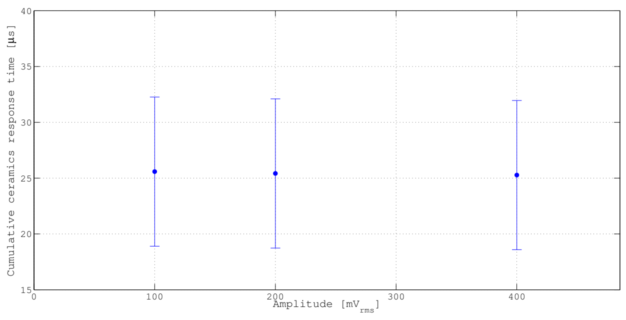

Figure 6.23: Cumulative ceramics response time of the ITC 1032 emitter and SMID hydrophone as a function of the amplitude of the input electrical signals produced by the waveform generator. The measurements have been performed with 157 μs long pulses at 32 kHz.

Fig. 6.24 shows cumulative ceramics response time, obtained for 120 test signals, emitted at frequencies of 10, 20, 32, 40 and 50 kHz.

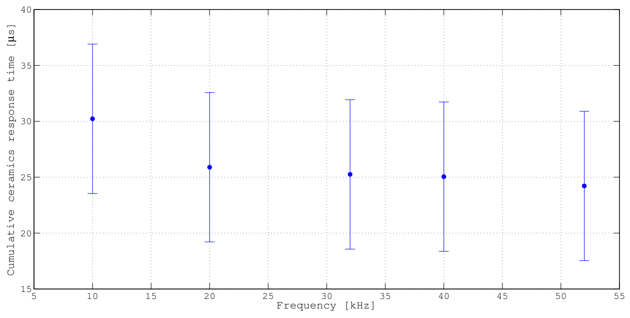

Figure 6.24: Cumulative ceramics response time of the ITC 1032 emitter and SMID hydrophones as a function of the acoustic signal frequency.

The obtained results show that the contribution to the latency due to the excitation time of the two ceramics is of the order of 25 μs above 20 kHz, corresponding to a time of flight path in water of about 3 cm. This preliminary result requires still further investigation, however the uncertainty due to the measure of the cumulative latency time of the ceramics is irrelevant for positioning purpose.

Chapter 7

Multidisciplinary science with deep-sea acoustic arrays: the East Sicily node of EMSO

In parallel with the activity of SMO at Capo Passero Site, a small-scale acoustic array has been designed and installed by the SMO Collaboration in the NEMO submarine Test Site (TS), 25 km off-shore Catania (Sicily) at a depth of 2100 m. The array was built thanks to funding gained by INFN in the framework of the LIDO (LIstening to the Deep-Ocean environment) Demonstration Mission [109] of ESONET [110]. The TS is nowadays indicated as the *East Sicily node*: the first cabled observatory of the EMSO project [111], a European infrastructure (ESFRI-European Strategy Forum on Research Infrastructures), born from ESONET, aiming at building a European-scale network of seafloor observatories and platforms with the basic scientific objective of long-term monitoring, mainly in real-time, of environmental processes related to the interaction between the geosphere, biosphere, and hydrosphere, including natural hazards. EMSO will be a geographically distributed infrastructure composed of several deep-seafloor observatories, which will be deployed on specific sites around European waters, reaching from the Arctic to the Black Sea passing through the Mediterranean Sea, thus forming a widely distributed pan-European infrastructure (Fig. 7.1). The main goal of EMSO is to allow the real-time data transmission from the multidisciplinary observatories to shore for specific activities addressed to a long term geo-hazard monitoring (earthquakes and tsunamis) and characterisation of marine ambient noise, with special attention to bioacoustics (mainly detection of marine mammals).

The East-Sicily node of EMSO consists of two underwater cabled stations, NEMO SN1 and OνDE-2, hosting standard environmental sensors and two tetrahedral arrays of hydrophones (one for each station), built by the INFN and INGV [112]. The NEMO-SN1 station was deployed and connected in June 2012. The OνDE-2 station was deployed and it is anchored on the seafloor, ready for the ROV connection, scheduled for the 2013. In this chapter the architectures of the NEMO SN-1 and of the

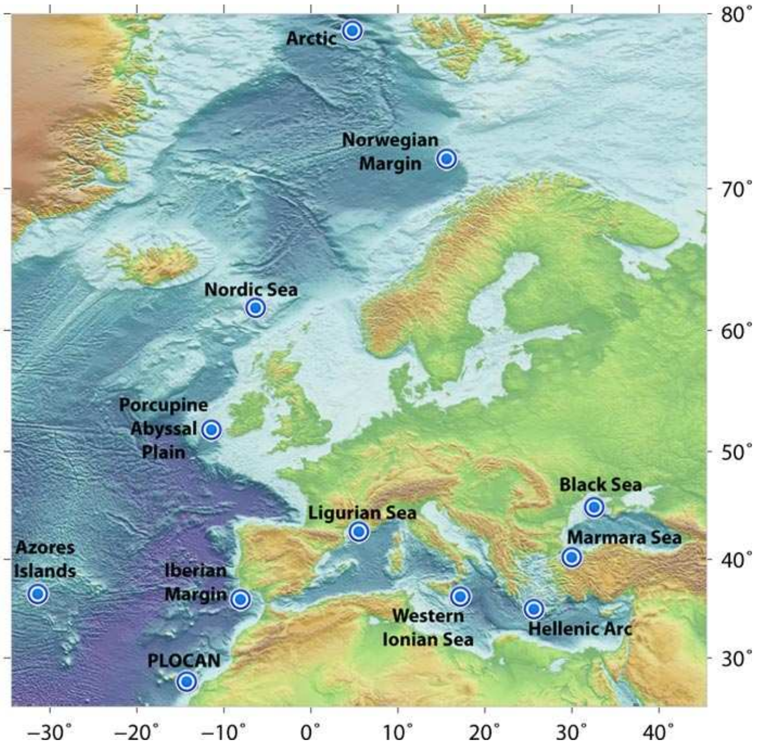

Figure 7.1: Map of the EMSO nodes.

OνDe-2 hydrophones arrays, the management and the real time analysis of the acquired acoustic data are briefly described

7.1 The EMSO East-Sicily node

The infrastructure of the EMSO East-Sicily node consists of a shore station, of an electro-optical submarine cable and of an underwater observatory. The shore station is located inside the port of Catania; it hosts the power supply system, the instrumentation control system and the landing stations of the data transmission and data acquisition systems. The electro-optical submarine cable connects the underwater stations to the shore station. It is a 28 km electro-optical cable split – at about 20 km from the coast – in two branches, each one is 5 km long. Both branches are terminated with electro-optical underwater connectors to host experimental stations. One branch (hereafter Test Site North, TSN) provides connection for the NEMO SN-1 multidisciplinary station, in the other branch is installed the OνDE-2 experiment, as shown in Fig. 7.2.

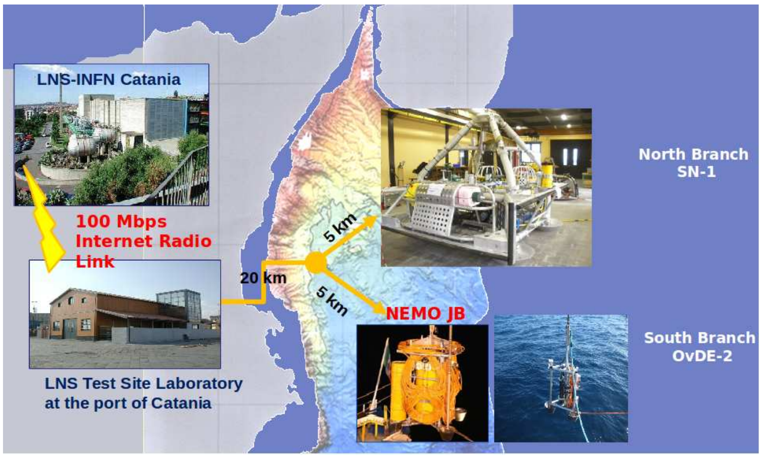

Figure 7.2: Sketch of the East Sicily Node.

7.2 The NEMO-SN1 observatory

The NEMO-SN1 observatory, shown in Fig. 7.3 was installed on 6^{th} of June 2012 and connected to the TSN. It is an upgraded version of the former SN1 station [113], a GEOSTAR (GEophysical and Oceanographic STation for Abyssal Research) class multidisciplinary observatory, deployed in the same site in 2005 and recovered in 2008. NEMO-SN1 hosts geophysical and environmental sensors and a tetrahedral array of hydrophones, that were not present in the previous experimental configuration. The list of sensors with their sampling rates is shown in Table 7.1.

Several mechanical parts of the station have been refurbished with respect to the former SN1 observatory. In particular the mechanical frame has been modified in order to host deep-sea hydrophones and allow easily handling of seismometers and magnetometers with Remotely Operated

Sensor	Sampl. rate	Model
3-C broad-band seismometer	100 Hz	Guralp CMG-1T
Hydrophone for Geophysics	200 Hz	OAS E-2PD
Hydrophone for Geophysics	2000 Hz	SMID
Hydrophone for Bio-acoustics	96/192 kHz	SMID
DPG (Differential Pressure Gauge)	10 Hz	St.Diego Univ. Prototype
APG (Absolute Pressure Gauge)	15 s	Paroscientific 8CB4000-I
3-C accelerometer + 3-G gyro	100 Hz	Gladiator Techn. Landmark 10
Gravity meter	1 Hz	ISFI-INAF Prototype
Scalar magnetometer	1 Hz	Marine Magnetics Sentinel
Vectorial magnetometer	1 Hz	INGV Prototype
ADCP 600 kHz	1 profile/h	RDI Workhorse Monitor
CTD	1 sample/h	SeaBird SBE-37SM-24835
Turbidity meter	1 sample/h	Wet Lab
3-C single point current meter	2 Hz	Nobska MAVS-3

Table 7.1: List of sensors with sampling rates and models adopted in the NEMO SN-1 station.

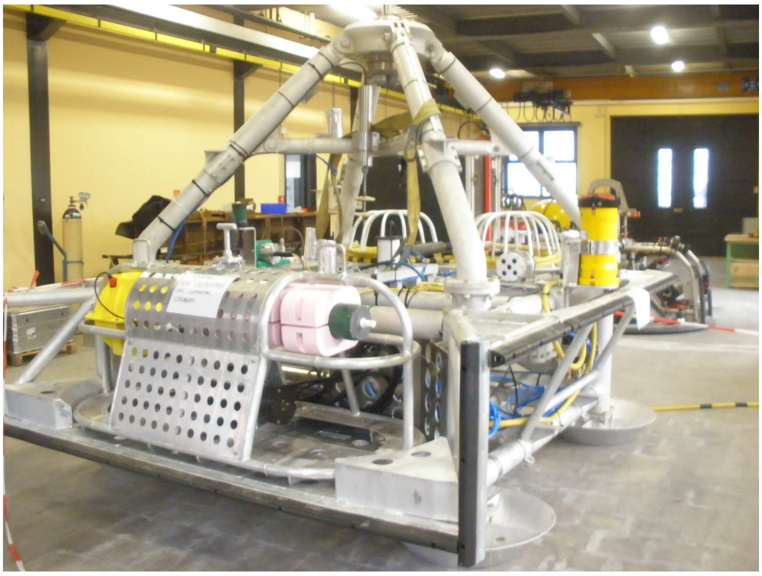

Figure 7.3: The TSN station, inside the LNS-INFN Shore Lab of Catania, ready for deployment.

Vehicles (ROV) for deep-sea operations; since the cabled power feeding system relies on power transmission through a main underwater electro-optical cable, batteries and their containers, used for stand-alone applications, have removed. The power, data acquisition and transmission systems of the INGV geophysical instruments are hosted in a titanium pressure vessel, called DACS (Data Acquisition and Control System); the front-end electronics of the hydrophones are installed in a 13” diameter pressure resistant glass housing. Concerning the electronic system, refurbishments have been carried out to the power feeding, data acquisition and data transmission systems: HVAC/LVDC power converters have been added to permit power feeding directly from shore and new full real-time data transmission system, complaint with C/D-WDM protocol, has been designed. The power electronics for SN-1 is composed of a shore power supply, a control unit and deep-sea power conversion subsystems placed in the DACS and in the glass housing that hosts the hydrophones front-end electronics.

The on shore power supply provides 500 VAC (single phase) power to the deep-sea installation. Thanks to a primary AC/AC power converter hosted in the DACS, the power is converted in several low voltage AC output lines; secondary low voltage AC/DC converters provide the low voltage DC power to the environmental and geophysics instrumentation. A dedicated 230 VAC low-noise power supply line is addressed to the glass housing hosting the hydrophones front-end electronics, where 230VAC/LowVoltage-DC converters are installed. The electro-optical data transmission chain has been designed and built by INFN in order to ensure reliability and full redundancy of the optical data transmission channels. For this reason the data transmission system, based on bidirectional Ethernet electro/optical media converters, was built using 3 e.o. Ethernet modems with 3 separated CWDM optical frequencies for uplink (shore to sea) and downlink (sea to shore). Hydrophones data are transmitted using e.o. CWDM media converters that utilise 2 CWDM frequencies (1530 nm and 1570 nm) for downlink, geophysical and oceanographic data use the other CWDM frequency for downlink.

Another frequency is used for controls (uplink). This configuration is obtained using an "optical add/drop box" capable to add the CWDM optical frequencies on a single fibre, duplicated on 2 optical fibres to improve system redundancy and reliability.

The acoustic array of NEMO SN-1 station consists of 4 SMID TR-401 hydrophones (same model of the hydrophones installed on the NEMO-SMO tower) arranged in a tetrahedral configuration at distance of about 1 m each other. Data from hydrophones are continuously digitized underwater by a professional audio acquisition board, model Texas Instruments PCM4204EVM (sampling frequency of 96 kHz, resolution of 24 bit)[114] installed in the glass housing. A metallic box shields the board from electromagnetic noise induced by other instruments of the station (see Fig. 7.4).

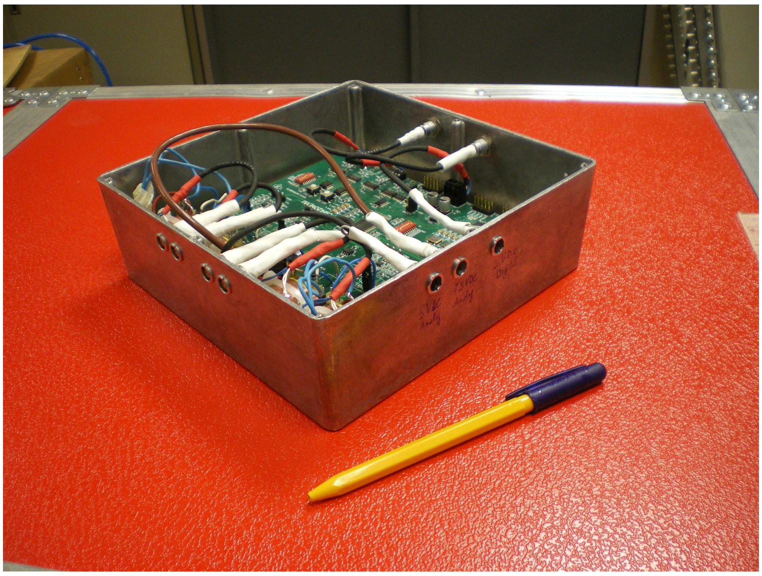

Figure 7.4: Picture of the audio acquisition board Texas Instruments PCM4204EVM. In order to shield the board from electromagnetic noise, the board has been installed in a metallic box.

The board features 4 input channels. The output data of the board are codified in the AES/EBU stereo audio standard; the signals coming from the 4 hydrophones are transmitted on two different stereo serial streams towards the electro-optical media converters hosted in the DACS. On shore the two optical data stream are reconverted in electrical signals by 2 fibre optic RS-422 data receivers. The audio data stream is GPS time stamped on shore by means of a modified FCMB. Audio data, in AES/EBU standard format, are acquired by a sound card installed on a PC that sends them via TCP/IP to a PC farm dedicated to the data storage and analysis. A schematic view of the data acquisition system of the acoustic array installed on the NEMO SN-1 station is shown in Fig. 7.5.

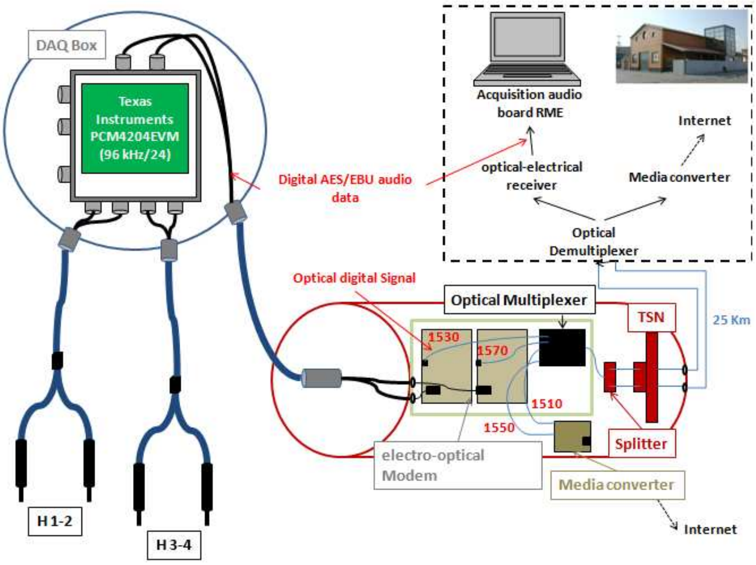

Figure 7.5: Schematic view of the data acquisition system of the acoustic array installed on board the NEMO SN-1 station.

7.3 OνDe-2

The OνDE-2 station (Fig. 7.6), is anchored in the TSS and has been entirely designed and constructed by the INFN. Similarly to NEMO-SN1, the acoustic array is composed of 4 SMID TR-401 hydrophones coupled with SMID AM-401 preamplifiers. The construction of OνDE-2 has represented a test-bench for the SMO project. Indeed, the same hydrophones and the same electronics of data acquisition system of SMO are used. The OνDE DAQ comprises 2 AcouBoard (192 kHz/24 bit), a FCMB, a SCI to manage an AHRS (Attitude Heading Reference System) board and a CPS to distribute power to all the devices. As for SMO, the underwater electronics is hosted in an aluminium vessel. In order to read synchronously from 4 hydrophones, OνDE-2 host in its pressure vessel two AcouBoards instead that one. The 2 stereo AES/EBU data streams, produced by the 2 AcouBoard, are managed by the same FCMB that labels them with the absolute GPS time of acquisition and send them to shore station on optical link. On shore, such as SMO data acquisition system, data from the underwater station are received by an eFCMB and addressed to a RME Hammerfall HDSP sound card, installed in a dedicated Acoustic Data Server (ADS). Acoustic data are available through TCP/IP connection to local and remote clients for the analysis.

7.4 Real-time data analysis

The analysis of the acoustic data acquired by the East Sicily North station is performed by custom software developed by the SMO Collaboration. As described in the previous sections, the stream of acoustic raw data coming from sea distributed to the analysis computer farm trough a TCP/IP connection with the AcouServers. In order to monitor the acoustic background noise of the underwater environment and to detect impulsive sources (acoustic pingers, marine mammals sounds, earthquakes), a real-time software for statistical analysis of the underwater sounds was implemented: the Acoustic Real-Time Analysis (ARTA). The software modules for data acquisition and data parsing have been written in JAVA language, while software tools for data analysis have been implemented under MATLAB platform. The choice of the JAVA language make the

Figure 7.6: The mechanical frame hosting OνDE-2 acoustic array.

software compatible with all computer architectures and operating systems and the MATLAB platform permits interface with several tools with user friendly interface. The software displays to the scientific users the real-time oscillogram and the spectrogram (2048 points with an overlap of 50 %) of the acoustic signals recorded by each hydrophone every 5 seconds. Moreover, the software calculates each 200 ms – corresponding to 19200 samples for the acoustic array installed on NEMO-SN1 (sampling frequency= 96 kHz) and 38400 samples for the OνDE-2 station (sampling frequency= 192 kHz) – the periodogram of the acquired signals by means of a Fast Fourier Transform at 1024 points. At regular intervals of 5 minutes, the values of the periodograms are collected in a ASCII file and recorded for further offline data analysis. In addition, the software

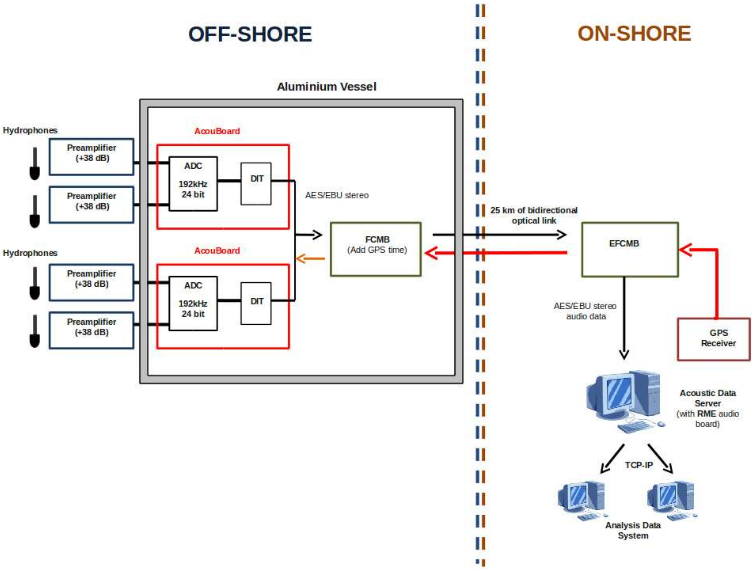

Figure 7.7: Schematic view of the data acquisition system of the OνDE-2 acoustic array.

calculates, as a function of the frequencies, the maximum amplitude, the mean value, the 95th percentile, the 90th percentile and the median of the analysed data . This information is stored in a dedicated database (MOIST - Multidisciplinary Ocean Information SysTem) [115], installed at the INFN-LNS computer centre that can be remotely accessed by the partner institutes of EMSO, for collaborative analysis. Fig. 7.8 shows a screen-shot of the software tool during a test in air of OνDE-2. Signals of a 32 kHz acoustic emitter (5 ms long pulses at a repetition rate of $\sim$ 1.2 s) are clearly visible.

7.5 First results

In the first months of activity, data acquired by NEMO SN-1 have allowed to measure underwater environmental acoustic noise and to detect signals of biological and geophysical interest. The environmental noise has been correlated with the marine traffic in proximity of the station,

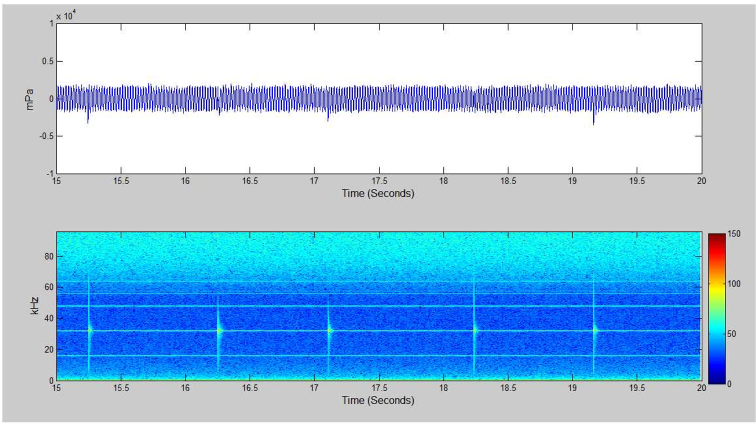

Figure 7.8: Screen shot of the real-time oscillogram and spectrogram produced by the ARTA software during a test with a 32 kHz acoustic beacon.

thanks to data acquired by AIS (Automatic Identification System) [116] antenna installed at INFN-LNS. AIS is an automatic tracking system, standardized by the International Telecommunication Union (ITU) [117] and used on ships and by vessel traffic services to identify and locate vessels. The system provides also the heading, the velocity and information about their size and destination. In Fig. 7.9 the daily spectrogram of the underwater acoustic noise recorded by NEMO SN-1 is reported. The typical passages of the ships above the station are clearly visible. Fig. 7.10 reports a map showing the correspondent vessels tracks, recovered by means of the AIS system.

The preliminary analysis of the NEMO SN-1 acoustic data highlights also a massive presence of dolphins, in particular *Striped Dolphin*, identified through detection of their whistles and echo-localization clicks (Fig. 7.11); sperm whales events have been also detected (see Fig. 7.12), as expected from previous OνDE data analysis.

Thanks to the use of hydrophones with a good sensitivity extended down to low frequency ($\sim$ 10 Hz), earthquake signatures has been also detected in coincidence with the NEMO SN-1 seismometer signal. Acoustic signature of earthquake signatures has been detected as acoustic signal

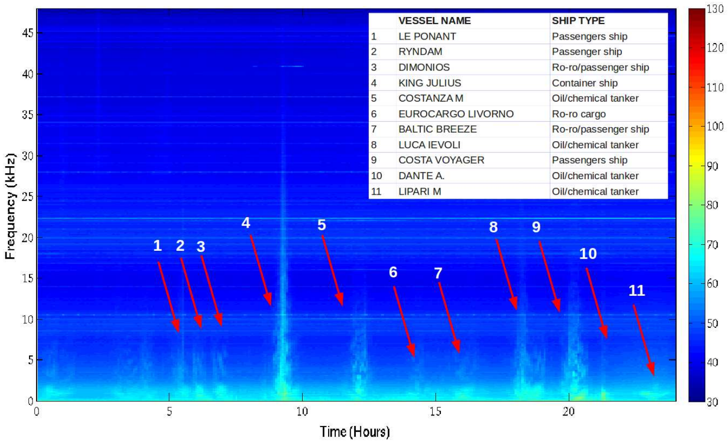

	VESSEL NAME	SHIP TYPE
1	LE PONANT	Passengers ship
2	RYNDAM	Passenger ship
3	DIMONIOS	Ro-ro/passenger ship
4	KING JULIUS	Container ship
5	COSTANZA M	Oil/chemical tanker
6	EUROCARGO LIVORNO	Ro-ro cargo
7	BALTIC BREEZE	Ro-ro/passenger ship
8	LUCA IEVOLI	Oil/chemical tanker
9	COSTA VOYAGER	Passengers ship
10	DANTE A.	Oil/chemical tanker
11	LIPARI M	Oil/chemical tanker

Figure 7.9: Daily spectrogram of the acoustic data acquired by SN-1 on the 13th of October 2012. Noise increase has been measured in correspondence of the ships transit close to the station.

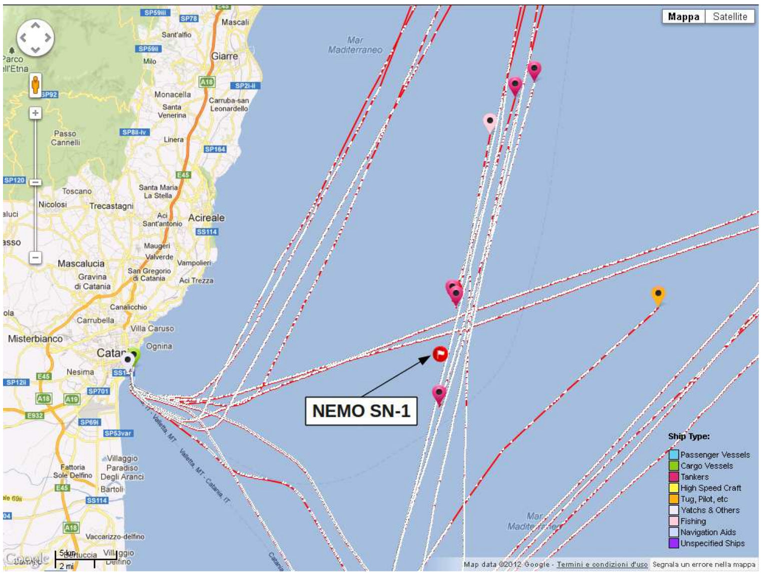

Figure 7.10: Vessels tracks recorded close to the NEMO SN-1 Station on the 13th of October 2012 by means of the AIS system.

produced by the vibration of the NEMO-SN1 mechanical frame, where the hydrophones are installed. In the Fig. 7.13 the hydrophones signals recorded correlating with a seismic event (magnitude 4.7) in the Ionian Sea on the 4th of July 2012 is reported.

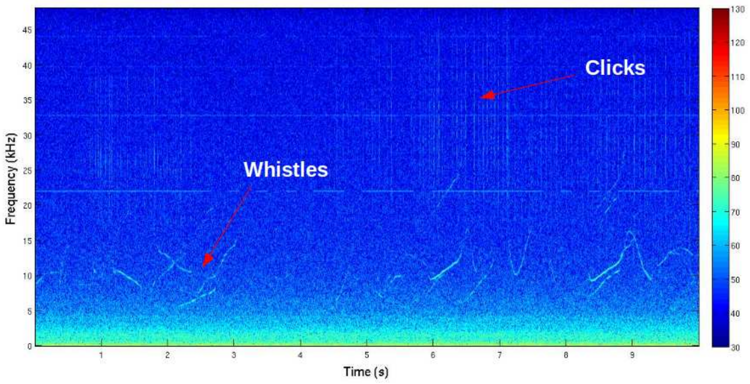

Figure 7.11: Spectrogram of whistles and clicks emitted by striped dolphins .

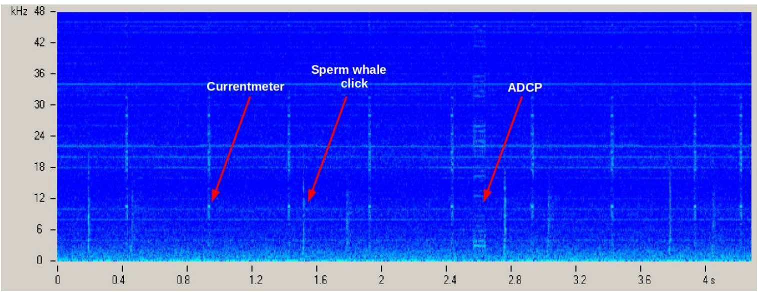

Figure 7.12: Spectrogram of sperm whale clicks detected by SN-1. The spectrogram shows also the acoustic noise produced by the ADCP and the currentmeter (repetition rate: 2 Hz) installed on the station.

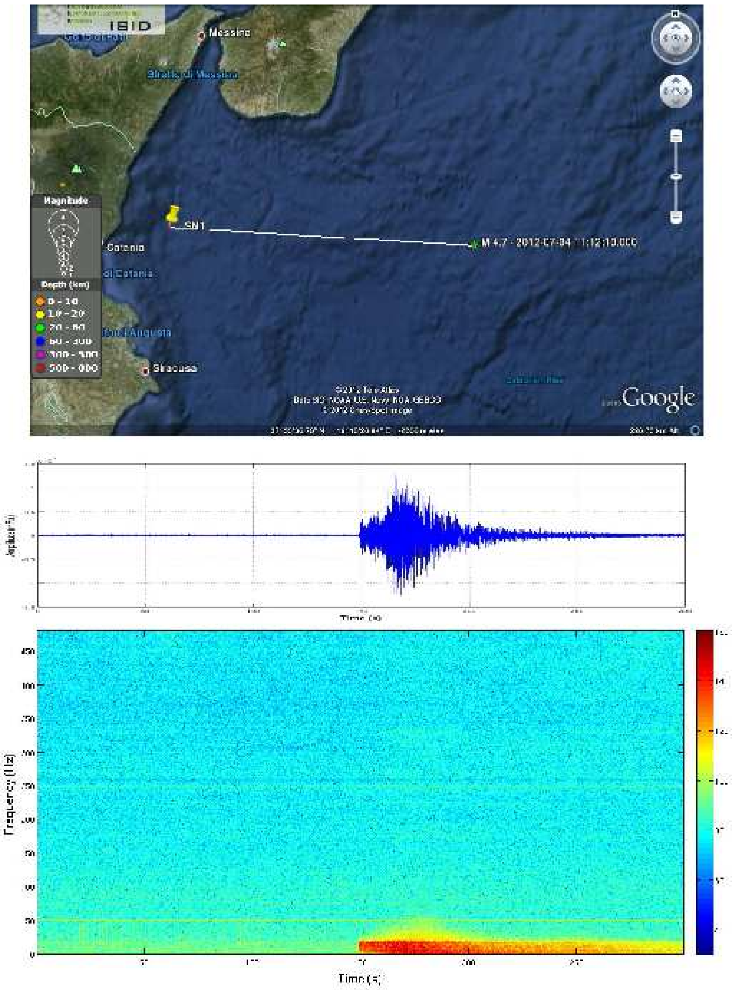

Figure 7.13: Oscillogram and spectrogram of the signals acquired by the NEMO SN-1 hydrophones in coincidence with a seismic event in the Ionian Sea (map on top).

Conclusions

Neutrino astronomy represents a powerful tool to investigate high energy events in the Universe. Since neutrino is subjected only to weak nuclear interaction, it can propagate through the Universe almost unabsorbed. This feature makes the neutrino an optimal probe to explore remote regions of the Universe and to study the physical processes the occur inside dense astrophysical sources. Depending on the energy range of the neutrino, different experimental detection techniques are proposed and applied. For neutrino energy between TeV and PeV, the most mature detection technique is the underwater Čerenkov one. This technique consists in the detection of Čerenkov light induced by the ultra-relativistic leptons, originated in the charged current neutrino interactions in a large volume of water or ice. If the lepton originated in the neutrino interaction is a muon, it is possible to determine the arrival direction of the incoming muon neutrino, and thus to point back to the neutrino astrophysical source. In fact, at high energies the muon direction is aligned with that one of the neutrino; above 100 TeV the neutrino direction can be determined with a precision $\theta_{rms} \sim 0.1^\circ$. The ICECUBE project, installed in the polar ices of Antarctica, accomplished in the 2010, is the first operating km^3-scale Čerenkov neutrino telescope. In the Northern Hemisphere, the ANTARES, NEMO and NESTOR Collaborations have established the KM3NeT Consortium, carrying out the design and construction of a Čerenkov neutrino telescope in the Mediterranean Sea. The work described in this thesis has been carried out within the NEMO

Collaboration, where I took an active part in theintegration and test of the NEMO Phase-II detector, a prototype of KM3NeT detection unit. The NEMO Phase-II concept is based on semi-rigid vertical structures, towers, composed of a sequence of eight horizontal frames (named floors) made of marine grade aluminium and interlinked by a system of ropes. Each floor hosts two optical modules at either end, one looking vertically downwards and the other horizontally outwards. The tower will be anchored to the seabed and kept vertical by appropriate buoyancy on the top. The spacing between storeys is 40 m, while the distance between the anchor and the lowermost floor is about 100 m. The detector has been integrated in a “compact” configuration that eases transportation and deployment on the seabed. In my Ph.D. activity, I took part at the integration and tests of the whole detector, at the functionality tests of the floor control modules and sensors and at the time calibration of the data acquisition and transport systems.

The activity reported in this thesis, was mainly addressed to the construction and test of a novel underwater acoustic detector for particle physics and multidisciplinary science. The detector, developed in the framework of the project SMO (Submarine Multidisciplinary Observatory), funded by “Futuro in Ricerca 2008” funds of MIUR, is installed onboard NEMO Phase-II tower. SMO consists of a 3D array of 14 broadband (10 Hz $\div$ 70 kHz) hydrophones, complemented with 2 couples of acoustic sensors provided by other groups of the KM3NeT Collaboration. Unlike commercial acoustic arrays, the SMO data acquisition system is based on the “all data to shore” concept: hydrophone data are sampled underwater at 192 kHz/24 bit and transmitted in real time to shore. Performances of the whole apparatus have been studied and evaluated. In particular, the electronic noise of the data acquisition electronics has been measured, using dedicated test benches, set up at LNS-INFN. The measured total power (RMS) of the electronic noise is -72 dB re 1 V and its spectral density, in the range 1 kHz ÷ 50 kHz, is -140 dB re 1 V^2/Hz, corresponding to an equivalent acoustic power spectral density of about 30 dB re 1 μPa^2/Hz. These values define the smallest amplitude of the acoustic signals that the SMO array can detect as function of the frequency. This very low electronics noise makes the SMO detector suitable for searching for impulsive signals in the frequency range of interests of the acoustic neutrino detection, perfectly complaint with the goal of detecting biological signals (namely mammals sounds). In order to determine the response of the whole system to acoustic waves, tests in a scientific waterpool facility available at CNR-IDASC of Rome have been performed. Tests in water demonstrated that the response of SMO data acquisition system, equipped with novel SMID TR-401 hydrophones, proposed by NEMO and SMO for the KM3NeT project, does not depend on the frequency of the incident acoustic wave. Moreover, tests confirmed that data acquisition electronics of SMO does not introduce, at the frequencies of interest, noise distortion and amplification of the hydrophone analogue signal, typically very low (few nV). The same measurements have been performed using low-cost Sensors technology Ltd SX30 FFR hydrophones, proposed for the KM3NeT project by UPV (Universitat Politècnica de València). Contrary to SMID hydrophones, the transfer function of FFR hydrophones is different for each sensor. The use of FFR hydrophones implies, therefore, a preliminary calibration procedure for each single sensor. This work also reports for the very first time tests to evaluate the performances of Opto-Acoustic Modules, a novel technology suggested to build the acoustic positioning array of KM3NeT. Tests demonstrated that the technology, even if promising is not yet mature.

The SMO acoustic array is also designed to provide the positioning of mechanical structures of the NEMO Phase-II tower underwater, through the measurements of the time of flight of acoustic signals emitted by a long baseline of acoustic emitters anchored on the seabed. So, the SMO DAQ architecture design was mainly driven by the necessity of a common time (Master Clock) distribution all over the system in order to correlate signals from different parts of the apparatus. For this purpose an innovative technology was implemented to achieve absolute GPS time-stamping of data underwater. Acoustic data are transmitted from the underwater detector to shore in the AES/EBU audio standard. Each AES/EBU block (containing 192 audio samples) is labelled by the NEMO Phase-II Floor Control Module Board with the absolute GPS time of acquisition, distributed from shore. Tests carried out in this work show that acoustic data are time-stamped underwater with a known and measurable latency (time delay) with respect to the GPS absolute time. This latency can be attributed to two contributions: one depending on the electronics and data transport system, the other one depending on the mechanical properties of the hydrophone ceramics. In this work, the two contributions have been measured separately. The measured electronics latency of each SMO channel is 39.325 μs ± 0.043 μs. The contribution depending on the mechanical response of hydrophone ceramics has been evaluated from tests carried out at the CNR-IDASC facility. The latency time of the hydrophone ceramics, measured at CNR-IDASC, is less than 25 μs. These features will permit the alignment in time of data recorded on shore from all sensors. The estimated accuracy in the determination of time of flight path between hydrophone and acoustic source is thus better than 10 cm. This is a not trivial feature considering that the detector is placed at 100 km from shore station, where the GPS sources is located. Moreover, both acoustic and optical sensors installed in the NEMO-SMO tower are phased with the absolute GPS time. This feature will be used, for the first time, to search for acoustic impulsive signals in coincidence with events reconstructed by the Čerenkov array, allowing preliminary studies on acoustic neutrino detection. The NEMO Phase-II and the SMO detectors, discussed in this thesis have been integrated and fully tested at the INFN-LNS. The deployment of the NEMO Phase-II tower is now foreseen for the first months of the 2013.

In parallel with the activities carried out on the NEMO Phase-II and SMO detectors, during this Ph.D. work I took part in the construction of the NEMO SN-1 and OνDE-2 acoustic arrays. These 2 experiments are deployed and are operating at the NEMO Test Site, 25 km off-shore Catania, at a depth of 2000 m, since June 2012. The two arrays, funded by the European ESONET and EMSO-ESFRI projects and managed in collaboration with SMO, allowed also to test the hardware and software technologies employed for the SMO array onboard NEMO Phase-II. Looking forward the deployment of the NEMO-SMO detector in Capo Passero Site, real time real time analysis software tools, fully compliant with SMO data acquisition architecture, have been developed and tested on NEMO SN-1 and OνDE-2 data.

Preliminary analysis of NEMO SN-1 data have demonstrated the capability of the acoustic array to monitor the underwater acoustic noise and to detect anthropic acoustic sources (ships, pingers, airguns) and the sounds produced by marine mammals present in the area. The success of this enterprise paves the way to multidisciplinary use of infrastructures and detectors developed for astroparticle physics goals, as recommended by the ASPERA (AStroParticle ERAnet) committee [118].

Bibliography

[1] G. D. Rochester and C. C. Butler, Nature **160**, 855 (1947).

[2] J.A. Simpson, Ann. Rev. Nucl. Part. Sci. **33**, 323 (1983).

[3] L. J. Gleeson and W. I. Axford, Astrophysical Journal **154**, 1011 (1968).

[4] V. L. Ginzburg and S. I. Syrovatskii, Annu. Rev. Astron. Astrophys. **3**, 297 (1965).

[5] C. Macolino and the Pierre Auger Collaboration, Journal of Physics: Conference Series **375**, 052002 (2012).

[6] E. Fermi, Phys. Rev. **75**, 1169 (1949).

[7] M. S. Longair, *High Energy Astrophysics* (Cambridge University Press, Cambridge U.K., 1992), Vol. 2.

[8] A. M. Hillas, Annu. Rev. Astron. Astrophys. **22**, 425 (1984).

[9] MAGIC website, http://magic.mppmu.mpg.de .

[10] High Energy Stereoscopic System website, http://www.mpi-hd.mpg.de/hfm/HESS/ .

[11] Very Energetic Radiation Imaging Telescope Array System website, http://veritas.sao.arizona.edu/ .

[12] F.A. Aharonian, *Very High Energy Cosmic Gamma Radiation: A Crucial Window on the Extreme Universe* (World Scientific, ADDRESS, 2004).

[13] A. Giuliani et al., The Astrophysical Journal Letters **742**, L30 (2011).

[14] S.Aiello et al., Astroparticle Physics **28**, 1 (2007).

[15] Meng Su, Tracy R. Slatyer, and Douglas P. Finkbeiner, The Astrophysical Journal **724**, 1044 (2010).

[16] LAT Pass 7 Galactic Diffuse Model, http://fermi.gsfc.nasa.gov/ssc/data/access/lat/Model_details/Pass7_galactic.html .

[17] Gregory Dobler, Douglas P. Finkbeiner, Ilias Cholis, Tracy Slatyer, and Neal Weiner, The Astrophysical Journal **717**, 825 (2010).

[18] Gregory Dobler, The Astrophysical Journal **750**, 17 (2012).

[19] The KM3NeT Collaboration, ArXiv e-prints (2012).

[20] D. Band et al., Astrophysical Journal, Part 1 **413**, 281 (1993).

[21] Eli Waxman, The Astrophysical Journal Supplement Series **127**, 519 (2000).

[22] E. Waxman, PHIL.TRANS.ROY.SOC.LOND.A **365**, 1323 (2007).

[23] E. Waxman and J. Bahcall, Phys. Rev. Lett. **78**, 2292 (1997).

[24] R. et al. Abbasi, Phisical review D **84**, 082001 (2011).

[25] E. Waxman and J. Bahcall, Phys. Rev. Lett. (1999).

[26] W.-M. Yao et al., Journal of Physics G **33**, 1+ (2006).

[27] K. Greisen, Phys. Rev. Lett. **16**, 748 (1966).

[28] K Kotera, D Allard, and a.V Olinto, Journal of Cosmology and Astroparticle Physics **2010**, 013 (2010).

[29] L. Cazon and The Pierre Auger Collaboration, Journal of Physics: Conference Series **375**, 052003 (2012).

[30] L. B. Okun, *Leptoni e quark* (Nauka, Mosca, 1981), Vol. 2.

[31] S. R. Mishra et al., Nevis Laboratory Report **NEVIS**, 1453 (1992).

[32] R. Gandhi et al, doi:10.1016/0927-6505(96)00008-4 (1996).

[33] Atri Bhattacharya, Raj Gandhi, Werner Rodejohann, and Atsushi Watanabe, Journal of Cosmology and Astroparticle Physics **2011**, 017 (2011).

[34] R. Gandhi et al., Physical Review D **58**, 093009 (1998).

[35] P. Sapienza and G. Riccobene, La Rivista del Nuovo Cimento **32**, 591 (2009).

[36] I. et al. Kravchenko, Phys. Rev. D **73**, 082002 (2006).

[37] H. Landsman, L. Ruckman, G. S. Varner, and IceCube Collaboration, Nuclear Instruments and Methods in Physics Research A **604**, 70 (2009).

[38] P. W. et al. Gorham, Phys. Rev. D **82**, 022004 (2010).

[39] J. Abraham, P. Abreu, M. Aglietta, C. Aguirre, E. J. Ahn, D. Allard, I. Allekotte, J. Allen, P. Allison, J. Alvarez-Muñiz, and et al., **79**, 102001 (2009).

[40] D. Fargion, P. G. De Sanctis Lucentini, M. De Santis, and M. Grossi, The Astrophysical Journal **613**, 1285 (2004).

[41] R. U. Abbasi et al., The Astrophysical Journal **684**, 790 (2008).

[42] Giorgio Riccobene, Journal of Physics: Conference Series **136**, 022053 (2008).

[43] Zheleznykh I.M. Markov, M.A., Nuclear Physics **27**, 385 (1961).

[44] M.A. Markov and I.M. Zheleznykh., Nucl. Instr. And Meth. A **248**, 242 (1986).

[45] V. A. Naumov T. S. Sinegovskaya S. I. Sinegovsky N. Takahashi E.V. Bugaev, A. Misaki, Phys. Rev. D **58**, 054001 (1998).

[46] T.K. Gaisser, (1997).

[47] J.G. Learned and K. Mnnheim, Activity Report 2008 INFN-LNS **50**, 679 (2000).

[48] C.D. Mobley, *Light and water: radiative transfer in natural waters* (Academic Press, ADDRESS, 1994).

[49] M. Ackermann and Others, Journal of Geophysical Research **111**, D13203 (2006).

[50] T. Gaisser, *Cosmic Rays and Particle Physics* (Cambridge University Press, ADDRESS, 1990).

[51] DUMAND website, http://www.phys.hawaii.edu/ dumand/ .

[52] Lake Baikal Neutrino Telescope website, http://baikalweb.jinr.ru/ .

[53] AMANDA website, http://amanda.uci.edu/ .

[54] R. Abbasi et al., Astropart.Phys. **35**, 615 (2012).

[55] R. Abbasi et al., Phys. Rev. Lett. **106**, 141101 (2011).

[56] KM3NeT website, http://www.km3net.org .

[57] KM3NeT: Conceptual Design Report, http://www.km3net.org/CDR/CDR-KM3NeT.pdf .

[58] KM3NeT: Technical Design Report, http://www.km3net.org/TDR/TDRKM3NeT.pdf .

[59] NESTOR website, http://www.nestor.org.gr .

[60] ANTARES website, http://antares.in2p3.fr .

[61] NEMO website, http://nemoweb.lns.infn.it .

[62] Astroparticle Physics **23**, 377 (2005).

[63] Th. for the ANTARES collaboration Eberl, ArXiv e-prints (2012).

[64] Nuclear Physics B - Proceedings Supplements **190**, 109 (2009).

[65] E. V. Bugaev, A. Misaki, V. A. Naumov, T. S. Sinegovskaya, S. I. Sinegovsky, and N. Takahashi, Phys. Rev. D **58**, 054001 (1998).

[66] G.A. Askaryan, The Soviet Journal of Atomic Energy **3**, 921 (1957).

[67] G.A. Askariyan, B.A. Dolgoshein, A.N. Kalinovsky, and N.V. Mokhov, Nuclear Instruments and Methods **164**, 267 (1979).

[68] J.G. Learned and K. Mnnheim, Phys. Rev. D **19**, 3293 (2000).

[69] L. Sulak et al., Nuclear Instruments and Methods **161**, 203 (1979).

[70] K. Graf and et al., 127 (2006).

[71] G. De Bonis, Nuclear Instruments and Methods in Physics Research Section A **604**, S199 (2009).

[72] V. Niess and V. Bertin, Astroparticle Physics **26**, 243 (2006).

[73] F. Simeone, Nuclear Instruments and Methods in Physics Research Section A **604**, S196 (2009).

[74] F. Simeone, Ph.D. thesis, Università di Roma "La Sapienza", 2008.

[75] Michael A. Ainslie, Journal of The Acoustical Society of America **103**, (1998).

[76] R. Abbasi et al., Astroparticle Physics **34**, 382 (2011).

[77] Ocean Conservation Research website, http://www.ocr.org .

[78] R.J. Urick, *Sound Propagation in the Sea* (Peninsula Publishing, ISBN 0-932146-08-2, 1982), Vol. 2.

[79] Nuclear Instruments and Methods in Physics Research Section A: Accelerators, Spectrometers, Detectors and Associated Equipment **683**, 78 (2012).

[80] J. Vandenbroucke N. Kurahashi and G. Gratta, Phys. Rev. D **82**, 073006 (2010).

[81] R. Lahmann and ANTARES Collaboration, Nuclear Instruments and Methods in Physics Research A **662**, 216 (2012).

[82] Pavan G. Nosengo N., Riccobene G., Nature **462**, 560 (2009).

[83] G. Riccobene et al, Astropart. Phys. **27**, 1 (2006).

[84] Teledyne ODI website, http://www.odi.com .

[85] GARR Consortium website, www.garr.it .

[86] Teen Photonics website, www.teemphotonics.com .

[87] Sea Bird Electronics website, http://www.seabird.com .

[88] K. V. Mackenzie, The Journal of the Acoustical Society of America **70**, 807 (1981).

[89] Wet Labs website, http://www.wetlabs.com .

[90] Aanderaa Data Instruments AS website, http://www.aadi.no .

[91] Submarine Multidisciplinary Observatory website, http://web.infn.it/smo .

[92] SMID Technology website, http://www.smidtechnology.it .

[93] Nato Undersea Research Centre website, http://www.nurc.nato.int .

[94] Sensor Technology Ltd website, http://www.sensortech.ca .

[95] Universitat Politécnica de Valéncia website, www.upv.es .

[96] Centre de Physique des Particules de Marseille website, http://marwww.in2p3.fr .

[97] Erlangen Centre for Astroparticle Physics website, www.ecap.nat.uni-erlangen.de .

[98] Cirrus Logic website, http://www.cirrus.com .

[99] European Broadcasting Union, Specification of the Digital Audio Interface (The AES/EBU interface), http://www.ebu.ch .

[100] RME website, http://www.rme-audio.de .

[101] ACSA website, http://www.underwater-gps.com .

[102] Istituto Di Acustica e Sensoristica "Orso Mario Corbino' CNR website, www.idasc.cnr.it .

[103] S. Viola, Master's thesis, .

[104] International Trasducer Corporation website, http://www.itc-transducers.com/ .

[105] Agilent Technologies website, http://www.home.agilent.com .

[106] Falco Systems website, www.falco-systems.com .

[107] Symmetricom website, www.symmetricom.com .

[108] F. Ameli et al., IEEE Transactions on Nuclear Science **55**, 233 (2008).

[109] Listening to the Deep-Ocean Environment website, www.listentothedeep.com .

[110] ESONET Network of Excellence website, www.esonet-noe.org .

[111] European Multidisciplinary Seafloor Observatory website, www.emso-eu.org .

[112] Istituto Nazionale di Geofisica e Vulcanologia website, www.ingv.it .

[113] P. Favali, L. Beranzoli, F. Italiano, E. Migneco, M. Musumeci, R. Papaleo, and NEMO Collaboration, Nuclear Instruments and Methods in Physics Research A **626**, 53 (2011).

[114] Texas Instruments website, www.ti.com .

[115] Multidisciplinary Ocean Information System website, http://moist.rm.ingv.it .

[116] Navigation Center of Excellence website, www.navcen.uscg.gov .

[117] International Telecommunication Union website, www.itu.int .

[118] AStroParticle ERAnet website, www.aspera-eu.org.it .